

Superconductivity Program for Electric Systems Annual Progress Report for Fiscal Year 2001

Superconductivity Technology Center Los Alamos National Laboratory

Dean E. Peterson, Center Director and Program Manager

Jeffrey O. Willis, Principal Team Leader and Editor

Contributors:

P.N. Arendt
S.P. Ashworth
J.F. Bingert
H.J. Boenig
L.E. Bronisz
D.J. Brown
G.W. Brown
L.N. Bulaevskii
B.L. Burley⁺
J.Y. Coulter
R.F. DePaula
P.C. Dowden
L.A. Emmert
A.T. Findikoglu
S.R. Foltyn
B.J. Gibbons

J.R. Groves
M.E. Hawley
T.G. Holesinger
D.B. Jan
Q.X. Jia
H. Kung
K. Lenseth[#]
Y. Li[#]
M.P. Maley
V. Matias
C.H. Mielke
F.M. Mueller
B.E. Newnam
R.D. Parella^{*}
D.E. Peterson
C. Park[#]

E.J. Peterson
Y. Qiao[#]
J. Reeves[#]
G.N. Riley, Jr.^{*}
D.A. Roybal
S. Sathiarju[#]
V. Selvamanickam[#]
J.E. Serna
A. Serquis
J.F. Smith
L. Stan
J.A. Waynert
J.O. Willis
Xing Yuan[#]
Y.T. Zhu

^{*}American Superconductor Corporation

⁺General Atomics

[#]IGC-Superpower

Work supported by the
United States Department of Energy
Office of Energy Efficiency and Renewable Energy /
Office of Utility Technologies

Table of Contents

Table of Figures	4
Glossary of Acronyms	10
Introduction.....	11
1. Highlights of Fiscal Year 2001	13
2. Technical Activities	15
2.1 Wire Technology	15
2.1.1 MgO IBAD Templates for YBCO Coated Conductors.....	15
2.1.2 High Current Coated Conductors Based on IBAD YSZ and Thick YBCO/Sm-123 Multilayers.....	26
2.1.3 Microstructural Development and Control in YBa ₂ Cu ₃ O _y Coated Conductors	32
2.1.4 Correlation between Transport Current Profiles and Tape Microstructure in YBCO Coated Conductors	38
2.1.5 Accelerated Coated Conductor Initiative	45
2.1.6 Scale-up of Coated Conductor Technology at IGC-SuperPower.....	56
2.1.7 Development of the Superconducting Phase and the Origin of Potential Current Limiting Defects in Bi-2223 Tapes	59
2.1.8 Effect of Lattice Strain and Defects on the Superconductivity of MgB ₂	66
2.2 Systems Technology.....	70
2.2.1. Fault Current Limiter Restoration Project.....	70
3. Fiscal Year 2001 Publications	79
3.1. Journal Articles Published.....	79
3.2. Journal Articles Submitted for Publication.....	82
3.3 Other Publications and Conference Abstracts	85
4. Patent and License Activity (April 1988 to Present)	91
4a. Invention Disclosures and Patent Applications	91
4b. Patents Granted.....	92
4c. Licenses Granted.....	94
5. Agreements in Progress (11 Active, all types)	94
5a. Superconductivity Pilot Center Agreements - Active.....	94
5b. CRADA Agreements - Active	94
5c. Funds In / Funds Out Agreements - Active	95
5d. Other Collaborations - Active.....	95
6. Completed Agreements.....	95
6a. Superconductivity Pilot Center Agreements - Completed.....	95
6b. CRADA Agreements - Completed	96
6c. Funds In / Funds Out Agreements - Completed	96
6d. Other Collaborations - Completed.....	97

Table of Figures

Figure 1. Comparison of in-plane texture development as a function of template layer thickness for IBAD YSZ and IBAD MgO (inset).	16
Figure 2. Improvement of YBCO in-plane texture (phi scan FWHM) relative to that of YSZ or MgO template layer textures.	17
Figure 3. Schematic of research chamber for MgO deposition.	17
Figure 4. RHEED patterns for MgO. (a) Rod-like pattern for IBAD MgO deposited homoepitaxially on single crystal MgO; (b) spot-like pattern for IBAD MgO deposited on crystalline Si with an amorphous layer of Si ₃ N ₄ ; and (c) ring-like pattern for MgO deposited on <i>a</i> -Si ₃ N ₄ /Si by e-beam with no ion assist beam.	17
Figure 5. Evolution of RHEED patterns during IBAD MgO film growth. (a) <i>a</i> -Si ₃ N ₄ /Si before starting growth; (b) after IBAD MgO deposition; (c) after homoepitaxial MgO film deposition.	18
Figure 6. Evolution of d-spacing observed by RHEED during deposition of IBAD and homoepitaxial MgO.	18
Figure 7. RHEED patterns showing tilting of spot pattern increasing with thickness. The orientation of the RHEED beam is 90° rotated from the direction of the ion assist beam.	18
Figure 8. Tilting of the c axis away from the MgO film normal as a function of film thickness. Results at LANL were confirmed and expanded by workers at Stanford University.	19
Figure 9a. Model for tilting in IBAD MgO. The top portion of the figure shows the effect of dislocations to form the tilt. About 10 ¹² dislocations/cm ² in 200 Å allows a 5° tilt to result. The bottom portion of the figure shows the region near the plane of dislocations.	19
Figure 9b. TEM micrograph of a MgO film. The bars indicate areas where interstitial point defects coalesce to form {110}-type planes.	19
Figure 10. X-ray intensity vs. rocking curve angle phi for a homoepitaxial layer of MgO deposited on IBAD MgO/ <i>a</i> -Si ₃ N ₄ /Hastelloy C276 substrate. A FWHM of less than 7° has been achieved.	20
Figure 11. YBCO in-plane texture (phi-scan FWHM) and critical current density J _c as a function of substrate surface roughness R _{rms}	20
Figure 12a. Schematic of IBAD loop coating system.	21
Figure 12b. Expanded view of region near the tape. The system can be used for small samples attached to moving tape or for a long length tape.	21
Figure 13. RHEED patterns on moving tape.	22
Figure 14a. Texture of IBAD MgO for two tapes not using the RHEED system (dashed curves) and with RHEED and two passes through the deposition zone (solid line).	22
Figure 14b. After several refinements, the texture quality and repeatability of the IBAD MgO tapes increased remarkably.	22
Figure 15a. TEM dark field micrograph of IBAD YSZ.	23
Figure 15b. TEM dark field micrograph of ion beam sputtered IBAD MgO.	23

Figure 16. Bright field TEM image of e-beam evaporated IBAD-MgO.	23
Figure 17. Dependence of critical current density on YBCO thickness for films deposited using IBAD YSZ and IBAD MgO template layers.	24
Figure 18. Critical current as a function of position for YBCO on meter length IBAD MgO templates produced in 2000 and 2001.	24
Figure 19. Critical current density and critical current of PLD YBCO on Inconel substrates with Y ₂ O ₃ - or CeO ₂ -buffered IBAD YSZ template layer. The bridge dimensions are ~0.2 mm x 5 mm.	26
Figure 20. Critical current normalized to the initial value as a function of thickness for three YBCO samples thinned progressively.	27
Figure 21. SEM Cross section (center) and plan view images (sides) at various levels throughout the thickness of a YBCO film.	27
Figure 22. (a) Stacking sequence of the Y-Sm-Y-Sm-Y multilayer film. The YBCO and SmBCO layer thicknesses are about 1.0 μ m and 0.2 μ m, respectively.	28
Figure 23. Critical current density as a function of YBCO film thickness for samples produced by the standard process and by the modified (Y/Sm-BCO multilayer) process. Also shown are contours of constant current per centimeter width. Inconel 625 substrate with YSZ IBAD; sample size is 0.2 mm x 5 mm.	29
Figure 24. Comparison of resistivity and superconducting critical temperature of a YBCO single layer and Y/Sm-BCO multilayer film.	29
Figure 25. Comparison of single and multilayer films at 75 K as a function of YBCO thickness. Above ~1.5 μ m, the I _c of the multilayer structure increases at a rate of 60 A/cm width/ μ m.	29
Figure 26. Comparison of YBCO standard process coated conductors on Inconel 625 with either LANL or ZFW YSZ IBAD. The IBAD layer was buffered with Y ₂ O ₃ or CeO ₂	30
Figure 27. Variation in the critical current as a function of position. The periodic variations showed a good correlation with temperature during the deposition process, indicating a problem with the temperature control.	30
Figure 28. Measurement results on 20 cm Y/Sm-BCO multilayer tape at 75 K. (a) Critical current on central 9 cm section of tape in a 0.6 T B c magnetic field. (b) Magnetic field dependence of central 5 cm section of tape. (c) Critical current of 335 A measured in magnetic field of ~ 4 mT (40 Oe).	31
Figure 29. SEM, TEM, and SAD micrographs of types of substrate defects that thread through the buffer layers and affect Y-123 film growth.	33
Figure 30. TEM micrograph of a crack structure in the IBAD YSZ layer and the resulting reaction between the Y-123 and buffer layers that results in the formation of an extended defect.	34
Figure 31. TEM micrographs of misoriented grains in the Y-123 films. Typical orientations are (a) a-axis, (b) 45° in-plane rotated, and (c) tilted Y-123 grains. The indicated orientations in (c) and (d) are approximately parallel to the [110] direction in the film. The tilted grains are not coherent with the film matrix and appear to be randomly oriented around the [001] direction.	35
Figure 32. Plot of J _c versus the thickness of the ceria buffer layer next to the Y-123 film. The Y-123 films were approximately 1.5 μ m thick and the critical thickness of the CeO ₂ layer was ~ 90 Å.	36

Figure 33. TEM micrographs of the Y-123 / ceria interfaces in films with nominal ceria thickness of (a) 90Å and (b) 1300Å. Whereas in (a) no interfacial reactions are found, a nearly continuous layer of BaCeO ₃ is present in (b).	36
Figure 34. TEM micrograph of a Y-123 coated conductor. The ceria thickness was 90 Å, which minimized the interfacial reactions. The only interfacial reactions present in this sample were those caused by substrate defects that propagate through the buffer layers as shown above. The resulting discontinuity in the substrate leads to an interfacial reaction at the Y-123 / ceria interface and a large pore in the Y-123 film.	36
Figure 35a. Schematic of the scanning system with scanning stage at room temperature connected to a long rod and pivot point near the sample, which is at liquid nitrogen temperature.	38
Figure 35b. Details of the MR sensor head construction. The sensor heads have an area of less than 1 μm ² and a sensitivity of greater than 3 μV/G.	38
Figure 36. Biot-Savart equations for the real and k-space components of the z component of the magnetic field calculated from a given current distribution. The experimental geometry is shown on the right.	39
Figure 37. Panel a) is a schematic showing the HTS bridge and current flow. Panels b) through d) are current maps acquired from the same area of the sample at 1.5, 1.75, and 2.0 A, respectively.	39
Figure 38. Current maps from the HTS tape. Panels a) through d) were taken with 5, 2.5, -2.5, and -5 A flowing respectively. Current flow direction is top to bottom. Imaged areas are ~ 9.2 mm x 9.2 mm.	40
Figure 39a. Current density is uniform over a high critical current I _c (185 A) region of the tape. The YBCO is deposited by PLD on a 1-cm wide Inconel substrate with an IBAD YSZ template layer.	41
Figure 39b. Current density shows the nonuniformity of the current flow in a low I _c (57 A) region of the same tape shown in 39a. The image on the right shows a vector current density map of the sample.	41
Figure 40a. Variation of the current density in the defect region of the conductor shown in Figure 3b with the transport current as a parameter. The top of the figure shows the density profiles in gray scale, and the bottom using a false color scale.	41
Figure 40b. Current density across the defected region of the tape as a function of position with the transport current as a parameter.	41
Figure 41. Left, current density map of low current region in tape. Right, x-ray peak intensity distributions for common YBCO orientations.	42
Figure 42. YBCO x-ray peak intensity ratios, known from the literature to correlate with deposition temperature, suggest that the deposition temperature varies across the tape width.	42
Figure 43. (104) Pole figures show both c- and a-axis-oriented components of YBCO in the bad region. The good region only shows c-axis oriented grains. The c- and a-axis orientation intensities are obtained by 360° integration in χ.	43
Figure 44. Phi angle FWHM does not vary across the tape, indicating that the poor performance is not caused by poor in-plane texture. However, the percentage of a-axis oriented grains is much higher in the bad region than in the good region.	43

Figure 45. SEM micrograph of the bad region (left) and the good region (right). The microstructure is consistent with lower temperature deposition in the bad region. Each image is about 20 μm on a side..	43
Figure 46. TEM images of the YBCO film. (A) - Dense, well-aligned film in the “good” section of the YBCO film. (B) - Significant amounts of porosity, a-axis YBCO, and secondary phases in the “poor J_c ” film section.	44
Figure 47. Plan view TEM images of regions from (A) the bad section of the film, showing the presence of a-axis oriented grains; and (B) the good section, showing much cleaner microstructure.	44
Figure 48. View of Los Alamos Research Park building located across the street from the LANL Administration Building.	45
Figure 49a. View of an Applications Laboratory at the Research Park.	46
Figure 49b. View of office at Los Alamos Research Park.	46
Figure 50. Schematic layout of the Research Park laboratories and offices.	46
Figure 51. Stacking sequence of layers in the LANL process for coated conductor fabrication.	47
Figure 52. Schematic of combinatorial method for coated conductor experiments. On the left, for instance, IBAD MgO is deposited under two conditions, A and B. On the right, three conditions (‘, ‘’, and ‘’’) are used to deposit PLD YBCO, resulting in a total of six combinations to be tested.	47
Figure 53. Illustration of tape polishing equipment ordered for the Research Park.	48
Figure 54. Schematic of laser scatterometer configuration and comparison of on line laser data with atomic force microscope (AFM) off-line scans.	48
Figure 55. Schematic of proposed IBAD chamber.	49
Figure 56. RHEED spot intensity for MgO film deposition stopped at the maximum and past the peak position. The best in-plane texture coincides with the peak spot intensity.	49
Figure 57a. RHEED beam is scanned from left to right at speed of the tape.	50
Figure 57b. Top view of the RHEED system showing the RHEED gun, the tape, and the RHEED screen. The RHEED beam intersects the tape at glancing incidence.	50
Figure 58. Schematic of ion scattering from a surface for <i>in-situ</i> monitoring.	50
Figure 59a. Schematic of the pulsed laser deposition chamber.	51
Figure 59b. Industrial lasers, similar to that installed at the Research Park, in a factory environment.	51
Figure 60. Bruker D8 Discover x-ray diffraction system.	52
Figure 61a. Location of a 500- μm diameter beam on a YBCO coated conductor tape.	53
Figure 61b. Pole figure of region in 61a generated in 10 minutes using Bruker D8 Discover and GADDS.	53
Figure 62a. Ac loss data on YBCO coated conductor.	54
Figure 62b. Probe for measuring ac losses in YBCO tape.	54
Figure 63. Reel to reel polishing rig designed, built, and operating at IGC-SuperPower for polishing >100 m lengths of tape.	57

Figure 64. Surface roughness profiles of (a) a manually polished tape ($R_a=1.5$ nm) and (b) a tape polished in the system shown in Figure 1 ($R_a = 2.9$ nm).	57
Figure 65a. Pilot-scale IBAD template buffer deposition facility at IGC-SuperPower. ..	57
Figure 65b. Interior view of box coater chamber.	57
Figure 66. Metal alloy substrate coated with IBAD template layer.	58
Figure 67. View of YBCO deposition chamber.....	58
Figure 68a. Phi scans of YBCO film and underlying buffer layer. The YBCO has an in-plane texture of 12 to 15° FWHM.	58
Figure 68b. Voltage/current density characteristic for a YBCO coated conductor at 77 K and self-field.	58
Figure 69. SEM micrograph (a) of a Bi-2223 filament after the initial ramp up to the processing temperature. The phases present were Bi,Pb-2212, 1:1 AEC, and the 14:24 AEC. The TEM micrograph (b) shows the transient liquid phase filling the voids between the Bi,Pb-2212 grains for a sample that was processed at temperature for 300 minutes in 7.5% O_2 prior to the quench.	60
Figure 70. TEM longitudinal cross section of a Bi-2223 filament from a tape after the full first heat treatment. A well-formed Bi-2223 colony structure occurs next to the silver sheath while porosity, second phases, and misaligned Bi-2223 grains dominate the filament interior.	61
Figure 71. SEM micrograph of a Bi-2223 tape after an intermediate deformation.	61
Figure 72. TEM micrographs of (a), the crack structure in the Bi-2223 matrix around a silver hillock and (b) the resulting structure around a silver hillock in a fully processed Bi-2223 tape. In (b), a number of basal-plane terminated grain boundaries have formed during the final sinter as a result of crack healing and the need accommodate the morphology of the silver hillock.	62
Figure 73. TEM micrograph of a Bi-2223 tape after the intermediate deformation. The failure of the matrix is illustrated by the marked crack structures.	62
Figure 74. The roughened silver interface, porosity, and secondary phases present after the final heat treatment can be (a) seen the in backscattered electron image and (b) TEM image. Both images were taken with the sample viewed in cross section perpendicular to the long axis of the tape.	63
Figure 75. EBSD data from etched Bi-2223 samples showing, a) the angular misorientation distribution for all boundaries measured <i>versus</i> only those that appear to be intercolony boundaries, and b) a representative SEM (70° tilt) micrograph with misorientations identified, showing the intracolony appearance of several low-angle ($<10^\circ$) boundaries.	64
Figure 76. TEM micrograph of a typical colony boundary in a Bi-2223 tape. The white lines indicate the portions of the colony boundary where the grain boundaries are basal-plane terminated.	64
Figure 77. Magnetic susceptibility of MgB_2 samples as a function of temperature. A constant magnetic field of 10 Oe was applied. The solid lines were used to determine the T_c s. In the inset, sample A is compared with commercial MgB_2 powder.	67
Figure 78. Williamson–Hall plots (FWHM values were obtained from the Rietveld analysis): (a) Isotropic models for Si and MgB_2 phases in samples A, B, and C. (b) Comparison of isotropic and anisotropic model for sample C. For clarity we	

have only included (00 l) and ($hk0$) Bragg reflections corresponding to the c axis and a - b plane.....	68
Figure 79. T_c as a function of the derived isotropic strain and the Mg occupancy. The results show the same dependency of T_c on both the strain and the Mg site occupancy.	68
Figure 80. Schematic circuit diagram of the Fault Current Limiter in a typical utility application.....	70
Figure 81. Model calculations of the load current in kA showing the steady state 0.5 kA peak current that rises to almost 12 kA peak immediately and has a significant dc component after the fault. The FCL limits the maximum current to only 4 kA peak on the first cycle and to 1 kA peak subsequently, with almost zero dc offset.....	70
Figure 82. Schematic of a bridge-type FCC.	71
Figure 83. The FCC located next to the NHMFL substation at Los Alamos National Laboratory after the tests in a Southern California Edison substation.	71
Figure 84. Experimental results of single-phase fault test of phase B of the FCC There is zero steady state current before the fault, which occurs at 0.2 s. The peak measured current, $i_{peak\ meas}$, during the fault was 4.28 kA.	72
Figure 85. Schematic circuit for the test setup at Southern California Edison.....	72
Figure 86. Simplified circuit diagram of the FCC during the test. The HTS coil is noted as 4 mH.	72
Figure 87. Phase angle between current and voltage during the FCC test.	72
Figure 88a. Damaged multilayer insulation near the high voltage bus at the top of the vacuum vessel. The damage was a result of an HV flashover from the HV bus to grounded parts of and in the vessel.....	73
Figure 88b. Schematic of HV bus, the cold head, MLI, AlN insulator and other components near the top of the vacuum vessel in the region where the HV flashover occurred. The vessel top plate is about 5' (about 150 cm) in diameter. ...	73
Figure 89a. Schematic of coil circuit leading to resonance and voltage doubling on the coil as a source of possible HV breakdown.	74
Figure 89b. Voltage transients measured in a circuit similar to that in the FCC to illustrate the phenomenon of voltage doubling.....	74
Figure 90a. The Paschen curve for voltage breakdown as a function of pressure times spacing. The FCC typical condition is 10^{-6} torr x 5 cm.	75
Figure 90b. Dependence of breakdown voltage on magnetic field strength at 10^{-6} torr.....	75
Figure 91a. Photograph of the of the original high voltage bus.	76
Figure 91b. Conceptual design for the new bus.....	76
Figure 92a. Test assembly used for flashover tests of the AlN disk as a function of temperature and pressure spanning the expected operating region of the FCC coil vessel.....	76
Figure 92b Finite element electrostatics analysis evaluating possible high field regions near the HV penetration of the coil vessel lid.....	76
Figure 93. Testing of vacuum and residual gas analysis of FCC coil vessel.....	77

Glossary of Acronyms

ANL	Argonne National Laboratory
AMSC	American Superconductivity Corporation
BEI	Backscatter Electron Imaging
Bi-2212	$\text{Bi}_2\text{Sr}_2\text{CaCu}_2\text{O}_8$
Bi-2223	$(\text{Bi,Pb})_2\text{Sr}_2\text{Ca}_2\text{Cu}_3\text{O}_8$
BSCCO	Bi-2212 or Bi-2223
CRADA	Cooperative Research and Development Agreement
EBSD	Electron Back-Scattered Diffraction
EDS	Energy Dispersive Spectroscopy
FCC	Fault Current Controller
FCL	Fault Current Limiter
HGMS	High-Gradient Magnetic Separator
HTS	High-Temperature Superconductivity
IBAD	Ion Beam-Assisted Deposition
IMP	Isothermal Melt Processing
I_c	Critical current of a superconductor, A
J_c	Critical current density of a superconductor, A/cm ²
LANL	Los Alamos National Laboratory
3M	Minnesota Mining and Manufacturing, Inc.
NHMFL	National High-Magnetic Field Laboratory
ORNL	Oak Ridge National Laboratory
OSTI	Oxford Superconductivity Technology, Inc.
PLD	Pulsed-Laser Deposition
PMC	Prototype Multi-Strand Cable
RBS	Rutherford Backscattering Spectroscopy
RHEED	Reflection High-Energy Electron Diffraction
SAD	Selected Area Diffraction
SCE	Southern California Edison
SEM	Scanning Electron Microscopy
SBCO	$\text{SmBa}_2\text{Cu}_3\text{O}_{7-\delta}$
SNL	Sandia National Laboratories
SPI	Superconductivity Partnership Initiative
STC	Superconductivity Technology Center (Los Alamos)
T_c	Critical temperature for superconductivity, K
TEM	Transmission Electron Microscopy
XRD	X-Ray Diffraction
YBCO	$\text{YBa}_2\text{Cu}_3\text{O}_{7-\delta}$
YSZ	Yttria-Stabilized Zirconia

Introduction

Development of High Temperature Superconductors (HTS) progressed at a rapid pace during the past year. Properties of commercially available BSCCO tapes continued to improve resulting in further reductions in cost. The superconducting properties obtained with the second generation coated conductors also showed dramatic increases in longer lengths. Power applications involving HTS prototype demonstrations in Superconductivity Partnership Initiatives further emphasized the exciting potential of these materials.

Los Alamos National Laboratory (LANL) continued to advance Bi2223 tape development by actively collaborating in the Wire Development Group led by American Superconductor Corporation (AMSC). We also partnered with Oxford Superconductivity Technology, Inc. (OSTI) in further development of Bi2212 tape conductors. Our tape processing studies involved novel thermal treatments and microstructural characterization in order to provide assistance to these companies in improving tape performance.

Our research on second-generation coated conductors based on the Ion Beam Assisted Deposition (IBAD) process combined with Pulsed Laser Deposition (PLD) of buffer and HTS layers continued with new technological breakthroughs. Our refocusing on a more commercially viable IBAD MgO template proved to be an appropriate decision with outstanding tape performance achieved. Our novel HTS multilayer technology and magnetic imaging system resulted in world record current carrying properties.

Our industrial collaborations on coated conductor development with IGC-Superpower and 3M Corporation were continued during this period. The extensive commitments with a team led by IGC-Superpower resulted in construction of a pilot scale facility at IGC that is moving towards producing long lengths of HTS coated conductor tape.

LANL continued to optimize operation of the Fault Current Controller (FCC) with successful redesign and testing of high voltage components.

Research and development activities at LANL related to the HTS program for fiscal year 2001 are collected in this report. Highlights of our technical progress are listed in Section 1, and summaries of the individual project areas appear in Section 2. Section 3 lists our 27 refereed publications, 25 papers submitted to technical journals, and 47 abstracts of conference presentations and other papers. Finally, Sections 4 to 6 contain tabulations of STC patent and license activities and collaborative agreements both active and completed.

Dean E. Peterson, Leader

Superconductivity Technology Center

1. Highlights of Fiscal Year 2001

- Demonstrated ability to produce short samples YBCO deposited on a MgO-IBAD template layer with critical current densities J_c in excess of 1 MA/cm². The J_c depends inversely on the in-plane texture, achieving these high values for YBCO phi scan full width at half maximum (FWHM) of less than 5°. Furthermore, the in-plane texture depends directly with the surface roughness, corresponding to R_{rms} of 4 Å over a 5x5 µm area.
- Successfully scaled IBAD MgO process from short sample deposition to deposition in the loop (1.1 m tape length) coater system. RHEED patterns are used to characterize the MgO texture. With ion and vapor fluences controlled to within 2% of the optimum, tapes with average MgO phi scan FWHM from 10° to 8° were achieved on roll-polished ($R_{rms} \sim 20$ Å) Inconel substrates.
- J_c versus thickness for YBCO on MgO IBAD template has reached the same level as that on formerly used YSZ IBAD, but with the template being deposited 100 times faster.
- Critical current I_c over 80 cm length of YBCO on an MgO IBAD template has been improved from 2.5 A to 14.4 A in the past year.
- YBCO/SmBCO multilayer structures eliminate the previous thickness limitation of ~1 µm for a YBCO film. The microstructure appears to degrade above 1 µm, and I_c remains relatively constant with increasing thickness for pure YBCO. The SmBCO layer stops the degradation, and allows the YBCO to renucleate on a fresh, although not planar, surface, to achieve currents of greater than 300-500 A/cm width in small samples.
- YBCO/SmBCO (Y-Sm-Y sequence) continuous process tapes using YSZ IBAD had I_{cs} of 335 A over a 5 cm section and two meter-length tapes with record I_{cs} of 142 A and 189 A.
- Optimizing the thickness of the CeO buffer layer to 90 Å on YSZ IBAD resulted in the minimum number of defect structures in the YBCO and a record J_c value of 1.7 MA/cm² for a 1.5-µm thick film. Any defects that originate in the substrate or template layer may result in chemically active regions where defect structures are more likely to degrade the YBCO film. Interfacial reactions can result in a-axis oriented grains and low J_c .
- A magnetic imaging system has been developed and used to determine the current distribution in a coated conductor tape. The system uses a hard disk drive read head that is scanned across the width of a current carrying tape. The current distribution was derived from the magnetic fields, and the presence of a defect correlated with temperature variation across the tape during the YBCO deposition.
- The Accelerated Coated Conductor Initiative has begun with the development of new laboratory facilities at the Los Alamos Research Park. The labs include tape polishing, MgO-IBAD template layer deposition, pulsed laser deposition of buffers and YBCO, and superconductivity characterization, all using reel to reel tape handling with a target of producing YBCO coated conductors in >10 meter lengths in collaboration with industrial and other external partners. Several application laboratories are also being established.

- *IGC-SuperPower, in collaboration with LANL, has constructed a pilot scale fabrication facility for YBCO coated conductors. Initial results show YBCO tapes with phi-scan FWHM values of 12-15° and J_c values in the 1-2 MA/cm² range for short samples.*
- *Microstructural analysis of the filament structure in Bi-2223 composite tapes suggests that most of the current is carried in the colony structure next to the silver sheath. Major types of defects identified in this region are chemical variation due to other phases, cracks in the matrix resulting from mechanical deformation, and basal plane terminated grain boundaries. These latter may result from inhomogeneities in the silver sheath interface.*
- *High quality MgB₂ bulk samples were affected only slightly (2 K (~5%) drop in T_c) by large (1%) anisotropic strains and Mg vacancies of ~5%, both obtained by varying the synthesis conditions.*
- *Analysis of the General Atomic Superconductivity Partnership Initiative Fault Current Controller found that it had suffered no HTS coil damage during initial substation testing in 1999. Electrical breakdown failure mechanisms were identified, and a feasible repair and restoration plan was developed. A new high voltage bus was designed and plans to improve other systems were developed. The National High Magnetic Field Laboratory at LANL was identified as the site for restoration and testing.*

2. Technical Activities

2.1 Wire Technology

2.1.1 MgO IBAD Templates for YBCO Coated Conductors

(P.N. Arendt, S.R. Foltyn, J.R. Groves, T.G. Holesinger, H. Kung, Q.X. Jia, V. Matias, E.J. Peterson, L.A. Emmert, R.F. DePaula, P.C. Dowden, J.Y. Coulter, L. Stan)

Preparation of high temperature superconductors on flexible metal substrates for advanced applications like transmission wires, motor windings, or magnets requires lengths of material with the ability to carry sufficient current. Bi-based superconductors have been successfully produced in long lengths using the oxide-powder-in-tube (OPIT) method for some time. However, these superconductors are limited in their application due to their high anisotropy that results in a low irreversibility field at 77 K despite the fact that they have such high superconducting transition temperatures (90 K and above). $\text{YBa}_2\text{Cu}_3\text{O}_{7-\delta}$ (YBCO) when deposited on single crystal substrates, shows high critical current densities ($>10^6$ A/cm² at 77 K) and superior irreversibility as compared to the Bi-based superconductors. However, YBCO exhibits a weak-link behavior in superconducting transport properties as a function of grain boundary alignment. As a result, deposition of such films on metallic polycrystalline substrates, which provide a robust platform for long length deposition and high mechanical strength for device integration, is problematic.

Several groups have approached the adaptation of YBCO to long length coated conductor development with differing degrees of success. One of the successful techniques has been the use of ion-beam assisted deposition (IBAD) to grow a biaxially textured film of yttria-stabilized zirconia (YSZ) on mechanically polished nickel alloys for subsequent pulsed laser deposition (PLD) of YBCO. At LANL, the use of this process has resulted in the fabrication of one-meter long coated conductors with critical current densities (J_c) of 1 MA/cm² or better for YBCO films ≥ 1 μm . The IBAD YSZ process develops texture by an evolutionary grain growth competition process that requires between 500 to 1000 nm of material to achieve an in-plane texture with a phi scan full width at half maximum (FWHM) of 12°. A small FWHM value is necessary for high performance conductors because large angle grain boundaries reduce the critical current density significantly.

One drawback to the commercialization of the process to lengths in excess of one meter has been the amount of time required to deposit the IBAD YSZ. A typical deposition takes ~20 hours per meter of tape. In 1997, researchers at Stanford found that comparable in-plane texture could be developed using the IBAD process with magnesium oxide (MgO). The major difference between the two material systems is the mechanism that controls the texture development. As mentioned above, IBAD YSZ has an evolutionary texture development character while IBAD MgO requires ~10 nm to develop similar texture. Since the deposition rates for the two materials are comparable, this texturing mechanism translates to a process that is ~100 times faster than that of IBAD YSZ. The dependence of texture development on time (proportional to thickness) is shown in Figure 1.

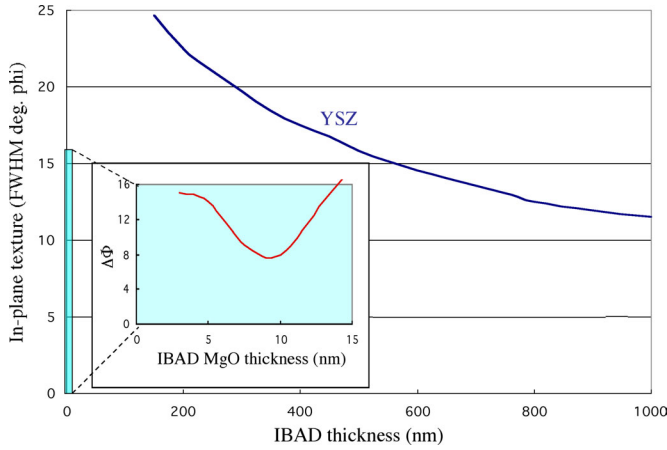


Figure 1. Comparison of in-plane texture development as a function of template layer thickness for IBAD YSZ and IBAD MgO (inset).

There are two extra layers required in the HTS coated conductor materials system using the MgO template versus those needed when using YSZ. One is the 0.5 nm thick amorphous Si_3N_4 nucleation layer and the other is the PLD YSZ buffer layer. Neither of these layers is expected to add to the total deposition time or cost in an industrial setting as they can be readily accommodated in the deposition sequence by adding additional stations. A second requirement of the IBAD MgO is that the surface of the metal substrate platform has a finish of $R_{\text{rms}} < 2$ nm. Although we currently achieve this finish by mechanically polishing meter lengths of metal substrates, we believe that kilometer lengths of tape will be more efficaciously prepared using electropolishing techniques. For substrates electropolished in stationary mode (10 cm pieces), we have achieved $R_{\text{rms}} < 1$ nm and are currently adapting this process to polish multiple meter lengths.

A beneficial enhancement of the in-plane texture is also observed in the YBCO film deposited onto the buffered template layer. Figure 2 shows that for a YSZ template layer, the enhancement (decrease in the phi scan FWHM) of 5° or more, or about 33%, from $\sim 15^\circ$ in YSZ to less than 10° in YBCO. The reason for this enhancement is that the measured FWHM of the YSZ layer is an average through the thickness, and the FWHM is gradually decreasing with thickness. Thus, the surface of the YSZ layer actually has a smaller FWHM than the bulk. Therefore, the thin buffer layers and the YBCO layer, which grow on the surface of the YSZ layer, are expected to reflect this FWHM. For MgO, the decrease is from a FWHM of 7° in MgO to $\sim 6^\circ$ in the YBCO, which represents a fractional decrease of $\sim 15\%$. The decrease in the FWHM is much smaller for IBAD MgO because the “bulk” and surface texture are essentially the same, in contrast to the case for IBAD YSZ. Because the transport J_c of YBCO decreases exponentially with phi FWHM, these decreases in FWHM from template film to YBCO both yield substantial, beneficial improvements to the J_c performance.

Figure 3 shows a schematic of the research chamber for depositing the MgO IBAD template film. An electron-beam gun evaporates the MgO and creates a flux of molecules normal to the substrate. Simultaneously, the ion assist gun provides a flux of Ar ions at a 45° angle between the MgO beam and substrate surface. The reflection high-energy electron diffraction (RHEED) gun provides a probe beam of electrons at glancing incidence ($\sim 1^\circ$ to 5°) to the substrate surface. The phosphor screen detects the diffracted electrons by fluorescing, and the light is recorded by the charge-coupled device (CCD) camera.

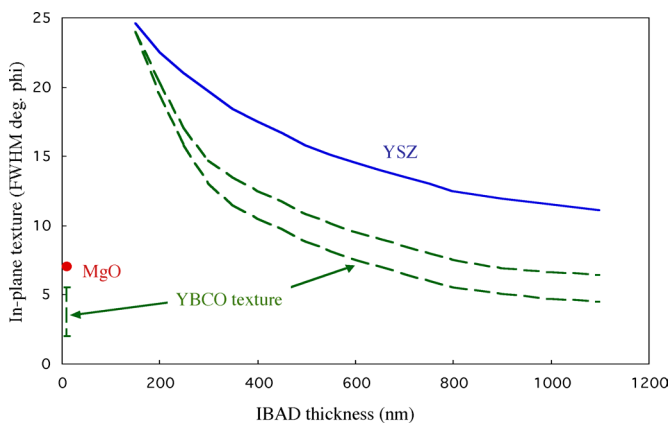


Figure 2. Improvement of YBCO in-plane texture (phi scan FWHM) relative to that of YSZ or MgO template layer textures.

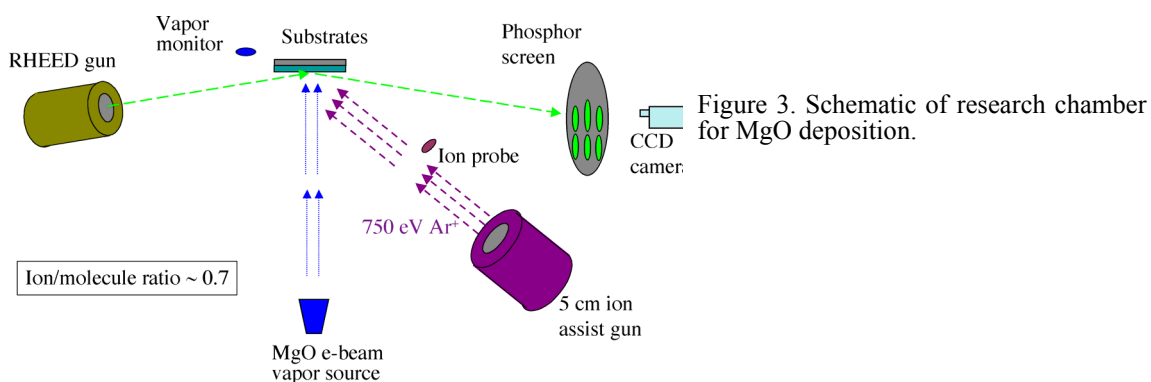


Figure 3. Schematic of research chamber for MgO deposition.

Figure 4 shows the usefulness of RHEED patterns for monitoring the quality of the film during deposition. The best “spots” (Figure 4b), characteristic of a single-crystalline like film, i.e., one with both good out of plane and in-plane texture, are seen for IBAD MgO deposited on α - $\text{Si}_3\text{N}_4/\text{Si}$, that is, on single-crystal silicon substrate with an amorphous layer of silicon nitride. Without the ion assist, Figure 4c, the pattern consists of rings, characteristic of a film with random in-plane texture.

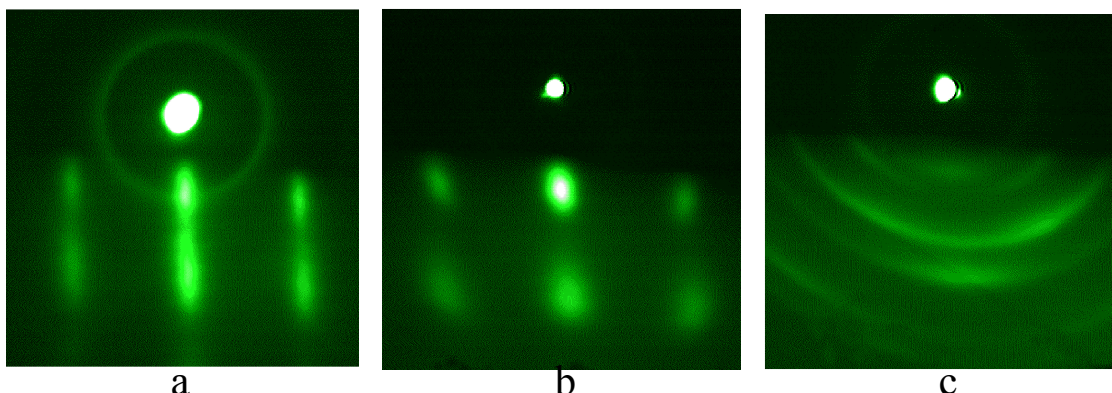


Figure 4. RHEED patterns for MgO. (a) Rod-like pattern for IBAD MgO deposited homoepitaxially on single crystal MgO; (b) spot-like pattern for IBAD MgO deposited on crystalline Si with an amorphous layer of Si_3N_4 ; and (c) ring-like pattern for MgO deposited on α - $\text{Si}_3\text{N}_4/\text{Si}$ by e-beam with no ion assist beam.

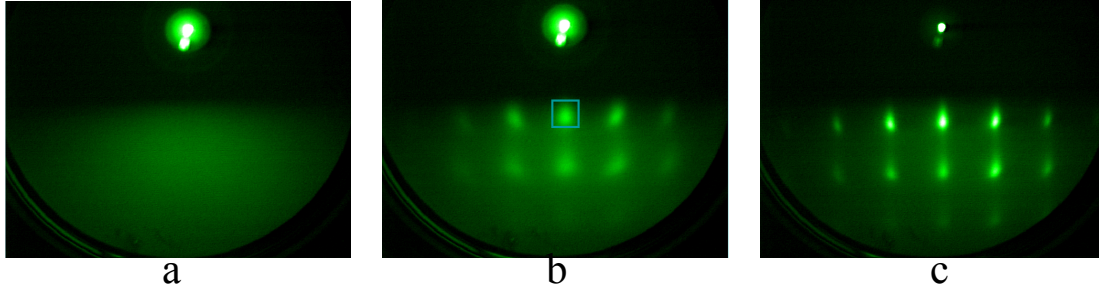


Figure 5. Evolution of RHEED patterns during IBAD MgO film growth. (a) a - $\text{Si}_3\text{N}_4/\text{Si}$ before starting growth; (b) after IBAD MgO deposition; (c) after homoepitaxial MgO film deposition.

Evolution of the MgO growth morphology is reflected in the RHEED pattern as shown in Figure 5. Starting from the amorphous layer of Si_3N_4 on the silicon substrate, there is only a diffuse pattern. After deposition of the 40-50 Å thick IBAD MgO layer, spots have clearly emerged. Finally, after deposition of a homoepitaxial layer of MgO (with no ion assist), the spots sharpen considerably. The continuous evolution of the MgO d-spacing of the (002) peak is shown in Figure 6. It expands somewhat during the IBAD process, indicating the presence of appreciable lattice strain. However, it then relaxes back to the bulk value of 4.21 Å with the deposition of about 400 Å of homoepitaxial MgO. (after V. Matijasevic, Conductus, 1998)

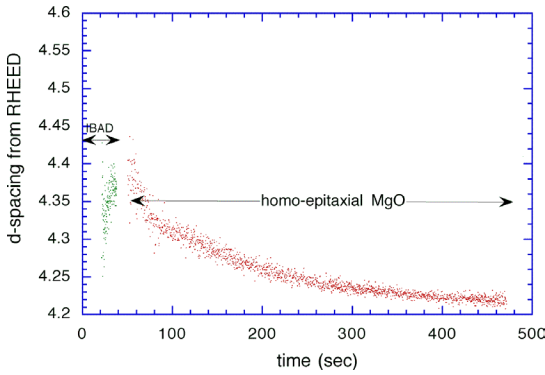


Figure 6. Evolution of d-spacing observed by RHEED during deposition of IBAD and homoepitaxial MgO.

Another potential problem associated with the deposition of IBAD MgO is a tilting of the c axis away from the surface normal. This can be seen (Figure 7) by observing the RHEED pattern with the RHEED beam oriented perpendicular to the ion beam direction. What is observed is that the c axis of the MgO film tilts progressively away from the surface normal as the film gets thicker. Figure 8 shows that this trend continues at least out to an IBAD MgO film thickness of 1000 Å (100 nm), at which point the tilt angle is nearly 30°. With this large a tilt angle, the RHEED pattern deteriorates from its optimum, and the growth of highly in plane textured YBCO is no longer possible. Thus the maximum thickness of MgO is limited to ~100 Å.

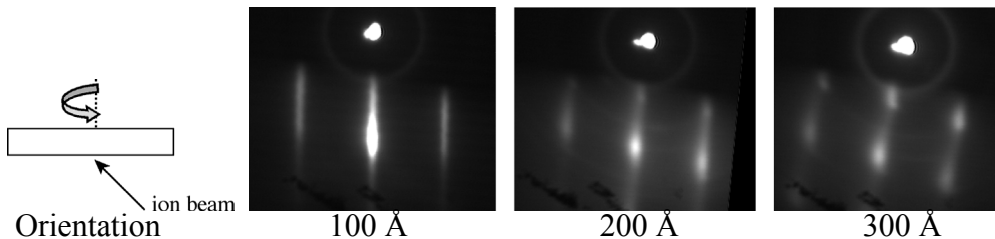


Figure 7. RHEED patterns showing tilting of spot pattern increasing with thickness. The orientation of the RHEED beam is 90° rotated from the direction of the ion assist beam.

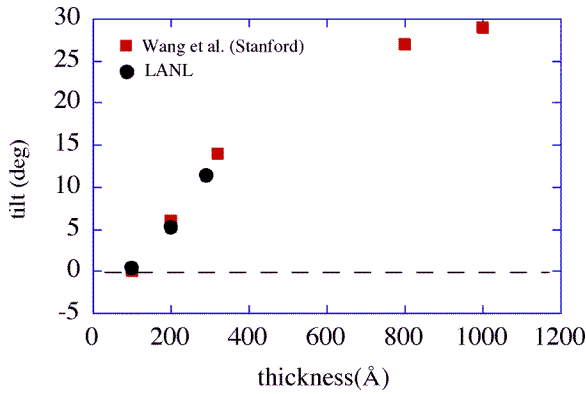


Figure 8. Tilting of the c axis away from the MgO film normal as a function of film thickness. Results at LANL were confirmed and expanded by workers at Stanford University.

A possible microstructural mechanism for this tilting of the c axis away from the perpendicular is the generation of radiation-induced dislocations in the IBAD MgO. Figure 9 illustrates this mechanism. The top portion of Figure 9a shows that the presence of (radiation induced) dislocations in the MgO results in a shift of the lattice planes by an angle $\theta = b/(l\sqrt{2})$, where b is the lattice spacing and l is the distance between dislocations. The bottom of Figure 9a shows the region near the dislocations. A 5° tilt in a 200 Å thick film requires about 10^{17} dislocations/cm². In support of this thesis, TEM images of a MgO film also indicate that interstitial point defects can coalesce into $\{110\}$ -type planes.

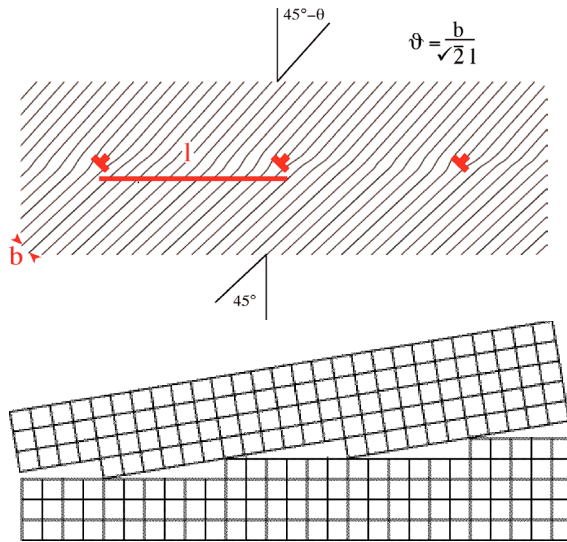


Figure 9a. Model for tilting in IBAD MgO. The top portion of the figure shows the effect of dislocations to form the tilt. About 10^{12} dislocations/cm² in 200 Å allows a 5° tilt to result. The bottom portion of the figure shows the region near the plane of dislocations.

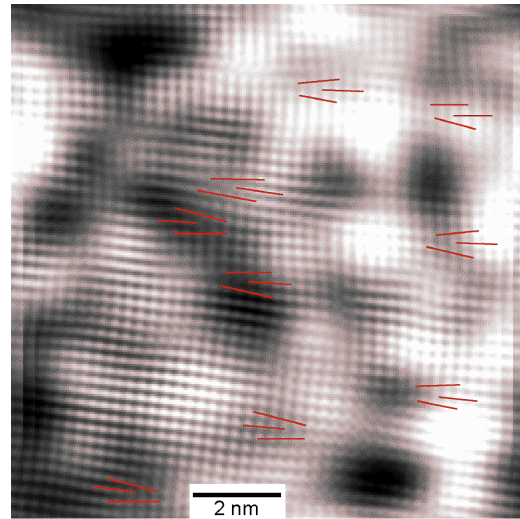


Figure 9b. TEM micrograph of a MgO film. The bars indicate areas where interstitial point defects coalesce to form $\{110\}$ -type planes.

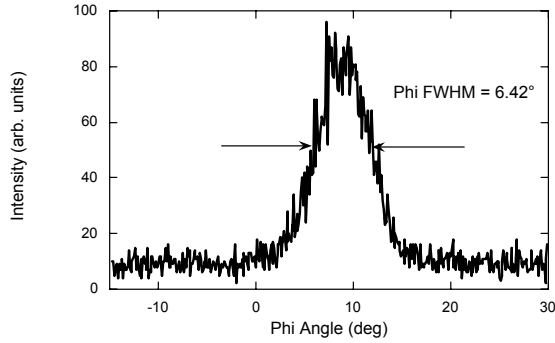


Figure 10. X-ray intensity vs. rocking curve angle ϕ for a homoepitaxial layer of MgO deposited on IBAD MgO/ α -Si₃N₄/Hastelloy C276 substrate. A FWHM of less than 7° has been achieved.

Based on the above work and using a combination of the calibrated RHEED intensity vs. time curve and XRD results allow for the optimization of IBAD MgO in-plane texture, as seen in Figure 10.

The substrate surface roughness also plays a major role in achieving good texture and good performance of the YBCO. This dependence can be seen in Figure 11. The substrate surface roughness, R_{rms} , is measured over a 5 μm x 5 μm region of the Hastelloy C276 polished substrate using an atomic force microscope (AFM). The critical current density was measured on the YBCO film with the layer sequence: YBCO/CeO₂/YSZ/homoepi-MgO/IBAD MgO/ α -Si₃N₄/Hastelloy-C276. There is a direct correlation between surface roughness and ϕ scan FWHM; because of the inverse dependence of the critical current density on the FWHM, there is a critical need to achieve very good surface roughness to achieve high J_c values. As the roll polisher for meter length tapes in service at present has a lower limit of R_{rms} of about 30 Å, different techniques are under development to achieve better surface properties and ultimately higher critical current densities.

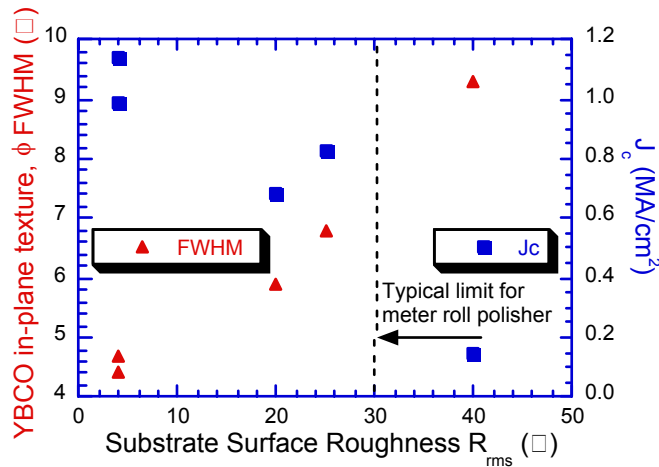


Figure 11. YBCO in-plane texture (ϕ -scan FWHM) and critical current density J_c as a function of substrate surface roughness R_{rms} .

All of the results discussed above were achieved with the sample in a small coating system (batch mode processing). The next step to producing longer length samples is to transfer the MgO IBAD deposition technology to a loop coating system. This is shown schematically in Figure 12a. The main differences from the research chamber shown in Figure 3 are the much larger ion assist source, the use of an ion sputter gun rather than an

e-beam to produce the MgO vapor, and the substrate transport system. This system can deposit MgO at 1/4 the rate of the research chamber. Details of the region near the tape are shown in Figure 12b.

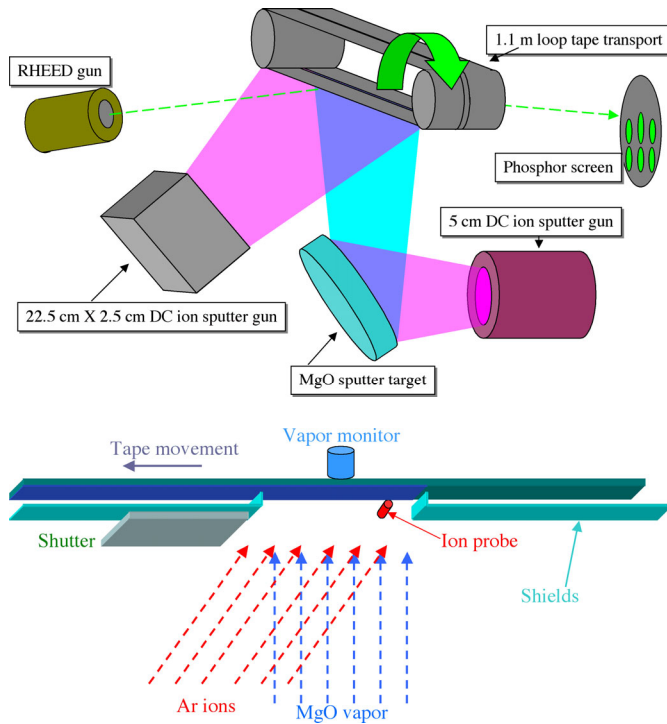


Figure 12a. Schematic of IBAD loop coating system

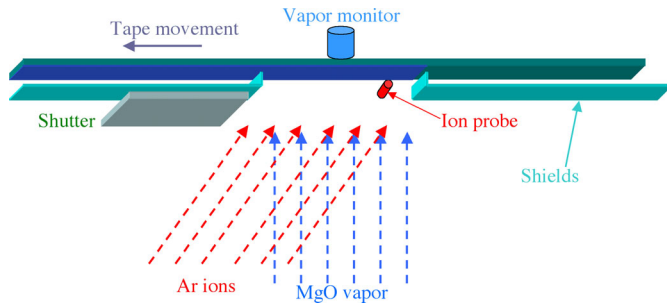


Figure 12b. Expanded view of region near the tape. The system can be used for small samples attached to moving tape or for a long length tape.

This apparatus can be operated in several modes. With samples, e.g., α -Si₃N₄/Si wafers pasted to the tape can be moved into the deposition zone with the shutter closed. The shutter is then opened for the deposition, closed again, and the next sample moved into position. The deposition parameters can be changed for each sample, thus many different conditions can be explored in one pump-down of the system. In addition, continuous deposition on the 1.1 m loop of tape can also be performed with the shutters opened wider than for the small stationary samples.

RHEED images can also be obtained during continuous processing of the tape. Figure 13 shows several images spaced over a 2 cm length of the tape. The beam sweep is less than the width of the deposition window (~10 cm), so the pattern is quite similar from point to point, the largest variation being due to slight variations of the tape position (plane and angle of tape).

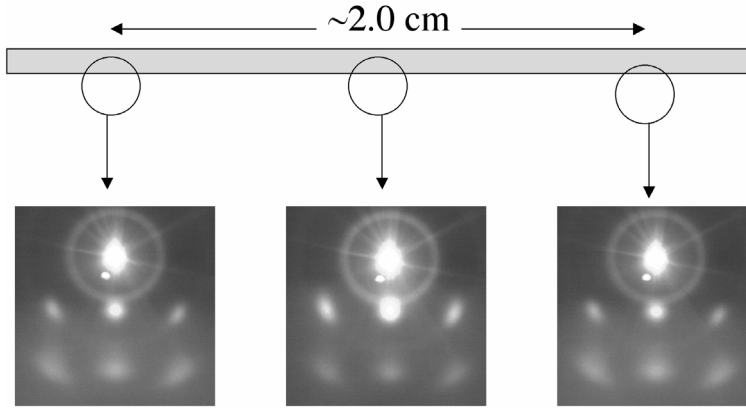


Figure 13. RHEED patterns on moving tape.

Figure 14 shows the initial meters coated in the continuous process system (a) and with various improvements, including controlling the ion and vapor fluences within $\pm 2\%$ of the optimum values. All of these tapes were produced using roll-polished Inconel 625 with an α - Si_3N_5 buffer and were overcoated with homoepitaxial MgO. The average $\Delta\phi$ values of the most recently coated meters are 9.8, 8.1, 7.8 (Figure 14b), 9.3, 9.2, 7.8, 8.6, and 9.3° .

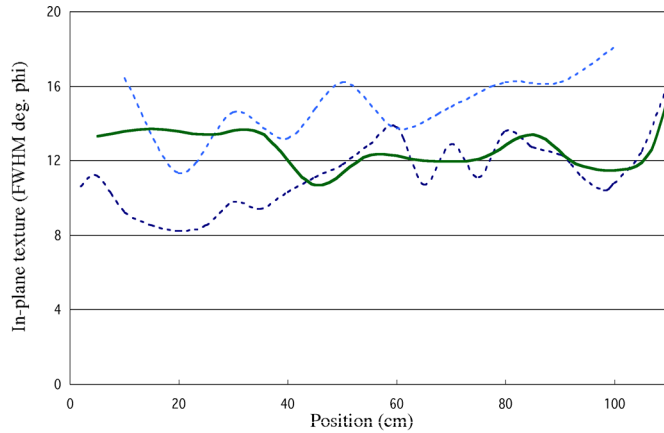


Figure 14a. Texture of IBAD MgO for two tapes not using the RHEED system (dashed curves) and with RHEED and two passes through the deposition zone (solid line).

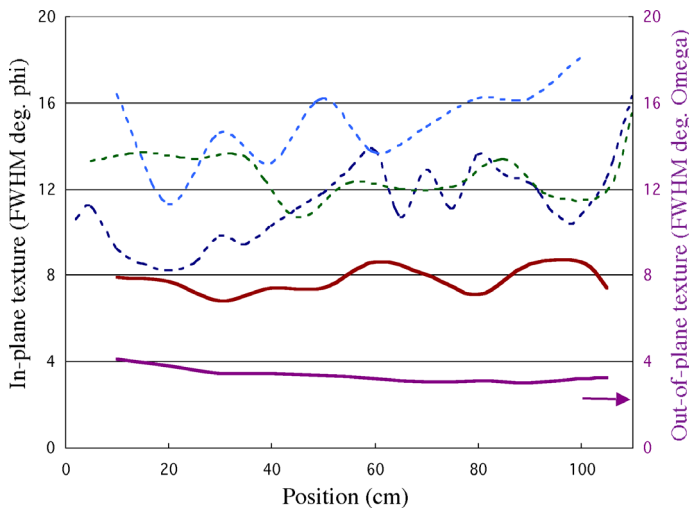


Figure 14b. After several refinements, the texture quality and repeatability of the IBAD MgO tapes increased remarkably.

There are some interesting differences in the microstructure between IBAD YSZ and IBAD MgO that have been discovered during the course of this work. Figure 15 shows plan view dark field TEM images of a YSZ layer (a) and an ion beam sputtered MgO layer (b). The YSZ film shows an average sub-grain size of 5 nm and micrometer size colonies of well-aligned grains. In contrast, the IBAD MgO film shows a much larger average grain size of ~50 nm, but a smaller colony size of ~200 nm.

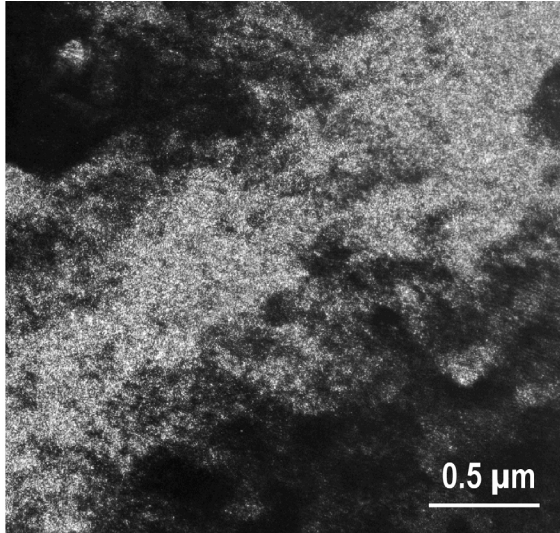


Figure 15a. TEM dark field micrograph of IBAD YSZ.

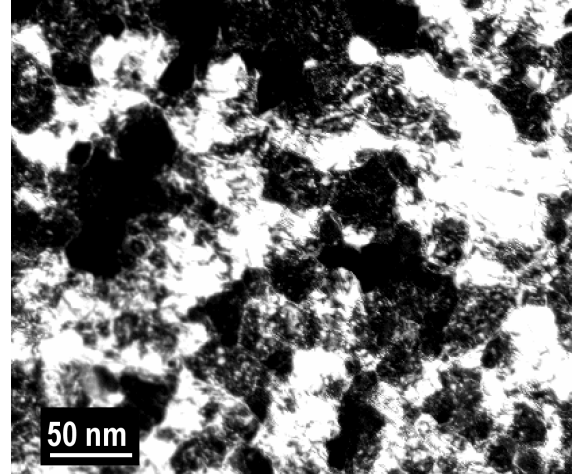


Figure 15b. TEM dark field micrograph of ion beam sputtered IBAD MgO.

The smaller size of the MgO colonies, compared to those of YSZ, does not appear to be solely a result of the deposition method. Plan view bright field TEM of e-beam evaporated IBAD-MgO shown in Figure 16 shows similar grain size and somewhat smaller colony size (~10 nm) than for ion sputtered films.

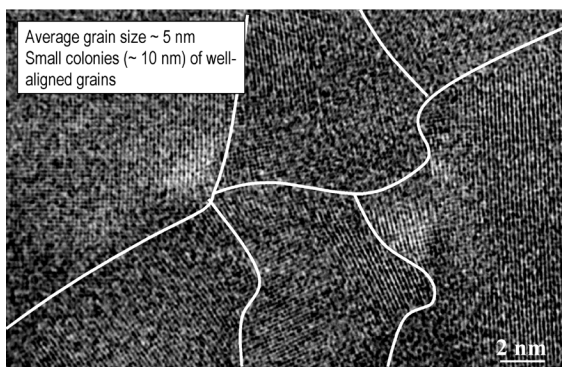


Figure 16. Bright field TEM image of e-beam evaporated IBAD-MgO.

Electrical performance of YBCO films on this new template is also quite good and is improving with time. The average values of I_c and J_c on 24 recent microbridges patterned on continuously processed meter lengths are 125 A/cm width and 0.89 MA/cm², respectively, for an average thickness of 1.44 μm. Results on 1 cm x 4 cm strips are 73 A and 93 A for I_c and 0.49 and 0.62 MA/cm² for J_c on 1.5 μm thick YBCO films. It is of interest to compare the critical current density of the YBCO films on metal substrates using IBAD YSZ or IBAD MgO templates. Figure 17 shows the most recently obtained

J_c values on microbridges as a function of YBCO film thickness. The most important message from this figure is that the IBAD MgO templates yield the same level of superconductor performance as the YSZ templates. However, IBAD MgO provides this performance at 100 times the processing speed of IBAD YSZ. This is extremely important in terms of reducing cost for producing second generation, coated conductors.

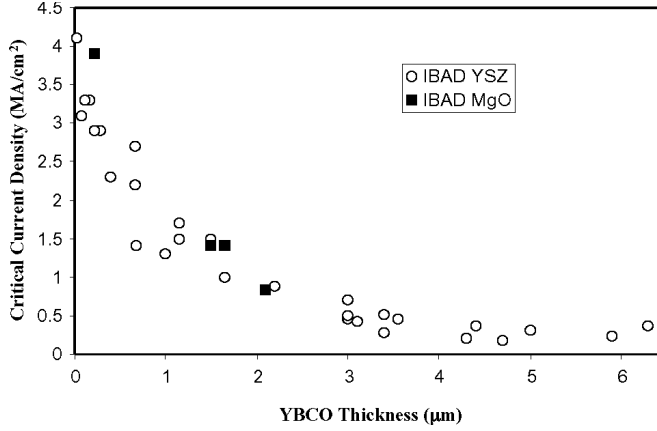


Figure 17. Dependence of critical current density on YBCO thickness for films deposited using IBAD YSZ and IBAD MgO template layers.

Measurements on meter-length samples of YBCO on IBAD MgO to date indicate substantial year to year progress, as shown in Figure 18. The end-to-end I_c at 75 K and self field has been increased from 2.5 A to 14.4 A over the past year. The performance achieved on meter length IBAD MgO templates is comparable to that achieved on IBAD YSZ templates after four years of development. For IBAD YSZ, this occurred in 1997.

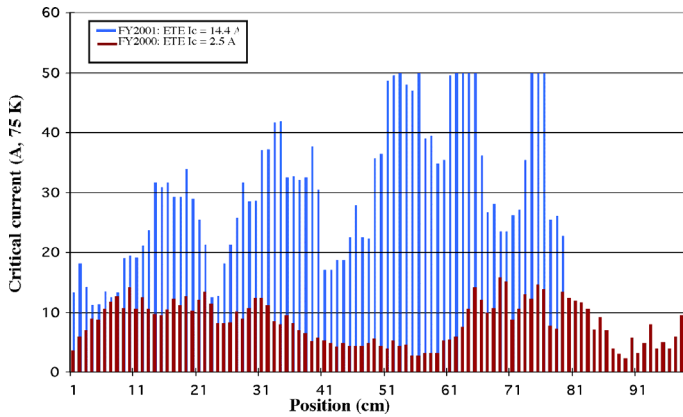


Figure 18. Critical current as a function of position for YBCO on meter length IBAD MgO templates produced in 2000 and 2001.

To summarize results in the past year, the following accomplishments have been made. RHEED/x-ray diffraction has been used to optimize the deposition parameters for IBAD MgO template layers. These optimized deposition parameters have been successfully transferred to continuous-mode processing for 1.1-meter loops of metal substrates. Further research has shown that the IBAD MgO in-plane texture is sensitive to substrate surface roughness and IBAD MgO thickness. The critical thickness (~ 10 nm) has been identified and polishing processes are being optimized to reduce surface roughness (< 2 nm R_{rms}) to improve IBAD MgO template texture. Good texture on continuously processed meter lengths of IBAD MgO templates without the need for RHEED monitoring (best: $\Delta\phi_{ave} = 7.8^\circ$, $\Delta\omega_{ave} = 3.3^\circ$) has been demonstrated Run-to-run texture repeatability with an average $\Delta\phi \sim 8.8^\circ$ over meter lengths (FY2000: $\Delta\phi_{ave} \sim 20^\circ$) has

also been demonstrated. Using continuously processed IBAD MgO, 24 bridge samples with $I_{cave}(75\text{ K, SF}) = 125\text{ A/cm width}$, $J_{cave}(75\text{ K, SF}) = 0.89\text{ MA/cm}^2$; 4 x 1 cm samples with best $I_c(75\text{ K, SF}) = 93\text{ A}$ have been produced. The best YBCO/IBAD MgO tape result is $I_c(75\text{K, SF}) = 14.4\text{ A}$ for an 80 cm length.

Future issues for the program include improving the performance of YBCO/IBAD MgO meters to be comparable to that of YBCO/IBAD YSZ meters, simplifying the buffer layer stack, demonstrating a less than 5 minute/meter deposition time for IBAD MgO, and investigating non-RHEED methods for optimizing IBAD MgO.

2.1.2 High Current Coated Conductors Based on IBAD YSZ and Thick YBCO/Sm-123 Multilayers

(S.R. Foltyn, Q.X. Jia, P.C. Dowden, P.N. Arendt, J.F. Smith, T.G. Holesinger, H. Kung, J.Y. Coulter, B.J. Gibbons, D.B. Jan, R.F. DePaula, L. Stan, and J.R. Groves)

Research on thick YBCO coated conductors is critically important to the development of this technology for a number of reasons. The first is that the decrease in the critical current density J_c in an applied magnetic field requires that to achieve 100 A/cm width in a 1 T magnetic field B perpendicular to the tape plane ($B \parallel c$) at 77 K, a self field critical current I_c greater than 500 A/cm is required. For many applications a high engineering critical current density J_c is required. To achieve a J_c of 0.1 MA/cm² requires an I_c greater than 500 A/cm on a 50- μ m thick substrate. Thus it is necessary to explore the limits of the coated conductor technology to achieve these practical goals.

Our earlier work (Appl. Phys. Lett. 75 3692 (1999)) showed that there was an apparent I_c limit of about 200 A/cm-width for coated conductors that was reached at a thickness of about 1.5 μ m. This result is shown in Figure 19.

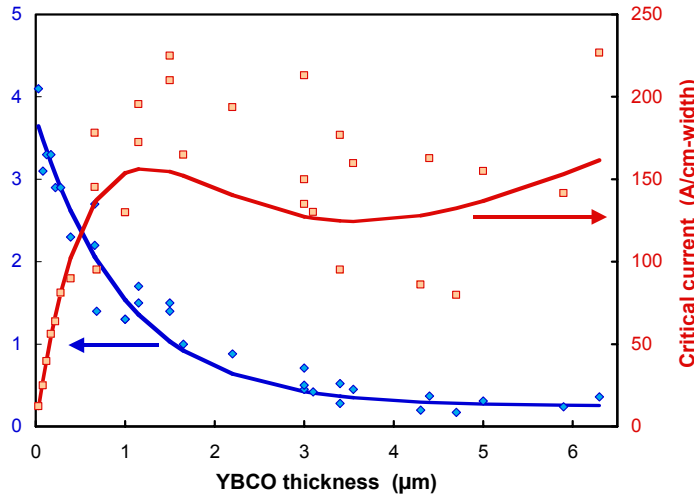


Figure 19. Critical current density and critical current of PLD YBCO on Inconel substrates with Y_2O_3 - or CeO_2 -buffered IBAD YSZ template layer. The bridge dimensions are ~ 0.2 mm x 5 mm.

In an effort to understand the source of this dependence of I_c on thickness, ion milling experiments were carried out. Three samples were thinned in steps followed by a critical current measurement. The result (Figure 20) indicates that little or no current flows in the upper layers. All of the current flows in the ~ 1.5 μ m thickness of the film closest to the substrate. The results of scanning electron microscopy (SEM) analysis of the cross section and plan views of the YBCO are shown in Figure 21. The plan views show increased roughening with thickness. This correlates with the increased porosity observed in the cross section micrograph in Figure 21. The microscopy results are consistent with the low current density in the upper layers illustrated in Figure 20.

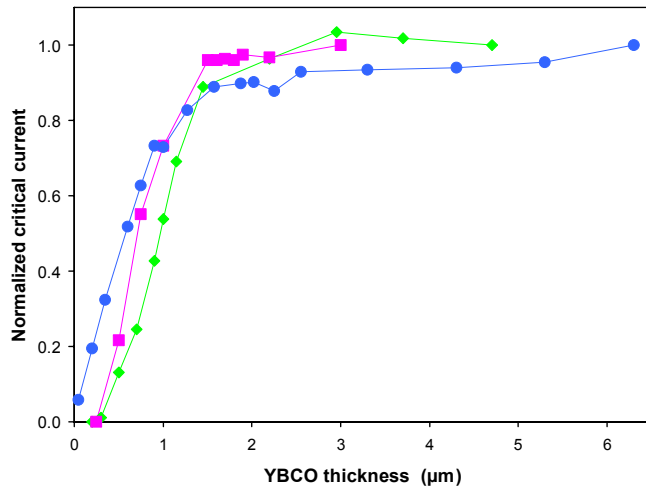


Figure 20. Critical current normalized to the initial value as a function of thickness for three YBCO samples thinned progressively.

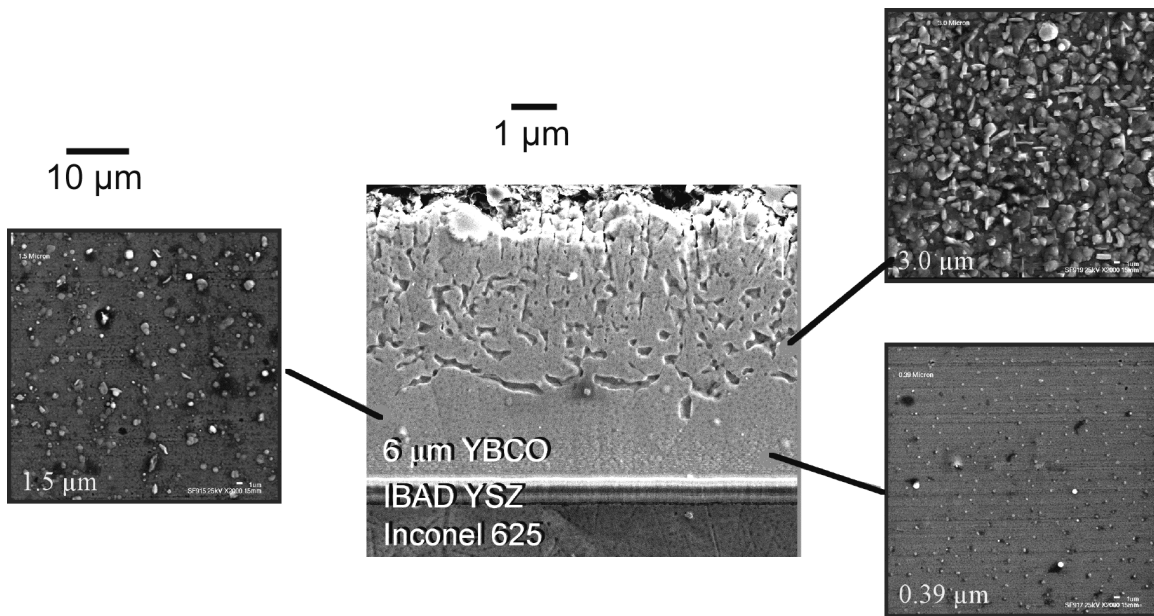


Figure 21. SEM Cross section (center) and plan view images (sides) at various levels throughout the thickness of a YBCO film.

As an attempt to eliminate the progressive roughening and porosity, a multilayer stack of YBCO interleaved with layers of SmBCO was grown. SmBCO by itself has a relatively low critical current density. In addition, it requires a higher deposition temperature (835°C compared to 790°C for YBCO) when deposited onto single crystal SrTiO₃. For a 0.25 μm-thick layer of SmBCO on single crystal SrTiO₃, the best J_c obtained was 0.88 MA/cm²; in contrast, YBCO would be 4.5 MA/cm² under the same conditions. However, it forms as a very smooth film. The SmBCO layer appears to "reset" the growth morphology of the YBCO. As a result, dense YBCO layers can be grown, and in the case of the structure shown in Figure 22a, to a total thickness of about 3 μm. From the backscattered electron SEM image on the right side of Figure 22a, the dense layers of

YBCO can be seen. However, it is clear that the SmBCO does not planarize the surface; the contour of the lower YBCO surface is faithfully reproduced in the SmBCO layer. The detailed mechanism for the improved YBCO properties is still under investigation.

Figure 22 (b) and (c) show plan view SEM images of the surface of two films of comparable thickness prepared by the standard process and by the Y/Sm multilayer process, respectively. The surface is remarkably smoother and denser with the Y/Sm process. Furthermore, the critical current density and current density per centimeter width are roughly twice as large using the Y/Sm multilayer process. This has allowed a major breakthrough to pass the level or 200 A/cm width, as extrapolated from these measurements on small (0.2 mm x 5 mm) samples.

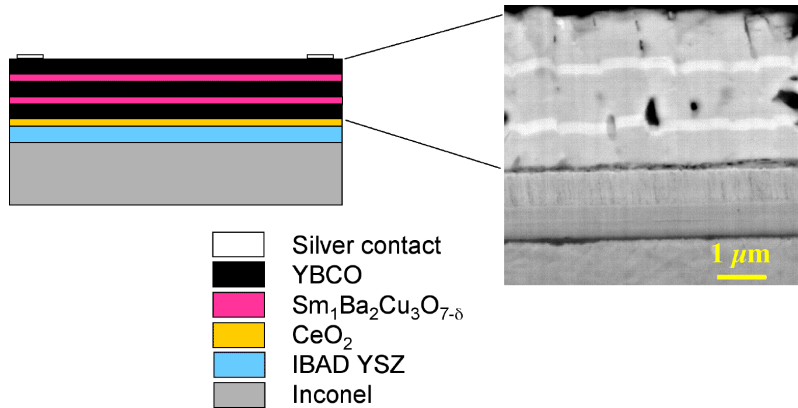
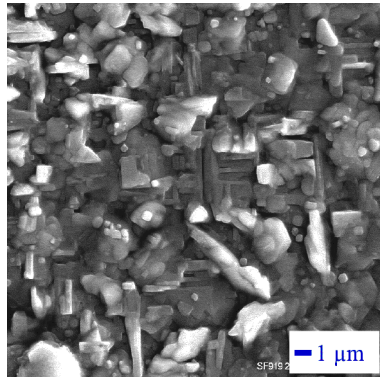
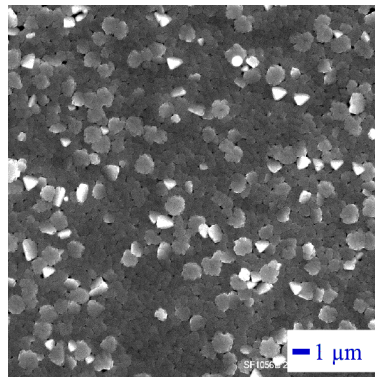


Figure 22. (a) Stacking sequence of the Y-Sm-Y multilayer film. The YBCO and SmBCO layer thicknesses are about 1.0 μm and 0.2 μm , respectively.



(b)



(c)

SEM plan views of the YBCO film surface. (b) Standard process: 3.0 μm thick, $J_c = 0.6 \text{ MA/cm}^2$, $I_c = 180 \text{ A/cm width}$. (c) Y/Sm-BCO multilayer process: 3.7 μm thick, $J_c = 1.1 \text{ MA/cm}^2$, $I_c = 405 \text{ A/cm width}$.

A number of small samples were produced by the Y/Sm-BCO multilayer process at various YBCO total thicknesses to explore the trends and potential for this process. The results are shown in Figure 23. All the results for samples made by the standard process lie roughly between 100 and 200 A/cm width. In contrast, the films made by the modified process all lie above the 300 A/cm width contour, with some as high as 500 A/cm width.

Exploring the dependence of critical current density and critical current per cm width on the total number of layers for fixed overall film thickness of 5.8 μm , it was found that saturation was reached above about 5 layers. At 5 layers, the YBCO thickness is about 1.5 μm , seen to be the thickness limit for a single layer as shown earlier.

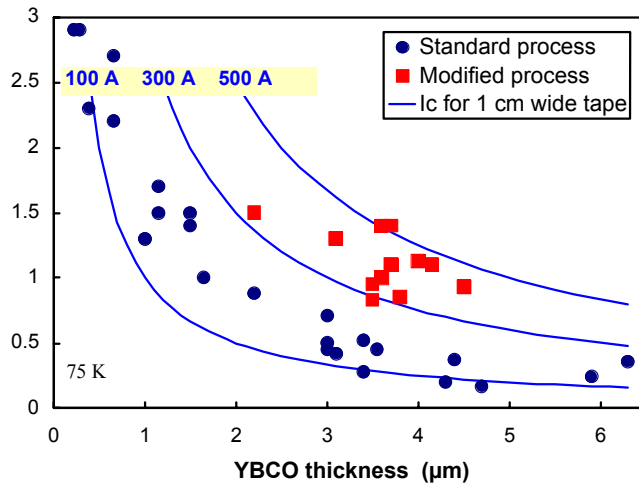


Figure 23. Critical current density as a function of YBCO film thickness for samples produced by the standard process and by the modified (Y/Sm-BCO multilayer) process. Also shown are contours of constant current per centimeter width. Inconel 625 substrate with YSZ IBAD; sample size is 0.2 mm x 5 mm.

Also, it was found that the critical current for films of 5 μm YBCO thickness is a decreasing function of SmBCO layer thickness. A typical Y/Sm-BCO multilayer film also shows lower resistivity and a higher superconducting transition temperature than a single layer film of comparable thickness, as shown in Figure 24. Finally, comparing the critical current as a function of YBCO film thickness for single and multilayer structures, Figure 25, it is clear that for a single layer film, all the current is carried in the first ~ 1.5 μm of thickness. However, for the multilayer structure, this is not a limit and in fact, the current density increases at a rate of 60 A/cm-width per micrometer of thickness above 1.5 μm .

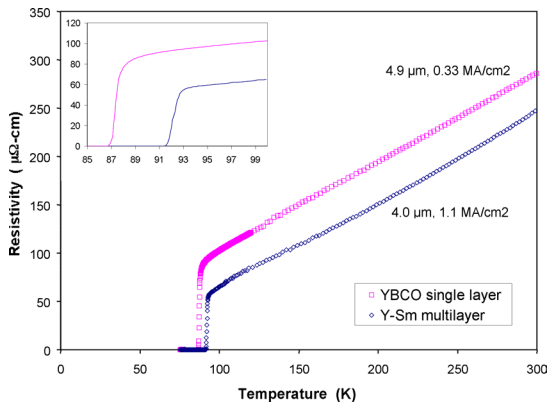


Figure 24. Comparison of resistivity and superconducting critical temperature of a YBCO single layer and Y/Sm-BCO multilayer film.

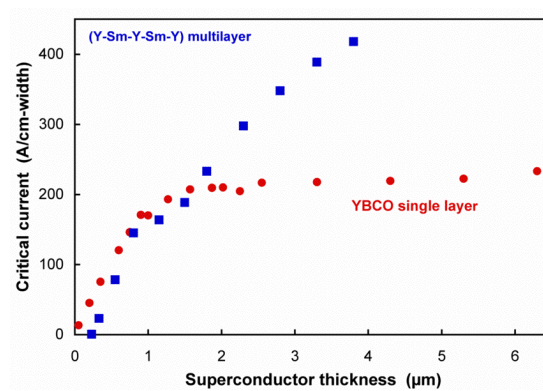


Figure 25. Comparison of single and multilayer films at 75 K as a function of YBCO thickness. Above ~ 1.5 μm , the I_c of the multilayer structure increases at a rate of 60 A/cm width/ μm

The next stage of development was to verify this modified process on full 1-cm width IBAD tapes. However, the source for high quality YSZ IBAD at LANL was no longer available. The LANL IBAD effort has been focused on MgO IBAD over the last few years. This process has the promise to be much faster than the one using YSZ; however, to date, the performance of YBCO on meter length tapes has not been as good with MgO. Therefore, it was decided to purchase YSZ IBAD coated flexible tapes commercially from Zentrum für Funktionswerkstoffe gGmbH (ZFW) in Göttingen, Germany.

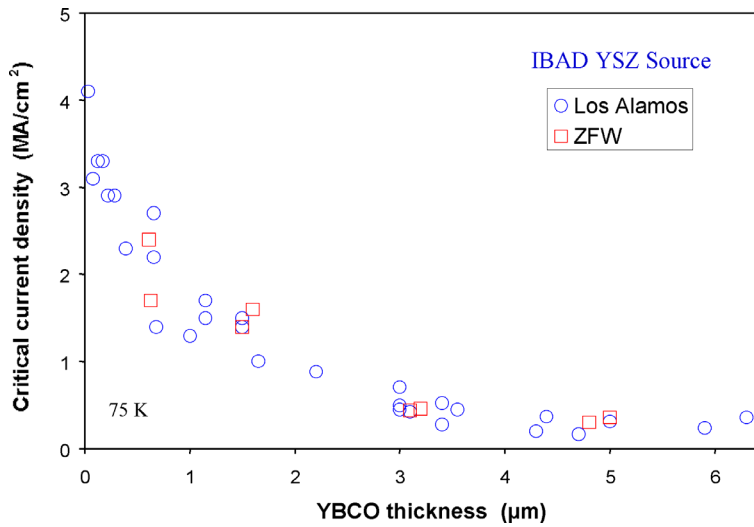


Figure 26. Comparison of YBCO standard process coated conductors on Inconel 625 with either LANL or ZFW YSZ IBAD. The IBAD layer was buffered with Y_2O_3 or CeO_2 .

Figure 26 shows that YBCO deposited on both LANL and ZFW YSZ IBAD, buffered with Y_2O_3 or CeO_2 , using the standard (single YBCO layer) process have comparable performance.

For the transition to the PLD tape-coating chamber, a conservative three-layer design (Y-Sm-Y) was used. One meter long YSZ IBAD tapes from ZFW were first buffered with CeO_2 . The multilayer structure was deposited to a superconductor thickness of $2.0\ \mu\text{m}$. This tape had a self field, 75 K critical current of 142 A. However, the second tape deposited showed periodic variations in the local (1 cm gauge length) I_c that indicated a problem with the deposition temperature. The data and the good correlation are evident from Figure 27. However, even with this temperature problem, the overall (end-to-end) I_c at 75 K and self field was a record value of 189 A. At 0.6 T magnetic field ($B \parallel c$), the lowest valley, which determines full-length I_c is 35 A, and the peaks in the distribution are at 65 A. This latter value corresponds to a self field I_c of about 350 A. The low deposition temperature is a problem that can also easily be remedied.

The next step was to coat a 20 cm long section resulting in a 9-cm length that was measureable. The results, shown in Figure 28 (a), are measured in a 0.6 T field $B \parallel c$ at 75 K. This shows good homogeneity of the conductor and of the critical current. Figure 28 (b) shows the magnetic field dependence at 75 K of the central 5 cm section of this tape. This performance is roughly comparable to that of thin, single layer YBCO. Figure 28 (c) shows the final measurement on this conductor as the magnetic field was reduced to near zero field. The I_c was 335 A under this condition.

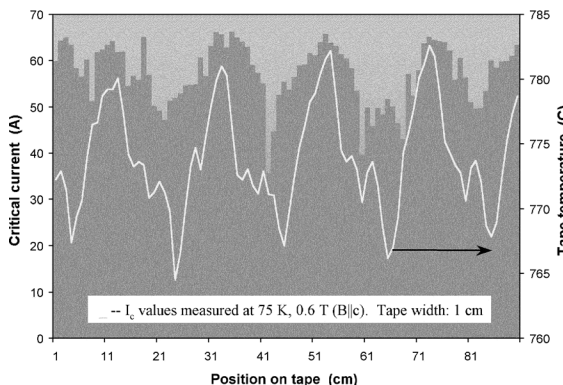
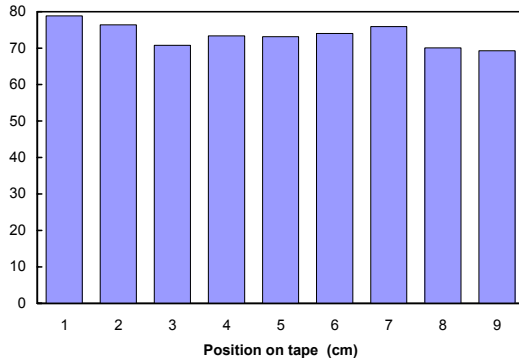
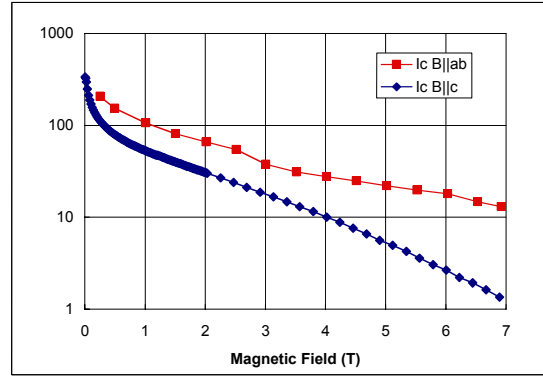


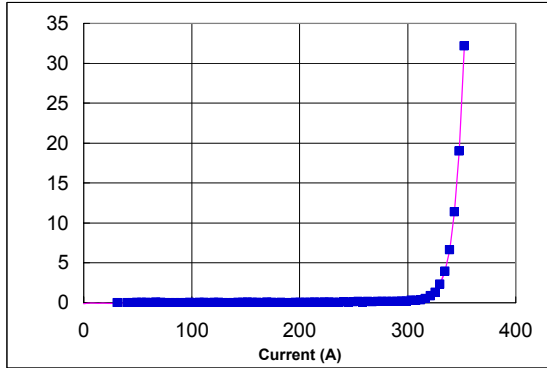
Figure 27. Variation in the critical current as a function of position. The periodic variations showed a good correlation with temperature during the deposition process, indicating a problem with the temperature control.



(a)



(b)



(c)

Figure 28. Measurement results on 20 cm Y/Sm-BCO multilayer tape at 75 K. (a) Critical current on central 9 cm section of tape in a 0.6 T $B || c$ magnetic field. (b) Magnetic field dependence of central 5 cm section of tape. (c) Critical current of 335 A measured in magnetic field of ~ 4 mT (40 Oe).

A section of this tape was patterned into bridges to obtain additional information about the conductor. It was determined that the superconductor thickness was $1.9 \mu\text{m}$, and that the estimated thickness of each YBCO layer was $0.9 \mu\text{m}$. The inductive T_c was 92.8 K. Two sections patterned into bridges 0.2 mm by 5 mm yielded J_c values 2.05 and 2.15 MA/cm^2 . These critical current density values and the sample geometry yield an extrapolate critical current of 400 A/cm-width .

To summarize this work, it has been determined that the use of YBCO/SmBCO multilayers can mitigate the degradation in film quality and performance present in single layer YBCO films greater than about $1.5 \mu\text{m}$. In the single layer films, it was found earlier that only the lowest $1.5 \mu\text{m}$ of the film carries any significant current. In thicker films, the upper part of the film is rough and poorly connected and makes only a small contribution to the current density. The use of SmBCO interlayers results in a kind of resetting of the YBCO growth morphology, which is not well understood, but that allows the growth of a much greater total thickness of superconductor with much higher critical currents possible. The performance of the Y/Sm-BCO multilayer structure performance can be improved by reducing the Sm layer thickness and by increasing the number of layers. Using a conservative multilayer design (Y-Sm-Y only), short, continuously processed tapes have been made with critical current greater than 335 A at 75 K and self field. The same multilayer design was extended to two one-meter lengths that had critical currents (same conditions) of 142 A and 189 A. The multilayer approach is a viable technique for greatly enhancing coated conductor performance and achieving critical currents greater than 200 A/cm-width .

2.1.3 Microstructural Development and Control in $\text{YBa}_2\text{Cu}_3\text{O}_y$ Coated Conductors (T.G. Holesinger, B.J. Gibbons, S.R. Foltyn, P.N. Arendt, J.R. Groves, and J.Y. Coulter)

Ion-beam-assisted deposition (IBAD) is an effective method for preparing a biaxially-aligned template on polycrystalline metal substrates for subsequent oriented growth of oxide buffer layers and superconductors. $\text{YBa}_2\text{Cu}_3\text{O}_y$ (Y-123) may be deposited directly onto the IBAD YSZ or MgO films. However, additional buffer layers such as CeO_2 , are necessary for optimizing the transport properties and controlling defects in the Y-123 films. The additional buffer layer(s) may provide a better lattice match to Y-123 or improve the chemical stability of the interface relative to the high reactivity of barium in Y-123.

Understanding the interactions between the Y-123 film, the underlying buffer layers, and the substrate is important for developing the IBAD process into a practical conductor technology. Each process used to deposit the bi-axially textured template, additional buffer layer(s), and the superconductor creates interfaces along which defects or interfacial reactions may result. These defects can be additive and propagate through the entire film structure to affect the growth and properties of the superconducting film. Defects within the films and at the interfaces can be structural, chemical, or a combination of both. Their origins include substrate roughness, lattice mismatch, porosity, and interfacial reactions. CeO_2 is a stable oxide with a good lattice match to Y-123 and it has been successfully used as a buffer layer. However, recent work has shown that even this highly stable material reacts with Y-123 along the interface and affects the superconductor's properties. Since it appears that nearly all materials react with Y-123 at typical processing temperatures, it is especially important to understand what general aspects of the interfacial reactions between a given material and Y-123 limit or enhance the rate of reaction and what effects they may have on the transport properties.

IBAD was used to produce the biaxially-textured YSZ film on Inconel 625 or Hastelloy substrates. The ceria and Y-123 layers were deposited by pulsed laser deposition (PLD). The IBAD YSZ thickness was kept at 0.5 μm while the thickness of the ceria and Y-123 layers were varied between 5 and 1000 nm and 1 and 3 μm , respectively.

Transmission and scanning electron microscopy (TEM and SEM) samples were prepared in the same manner for viewing in the longitudinal transverse direction (perpendicular to both the nominal c-axis of the film and direction of current flow). Phase identification was performed by x-ray diffraction, energy dispersive spectroscopy (EDS) and electron diffraction.

Substrate and buffer layer defects can influence the growth of the Y-123 film. It has been found that the growth of the Y-123 film changes to accommodate these defects. These changes may be reflected in a change in alignment, generation of a structural defect in the Y-123 film, or the occurrence of an interfacial reaction phase. The SEM micrograph of Figure 29a demonstrates how a substrate defect can propagate through the film and affect film growth. In this case, a large pore that spans the entire thickness of the film is formed. The sources of these substrate defects include surface roughness, cracks, pits or holes, bubble formation, and substrate inclusions. In general, no interfacial reactions are found between the IBAD YSZ and metal substrate. The layer that forms between them is the passivating Cr_2O_3 layer that normally forms on Ni-Cr alloys that are exposed to oxygen at elevated temperatures as occurs during Y-123 deposition.

The fine structure of these defects is shown in the TEM and selected area diffraction (SAD) micrographs of Figure 29b, c, and d. In Figure 29b, the local alignment of the IBAD YSZ layer changes such that an imprint of the substrate defect is transferred through the subsequent layers. The end result is an area of enhanced reactivity at the ceria / Y-123 interface. Inclusions and delaminations at the metal/buffer interface can lead to the microstructure shown in Figure 29c. The presence of the bubble before Y-123 deposition is indicated by the dense film and alignment of the Y-123 to accommodate the defect. The result, as indicated by the diffraction pattern in Figure 29d, is a series of relatively high-angle tilt boundaries in the Y-123 film.

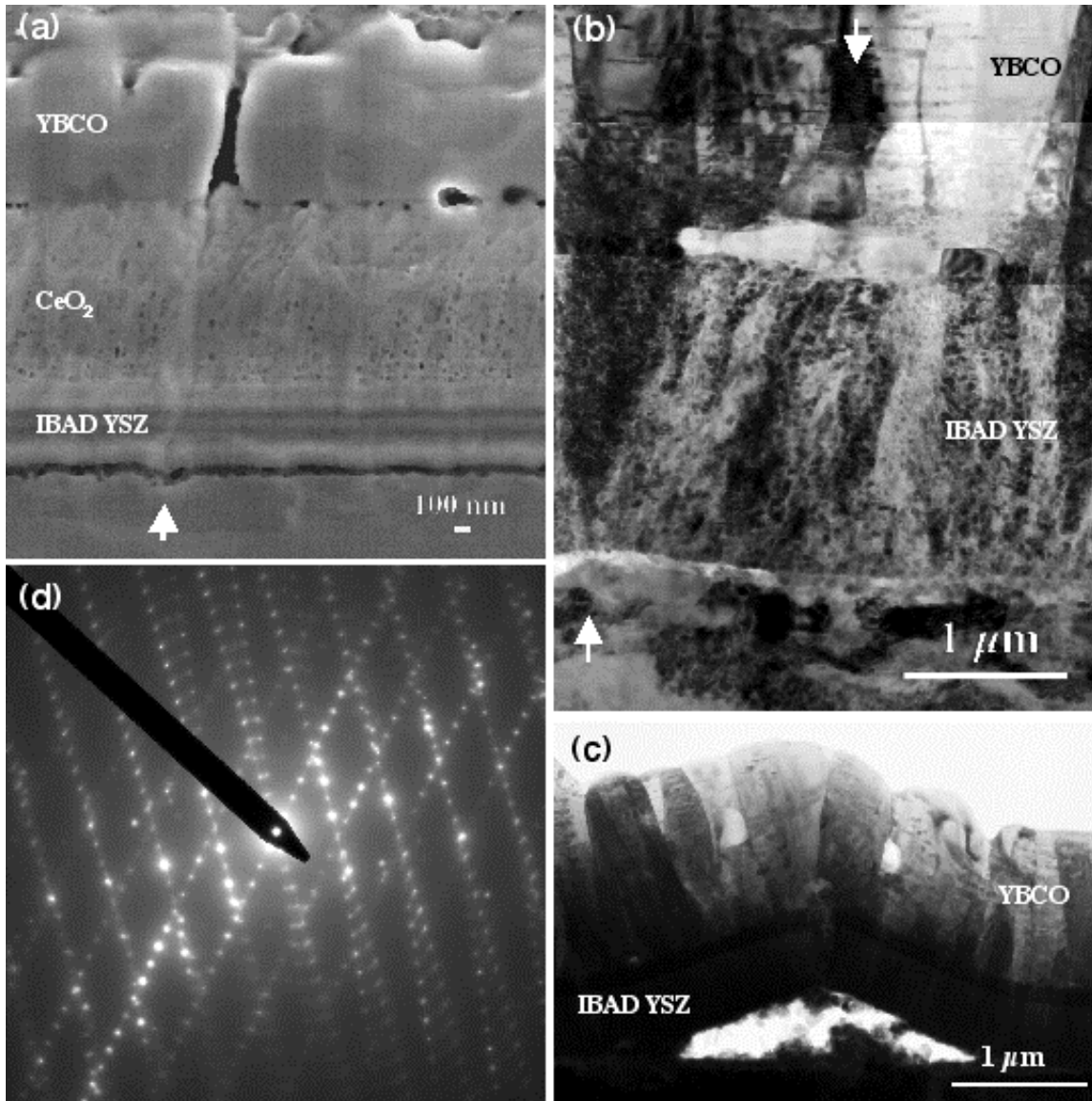


Figure 29. SEM, TEM, and SAD micrographs of types of substrate defects that thread through the buffer layers and affect Y-123 film growth.

The SEM micrograph (a) shows the structure of a defect that starts at a pit in the substrate and ends as a pore in the Y-123 film. The TEM micrograph (b) shows the effect of a small hillock on the substrate and the ensuing disruption and discontinuity in the IBAD YSZ. Such discontinuities enhance interfacial reactions between the Y-123 and ceria. The TEM and SAD micrographs, (b) and (c) show the result of bubble formation between the substrate and YSZ. The growth of the Y-123 film over this defect results in a series of tilt boundaries between the Y-123 grains as indicated by the SAD micrograph (d).

Little reaction occurs between the interior buffer layers. However, the morphology of the interfaces will follow the underlying substrate. Problems occur when cracks develop in the buffer layers and reach the Y-123 film. These defects greatly enhance interfacial reactions. Transport of material from the Y-123 film into the underlying buffer layers and substrate and vice-versa occurs as shown in Figure 30.

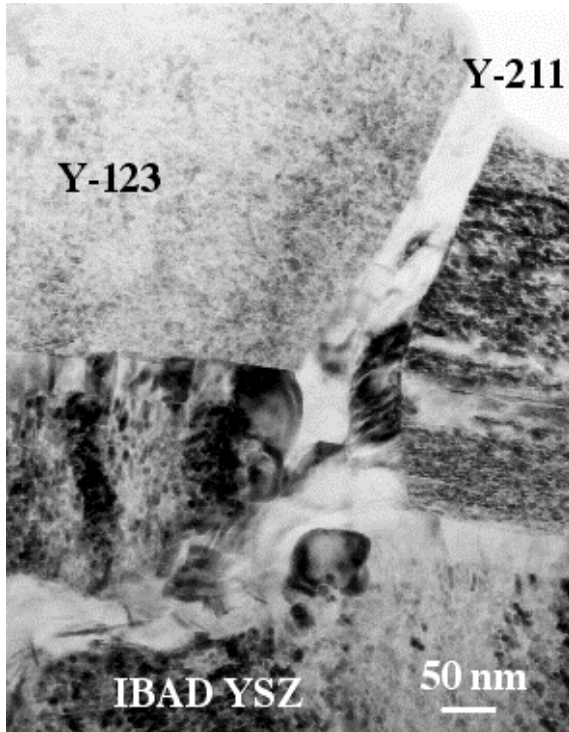


Figure 30. TEM micrograph of a crack structure in the IBAD YSZ layer and the resulting reaction between the Y-123 and buffer layers that results in the formation of an extended defect.

Misalignments in the Y-123 film of the coated conductor can take the form of a-axis, 45° in-plane rotated, and tilted grains. Examples are shown in Figure 31. a-axis oriented grains are often found in films deposited under non-optimal conditions. Grains rotated 45° in-plane have also been found in the Y-123 films as shown in Figure 31b. No specific causes for their appearance have yet been clearly identified. The last example is of grains that are tilted as shown in Figure 31c and d. These grains have an inverted, pyramidal shape. Once nucleated, these grains tend to grow faster than the matrix and often protrude above the nominal film surface. Randomly oriented interfacial reaction products are a cause for their nucleation in the film. The inverted pyramidal shape for the latter class of misoriented grains suggests a role as a potential current limiting defect having a thickness dependence.

The Y-123 film properties and interfacial reactions at the Y-123 / ceria interface can be controlled by a suitable choice for thickness of the underlying buffer material (ceria). Shown in Figure 32 is a plot of the critical current density (J_c) as a function ceria thickness for Y-123 films deposited on IBAD YSZ-coated metal substrates. This maximum in J_c correlates with a minimum in the reactivity between the ceria buffer layer and Y-123 film. The critical ceria layer thickness on the IBAD YSZ metal tapes was approximately 90 Å. The maximum J_c value reached with a 90 Å ceria film and a 1.5 μm Y-123 film was 1.7 MA/cm² at 75 K and self-field.

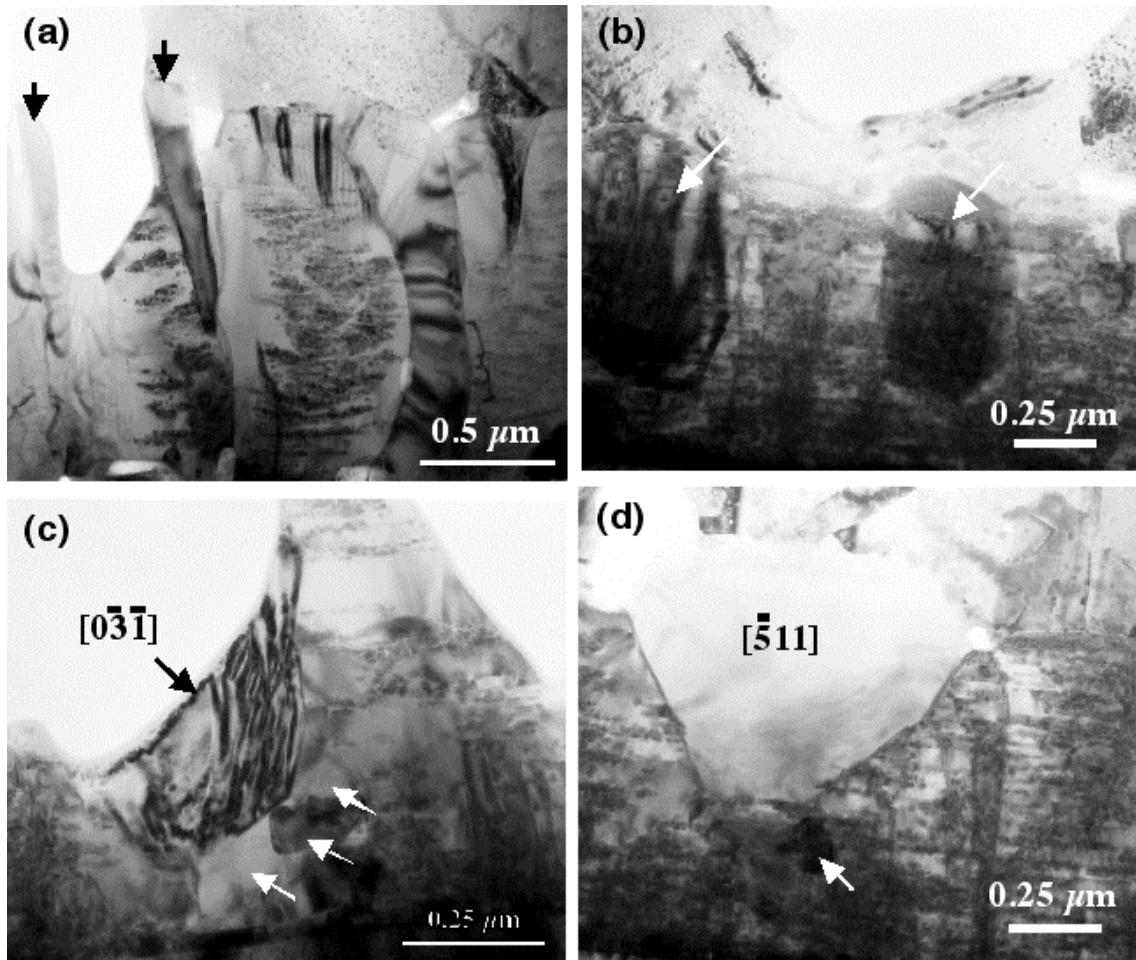


Figure 31. TEM micrographs of misoriented grains in the Y-123 films. Typical orientations are (a) a-axis, (b) 45° in-plane rotated, and (c) tilted Y-123 grains. The indicated orientations in (c) and (d) are approximately parallel to the $[110]$ direction in the film. The tilted grains are not coherent with the film matrix and appear to be randomly oriented around the $[001]$ direction.

At the critical thickness, the interfacial reactions were found to be almost non-existent as shown in Figure 33a. The few that were found could be traced to the propagation of non-uniformities in the substrate to the ceria/Y-123 interface as shown in Figure 34. J_c decreases and interfacial reactions increase as the ceria buffer layer thickness moves away from the optimal value. Figure 33b shows the interface in a film where the ceria thickness was initially 1000 Å. Large portions of the interface have reacted to form BaCeO_3 and YCuO_2 . The reactions between the ceria and Y-123 tend to stop when the underlying IBAD YSZ/ceria interface is reached. Conversely, the extension of the reaction products into the Y-123 increases without bound as the severity of the interfacial reactions increase. The reaction products also serve as nucleation sites for misaligned Y-123 grains as shown above. These results suggest that interfacial reactions play a significant role in forming current limiting defects in Y-123 films.

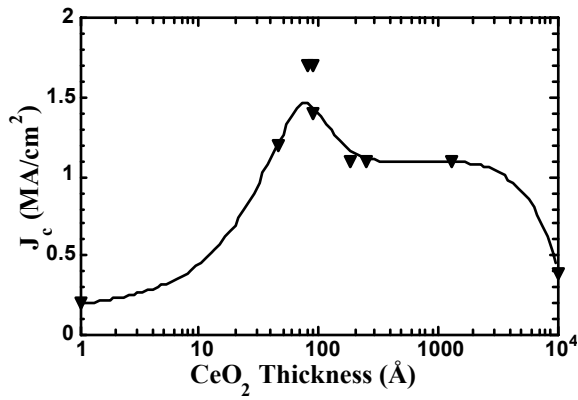


Figure 32. Plot of J_c versus the thickness of the ceria buffer layer next to the Y-123 film. The Y-123 films were approximately 1.5 μm thick and the critical thickness of the CeO_2 layer was ≈ 90 Å.

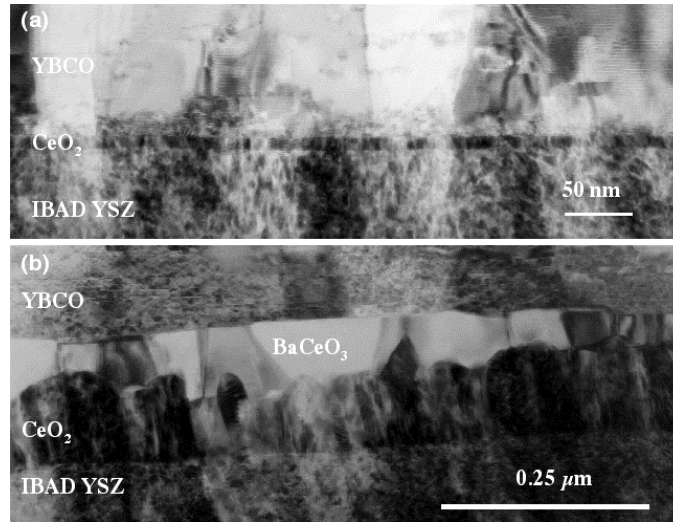


Figure 33. TEM micrographs of the Y-123 / ceria interfaces in films with nominal ceria thickness of (a) 90 Å and (b) 1300 Å. Whereas in (a) no interfacial reactions are found, a nearly continuous layer of BaCeO_3 is present in (b).

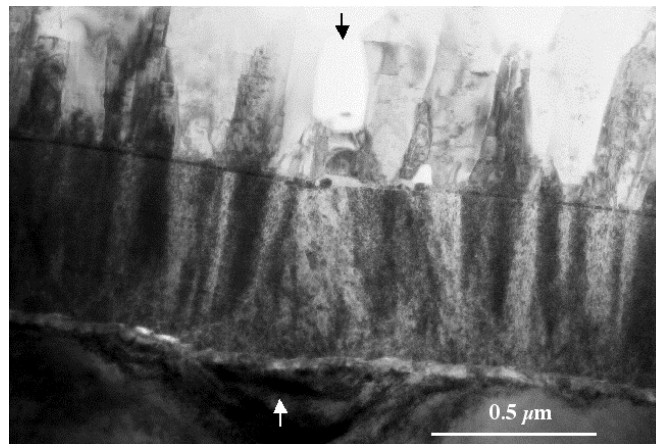


Figure 34. TEM micrograph of a Y-123 coated conductor. The ceria thickness was 90 Å, which minimized the interfacial reactions. The only interfacial reactions present in this sample were those caused by substrate defects that propagate through the buffer layers as shown above. The resulting discontinuity in

the substrate leads to an interfacial reaction at the Y-123 / ceria interface and a large pore in the Y-123 film.

Maximizing the J_c properties of the Y-123 coated conductors requires an understanding the origin of current limiting defects. A prime area for concern is the preparation of the substrate surface prior to film deposition. The results show that any defects in the substrate transfer through the buffer layers to adversely affect the growth of the Y-123 film due to changes in morphology or chemical reactivity. In addition to the role it plays for biaxial alignment, the IBAD YSZ layer is also a diffusion barrier. Defects such as cracks in the buffer layers defeat this purpose as they are chemically more reactive and allow transport of material from the film into the underlying buffers and substrate and vice-versa.

Misoriented grains within the film are also a concern for maximizing J_c . Their origins are varied and their presence can be used as guide to determining optimal deposition conditions or gauging the extent of interfacial reactions. The presence of the a-axis grains can be used to address the former point while a measure of the tilted Y-123 grains can be a gauge of the latter. Many of the tilted Y-123 grains could be traced to nucleation on a randomly oriented interfacial reaction phase such as CuO, YCuO₂, or BaCeO₃. Other deleterious effects of the reactions are intergrowths within the Y-123 gains. Hence, it is very advantageous that the interfacial reactions can be minimized through a suitable choice of the final buffer layer thickness. For the case of ceria on IBAD YSZ, the critical thickness was around 90 Å. The J_c value of 1.7 MA/cm² is one of the highest values measured for Y-123 films greater than 1 µm in thickness on polycrystalline metal substrates. Further increases in the J_c performance will come with the mitigation of substrate defects like the one shown in Figure 34.

The origin of some defect structures in Y-123 coated conductors based on the IBAD process was examined. The defects can be additive and propagate through the entire film structure to affect the growth, orientation, and properties of the superconducting film. The interfacial reactions and the transport properties of the Y-123 films can be controlled by a careful choice of the thickness of the underlying buffer layer. In the case of a ceria buffer layer, a critical thickness value of 90 Å was found for which the interfacial reactions were minimized. A record J_c value of 1.7 MA/cm² (self-field, 75 K) was obtained in a 1.5 µm thick Y-123 film on an IBAD YSZ / metal substrate with an intervening 90 Å ceria buffer layer. Further increases above this level of performance will come with the elimination of substrate-induced defects.

2.1.4 Correlation between Transport Current Profiles and Tape Microstructure in YBCO Coated Conductors

(F.M. Mueller, G.W. Brown, M.E. Hawley, D.J. Brown, J.Y. Coulter, M.P. Maley, B.J. Gibbons, E.J. Peterson, T.G. Holesinger, and S.R. Foltyn)

We have developed a magnetic imaging system that yields quantitative information about the magnetic field near the surface of a superconducting sample while it is carrying current at liquid nitrogen temperatures. We have numerically inverted the self magnetic field data from $\text{YBa}_2\text{Cu}_3\text{O}_{7-d}$ bridges and silver-coated $\text{YBa}_2\text{Cu}_3\text{O}_{7-x}$ tapes to derive the internal current densities. Preliminary results are consistent with the expected patterns but suggest that the current flow is often non-uniform.

High temperature superconductors (HTS) are of interest in electrical power applications where their unique properties can make them economical if they can be optimized and produced repeatably. One area of characterization interest is using magnetic imaging techniques to map current flow in HTS and correlate it with microstructure and other data. The Biot-Savart law is the basis of relating current to magnetic field so that one can be determined from the other. Determining all three components of the field can be difficult, but the inversion problem can be simplified to local relations for 2-dimensional conductors at low resolution ($>30\mu\text{m}^2$ pixel area). In this situation, the components of the current density, J_x and J_y , can be obtained from the z component of the magnetic field B alone.

We performed magnetic imaging by rastering a magnetoresistive (MR) sensor on the surface of a superconducting sample cooled in liquid nitrogen. The design is similar to that of others in that the mechanical scanner motion is transferred into the dewar via a rod pivoting at a fixed point. Figure 35a shows a schematic of the measurement system. The MR sensors are read heads used in magnetic hard disk storage devices and are obtained from a commercial manufacturer, Read-Rite Corporation. Similar sensors have been used for magnetic imaging previously. A close up view of the sensor head is shown in Figure 35b.

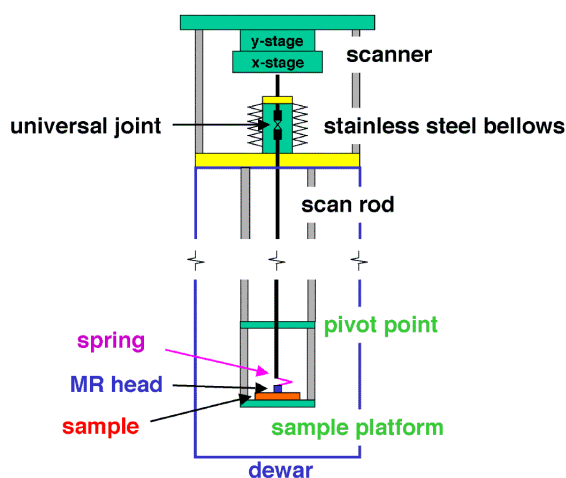


Figure 35a. Schematic of the scanning system with scanning stage at room temperature connected to a long rod and pivot point near the sample, which is at liquid nitrogen temperature.

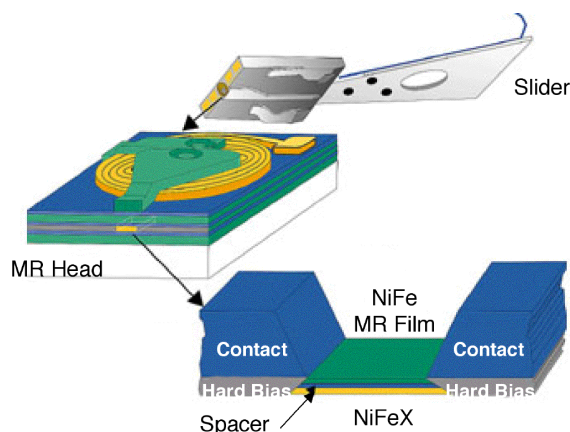
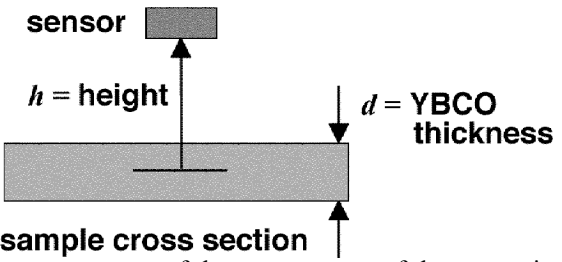


Figure 35b. Details of the MR sensor head construction. The sensor heads have an area of less than $1\mu\text{m}^2$ and a sensitivity of greater than $3\mu\text{V/G}$.

$$B_z(y) = \frac{\mu_o}{4\pi} \int dz' \int \frac{J_x(y) \cdot (y - y')}{|\vec{r} - \vec{r}'|^3} dy'$$

$$B_z(k) = \frac{i\mu_o}{k} \sinh\left(\frac{d}{2}|k|\right) \exp(-h|k|) J_x(k)$$


The diagram illustrates the experimental setup. A rectangular sensor is positioned at a height h above a sample cross section. The sample has a thickness d , which is the YBCO thickness. The sample cross section is shown as a gray rectangle. The sensor is shown as a smaller gray rectangle above it. Arrows indicate the height h and the thickness d .

Figure 36. Biot-Savart equations for the real and k-space components of the z component of the magnetic field calculated from a given current distribution. The experimental geometry is shown on the right.

The sensors are employed in constant current mode and the voltage on the head is proportional to the resistance change. This provides B_z maps, and current maps are calculated by inverting the integral equations shown in Figure 36. For simplicity, we present data here as maps of $J = \sqrt{J_x^2 + J_y^2}$.

We examined two different samples. The first was an $\text{YBa}_2\text{Cu}_3\text{O}_{7-\delta}$ (YBCO) bridge with dimensions $6 \mu\text{m} \times 185 \mu\text{m} \times 5 \text{mm}$. Deposition was carried out by pulsed laser deposition (PLD) at 775°C on SrTiO_3 . The sample's critical current was $\sim 2.5 \text{ A}$. The second sample was a tape, consisting of PLD-deposited YBCO on a 1-cm wide Inconel ribbon and coated with 1 to $2 \mu\text{m}$ of silver. This tape was an early sample with a critical current of 10 A. Tapes produced today have $\sim 100 \text{ A}$ critical currents, implying that the sample under study likely has some defects. During scanning, a thin plastic layer (25 to $60 \mu\text{m}$) is used to protect the sample surface.

Current maps from the YBCO bridge are shown in Figure 37. Darker pixels represent larger currents. The current maps are $\sim 2 \text{ mm}$ square at 62×62 point resolution. Several obvious features are visible including repeatable variations along the edge of the bridge, an overall increase in signal magnitude as the current is increased, and an interesting behavior in the bottom quarter of the image. Here, as the current is increased, the path changes and narrows slightly.

Current maps from the HTS tape are shown in Figure 38. These scans are $\sim 9.2 \text{ mm}$ square with 62×62 point resolution. Here, current appears to be concentrated along the right side of the tape and in the vicinity of the defect near the bottom center. We see approximately the same current paths for both signs of current and we also see a general narrowing or sharpening of the current paths at higher magnitudes with some change in the pathways, particularly through the central defect, indicating its weak-link behavior.

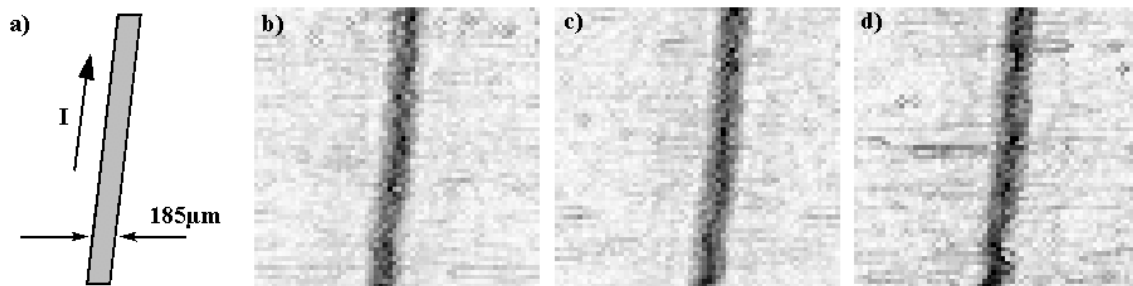


Figure 37. Panel a) is a schematic showing the HTS bridge and current flow. Panels b) through d) are current maps acquired from the same area of the sample at 1.5, 1.75, and 2.0 A, respectively.

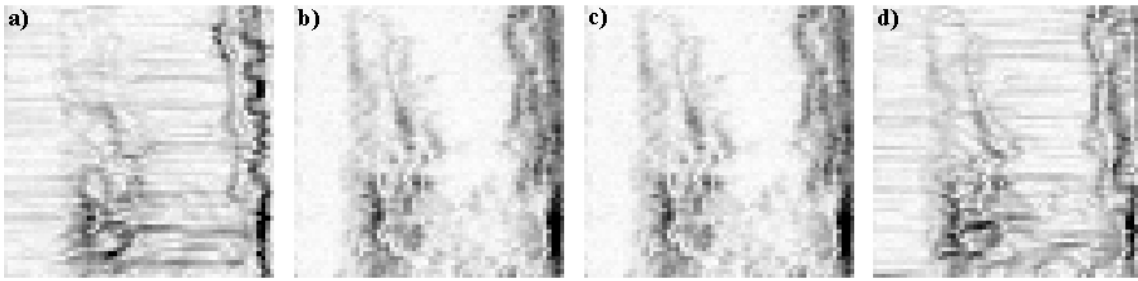


Figure 38. Current maps from the HTS tape. Panels a) through d) were taken with 5, 2.5, -2.5, and -5 A flowing respectively. Current flow direction is top to bottom. Imaged areas are ~ 9.2 mm x 9.2 mm.

The data presented here show the possibility of magnetic field imaging of HTS samples using an MR based scanner. Benefits of using MR heads include commercially available sensors that are economical and linear. The currents that we obtain from the magnetic field images show the expected behavior with interesting features due to the YBCO edge roughness, quality, and/or defects. A possible trend that should be further examined is the narrowing or sharpening of some current pathways as the tape current is increased.

The system was also used to characterize a high critical current YBCO tape that had some low I_c regions. The YBCO was deposited by pulsed laser deposition (PLD) on a 1-cm wide Inconel substrate with a buffered YSZ template layer produced by ion beam assisted deposition (IBAD). The YBCO layer was about 1.5- μ m thick and had a maximum I_c and J_c of ~ 250 A and 1.65 MA/cm², respectively, at 75 K and self field. We examined two regions, one with a very high I_c and the other with the lowest I_c of the meter long sample.

The results of the magnetic field scan of the high- I_c region are shown in Figure 39a. In this high conductivity region, the current is found to be uniform over the ~ 3.5 cm length of this scan. The white regions at the tape edges indicate areas of high magnetic field. The interior region of the tape has a lower, and very small, current density. In contrast, the region with low I_c shows a large variation in the current map across and along the scan area, as shown in Figure 39b. At the two ends of the scan, where the current density is relatively high, the magnetic field penetrates only slightly into the tape from the sides. However, in the middle of the scan, where the I_c is lowest, it can be seen that the magnetic field penetrates well into the tape, indicating that less than half of the tape width is a good superconductor. At the right side of Figure 39b is a map showing the direction of the local current. In the bulk of the sample, the current flow can be seen to be laminar along the tape length; however, in the “defect” region where the field penetrates deeply, the direction is seen to be much less well defined, indicating likely both the lower magnitude of the current density and the varying direction in that region.

We then examined the current distribution in the “defect” region as a function of the transport current amplitude. Figure 40 shows the results of mapping the current density in the defect region at several different levels of transport current. Figure 40a shows the two current density maps graphically, and Figure 40b shows an x-y plot of the current density along a line across the tape. It can be seen that as the transport current is increased, the region carrying the current becomes progressively narrower. This fact illustrates that the left side of the current-carrying region is still somewhat weak.

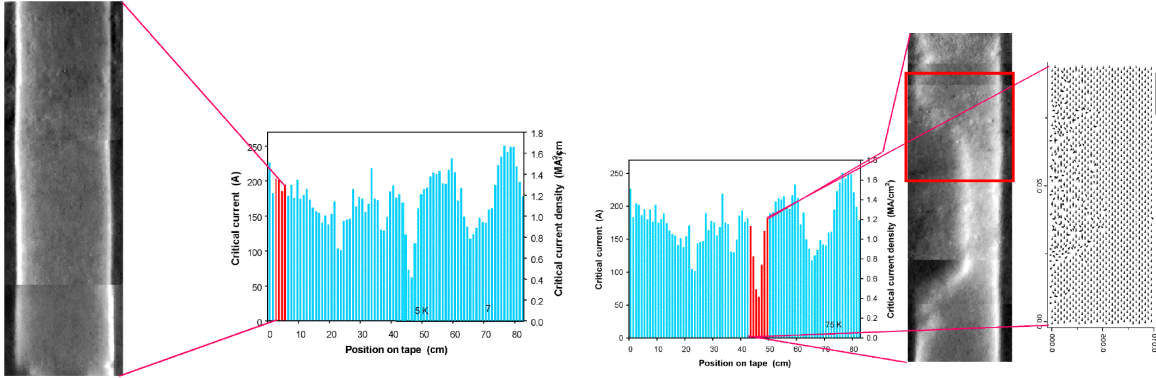


Figure 39a. Current density is uniform over a high critical current I_c (185 A) region of the tape. The YBCO is deposited by PLD on a 1-cm wide Inconel substrate with an IBAD YSZ template layer.

Figure 39b. Current density shows the nonuniformity of the current flow in a low I_c (57 A) region of the same tape shown in 39a. The image on the right shows a vector current density map of the sample.

The low critical current behavior observed by the magnetic scanning technique can be correlated with x-ray diffraction (XRD) analysis of the YBCO crystallographic orientation. Figure 41 shows several x-ray diffraction maps of the tape studied here for the peak intensity distribution of typical YBCO orientations. The data shown in Figure 41 were taken on a Bruker D8 Discover XRD apparatus fitted with a large area, two-dimensional position sensitive detector and the Bruker GADDS software to allow rapid acquisition of spatially dependent orientation information with resolution down to 10 μm . The data in Figure 41 show that the region with high critical current has a high degree of c-axis orientation, whereas the low I_c region has a large amount of a-axis oriented material. Typically, a-axis oriented grains are known to result in low critical current density, and this is true in this example also.

Next, the YBCO (004)/(005) x-ray peak intensity ratio was measured. This did show a correlation with the current density. Figure 42 shows that correlation on the left. On the right is a bar graph showing this intensity ratio along the line indicated by the arrow across the tape width. This bar graph also shows in red the intensity ratios at the YBCO deposition temperatures of 600°C and 750°C. The measured intensity ratio variation across the tape suggests that the temperature across the tape may have varied during deposition of the YBCO.

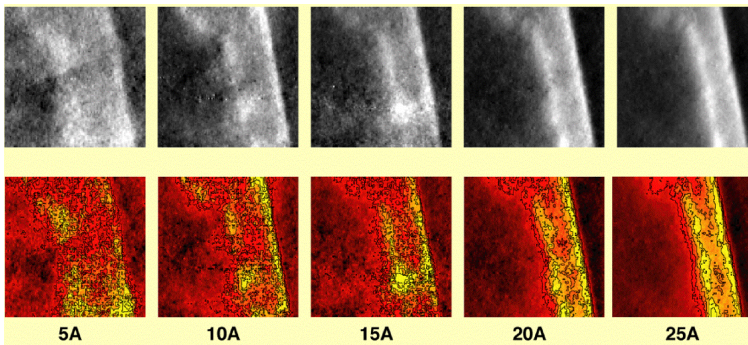


Figure 40a. Variation of the current density in the defect region of the conductor shown in Figure 3b with the transport current as a parameter. The top of the figure shows the density profiles in gray scale, and the bottom using a false color scale.

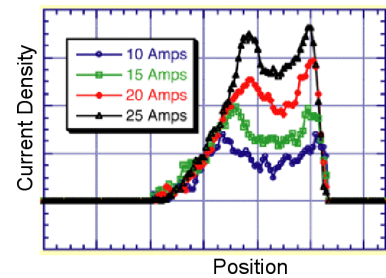


Figure 40b. Current density across the defected region of the tape as a function of position with the transport current as a parameter.

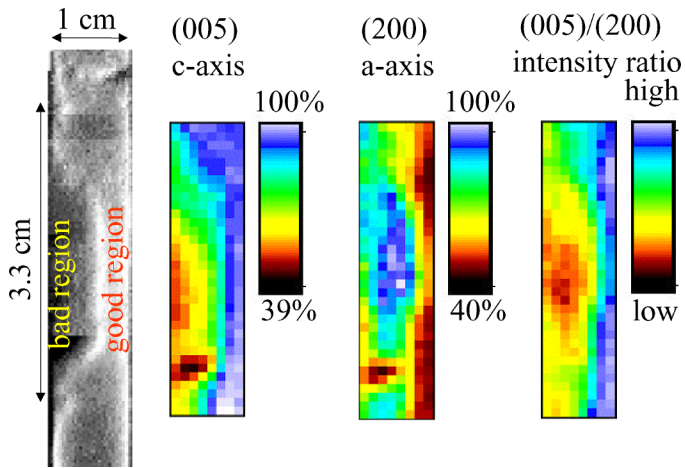


Figure 41. Left, current density map of low current region in tape. Right, x-ray peak intensity distributions for common YBCO orientations.

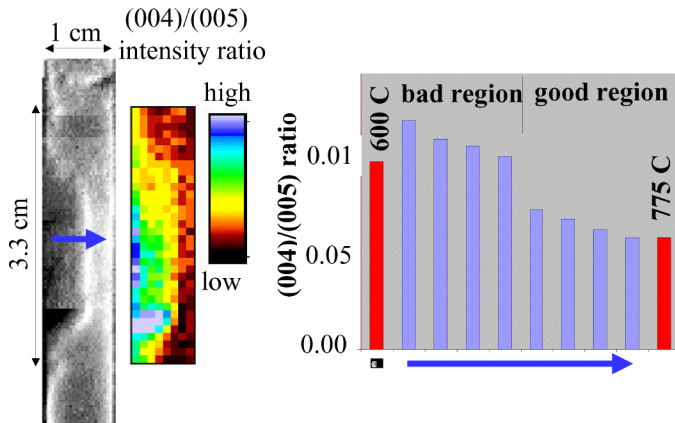


Figure 42. YBCO x-ray peak intensity ratios, known from the literature to correlate with deposition temperature, suggest that the deposition temperature varies across the tape width.

The texture of the YBCO was also found to vary across the tape width. Pole figure taken at two locations on the tape are shown in Figure 43. There is clear evidence of both c-axis and a-axis oriented grains, often indicative of a low YBCO deposition temperature in the bad region, while the good region only shows c-axis orientation. Figure 44 shows that the phi angle FWHM does not vary across the tape, but the fraction of a-axis oriented grains does.

The microstructure also is consistent with this conclusion. Figure 45 shows SEM images of both the bad and the good region. The bad region (left) shows a smooth surface and the presence of some a-axis oriented grains, consistent with a low deposition temperature.

TEM measurements on the same YBCO tape also found substantial differences between the two regions. Figure 46 shows that the good region is dense, well aligned, and has few secondary phases, whereas the low J_c region shows porosity, a-axis oriented grains, and second phases. Differences in the two areas are also apparent in the plan view TEM images shown in Figure 47.

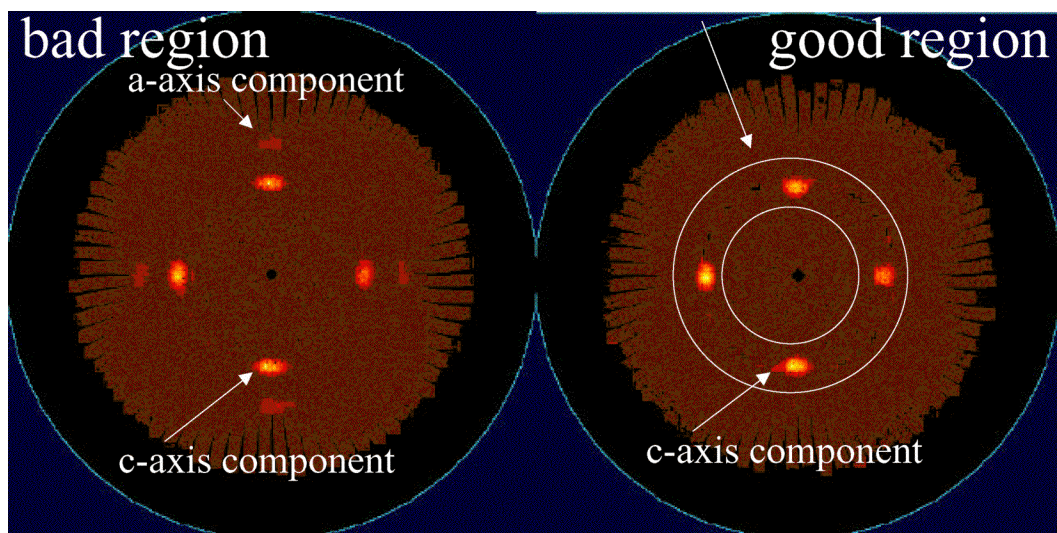


Figure 43. (104) Pole figures show both c- and a-axis-oriented components of YBCO in the bad region. The good region only shows c-axis oriented grains. The c- and a-axis orientation intensities are obtained by 360° integration in χ .

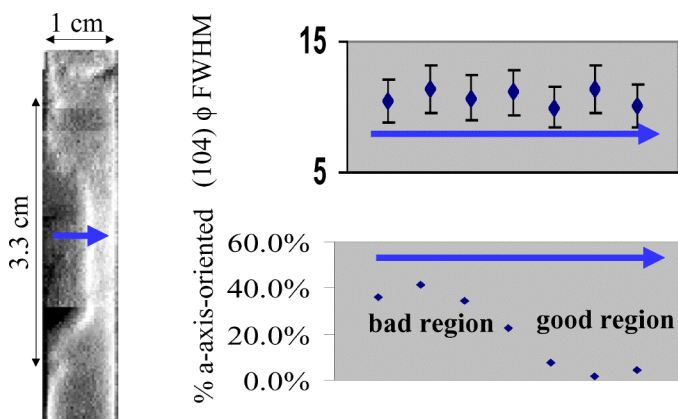


Figure 44. Phi angle FWHM does not vary across the tape, indicating that the poor performance is not caused by poor in-plane texture. However, the percentage of a-axis oriented grains is much higher in the bad region than in the good region.

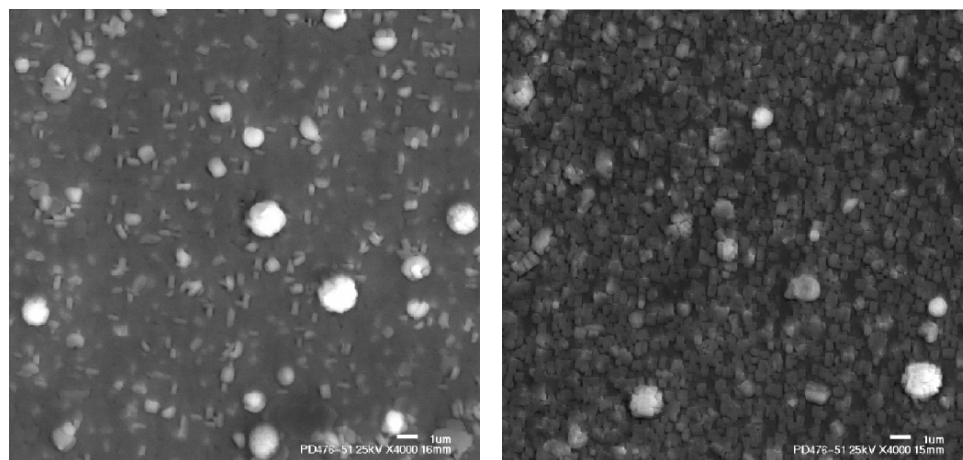


Figure 45. SEM micrograph of the bad region (left) and the good region (right). The microstructure is consistent with lower temperature deposition in the bad region. Each image is about 20 μ m on a side..

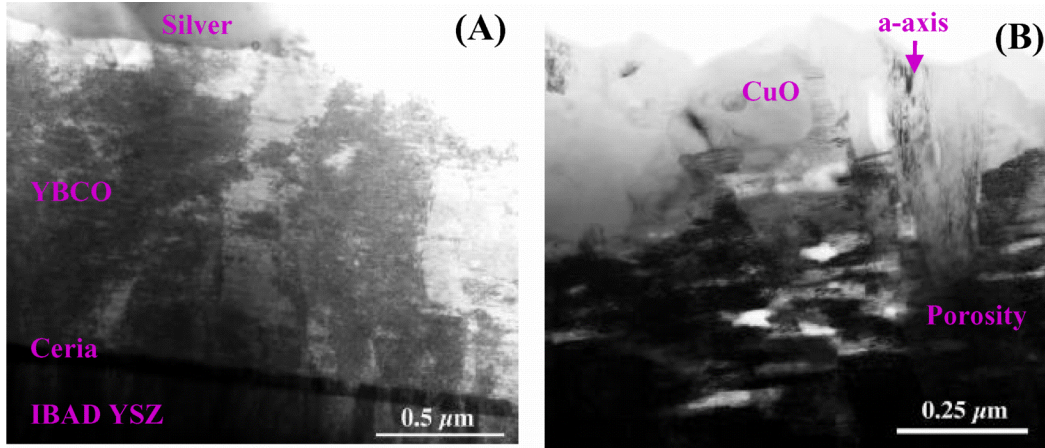


Figure 46. TEM images of the YBCO film. (A) - Dense, well-aligned film in the “good” section of the YBCO film. (B) - Significant amounts of porosity, a-axis YBCO, and secondary phases in the “poor J_c ” film section.

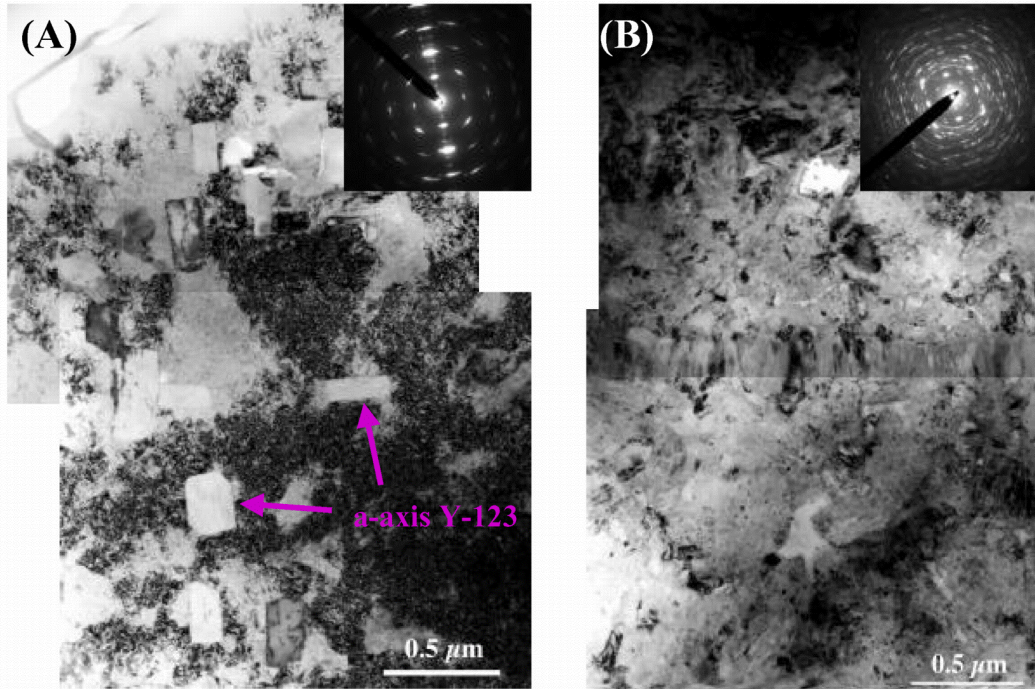


Figure 47. Plan view TEM images of regions from (A) the bad section of the film, showing the presence of a-axis oriented grains; and (B) the good section, showing much cleaner microstructure.

In conclusion, a system has been developed to image transport current profiles in YBCO coated conductor tapes and thin films using magnetoresistive sensors to image at a resolution of 10 μm. Two different regions of an IBAD YSZ – YBCO coated conductor tape have been probed: A high current region where $I_c = 185$ A, and a low current region where $I_c = 54$ A. The high current region shows a typical Bean critical state magnetic field profile across the entire tape width, whereas the low current region shows turbulent current flow with a concentration of current on one side of the tape. The high correlation between the magnetic imaging and x-ray, SEM, and TEM data suggests a single likely cause for the poor performance region: that of a low deposition temperature for the YBCO. This represents the first success in which magnetic imaging has helped to suggest an improvement in tape processing.

2.1.5 Accelerated Coated Conductor Initiative

(V. Matias, B.J. Gibbons, L.E. Bronisz, P.N. Arendt, S.R. Foltyn, E.J. Peterson, J.R. Groves, P.C. Dowden, J.Y. Coulter, R.F. DePaula, L. Stan, Q.X. Jia, J.O. Willis, A.T. Findikoglu, S.P. Ashworth)

The initial impetus for the Accelerated Coated Conductor Initiative (ACCI) was the realization that recently both Japan and Europe have been making great strides forward in Coated Conductor (CC) development with help of greater government funding, and that the US had been losing the lead. To this end, the US DOE provided additional funding to accelerate CC research and development beginning in FY2001 with facilities at both Oak Ridge National Laboratory and here at Los Alamos.

The STC's Los Alamos Research Park laboratories will be a national facility intended to demonstrate feasibility of continuous fabrication of high-quality HTS coated conductor (CC) tape using technologies already proven to produce smaller batch samples. This effort will provide an opportunity for accelerated development of 2nd generation HTS wire and its applications. The specific goals are to produce superconducting tapes of 10 m lengths, carrying over 100 A at 75 K, and to demonstrate their use in prototype applications. LANL staff, in collaboration with external partners, will do the work in this facility.

The Research park facility is a 10,000 sq ft area divided into 7 labs, 14 offices, and a reception area. The offices are for LANL staff as well as outside collaborators. It is anticipated that 8-10 people will be full time at the Research Park, in addition to the people who will spend part of their time at the Research Park. Figure 48 shows an exterior view of the Research Park building. Figure 49 shows views of a laboratory and an office in the Research Park. Figure 50 shows a schematic layout of the labs in this building.

When the facility is fully operational by summer/fall of 2002, the dual activities of CC fabrication development and applications research will have internal as well as external components. Foremost, it is to be a leading CC research facility. STC's Research Park Labs will be performing research and development work that moves the superconducting community towards manufacturing of CC tape. As a national center it will also facilitate collaboration and coordinate research among universities, national labs, and companies. In addition, by providing a collection of state-of-the-art equipment for CC development and making it available to outside users, this will also be a unique national user facility. It will be the first and most complete open facility to encompass a whole line of activities from CC fabrication to characterization and applications development.



Figure 48. View of Los Alamos Research Park building located across the street from the LANL Administration Building.



Figure 49a. View of an Applications Laboratory at the Research Park.

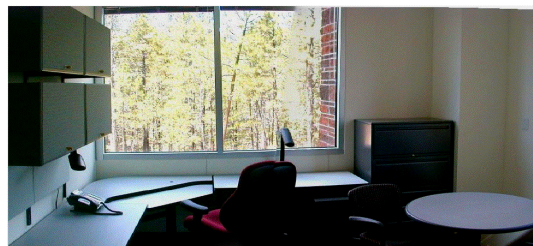


Figure 49b. View of office at Los Alamos Research Park.

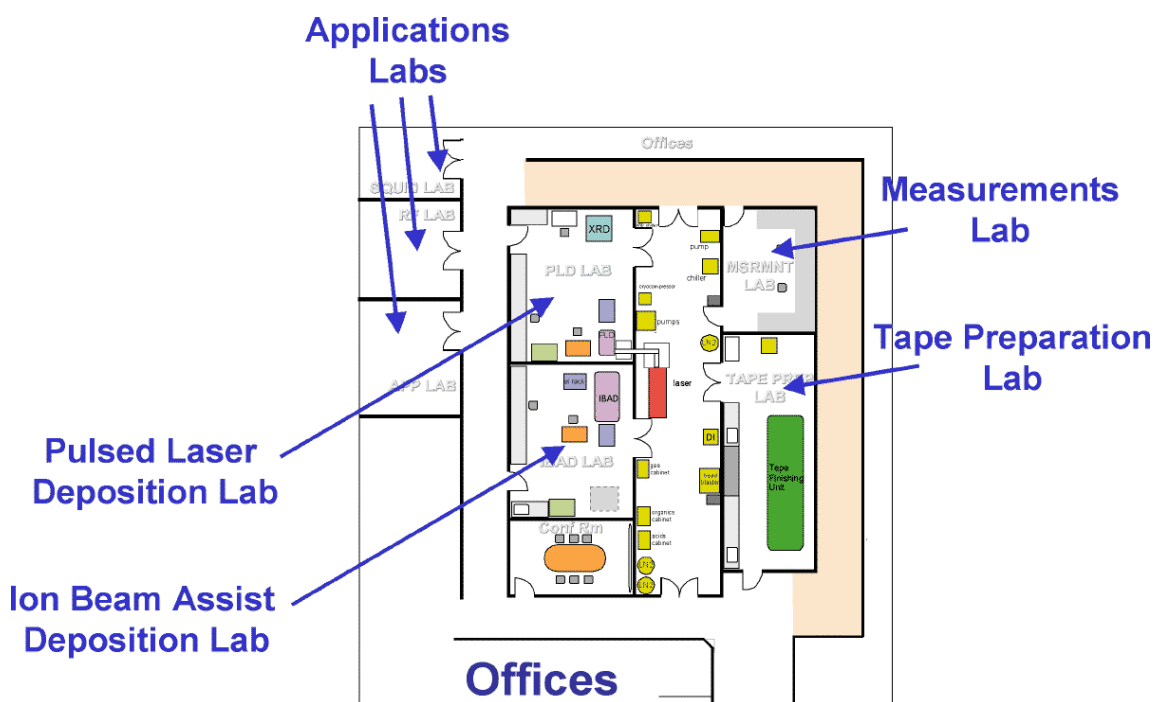


Figure 50. Schematic layout of the Research Park laboratories and offices.

In successfully accomplishing these goals, the STC will contribute significantly to the development of a novel technology and transfer it to American industry. New applications of this technology will surely spin out of these developments. At the same time, by making the Research Park a dynamic and leading research environment we will be able to attract the best young people and train them to work in this new technology area.

Currently the STC is making CC tapes in lengths of up to 1 m. The current processes for making a CC tape are: 1) mechanical polishing of a nickel-based alloy tape; 2) ion-beam assisted deposition (IBAD) of biaxially-textured template layers on the nickel-alloy tape; 3) pulsed-laser deposition (PLD) of HTS layers, in this case $\text{YBa}_2\text{Cu}_3\text{O}_7$, on top of

textured templates; and 4) overcoating with a silver layer. Except for step No. 1, all the processes involved are physical vapor deposition (PVD). A schematic of the stacking sequence is shown in Figure 51.

The research to be conducted at the new facility will address issues in transferring these processes to continuous superconductor fabrication. As an example, by making continuous lengths the processes will be ported to reel-to-reel tape drives. Such tape transport mechanisms will be developed and issues with continuous CC handling and processing will be explored. Eventually, the goal is to have all the PVD processes done in one vacuum-processing chamber. Initially, however, the template layer deposition by IBAD techniques, and PLD of YBCO will be performed in two separate chambers. In the future alternate deposition processes that are more oriented towards eventual manufacturing may also be employed. Processing of CC tape will also need to be accelerated. Faster processes will enhance research capabilities by being able to try out a many processing conditions in one run. Such work is also known as combinatorial research. New characterization techniques for quality control as well as diagnostic studies of long lengths of materials will be developed. Continuous tape measurements of surface roughness, crystallographic texture, and superconducting critical currents in magnetic field will be developed and employed.

By working on long continuous lengths of tape for both fabrication and measurements, materials and process development can be accelerated significantly since many experiments can be carried out in parallel, or combinatorially (see Figure 52). As an example the deposition temperature can be varied over 10 cm lengths and then the tape can be analyzed later to find the optimum process temperatures. Other parameters can also easily be varied during a run. Vast amounts of information can be obtained in single tape runs, typically 10 m long. Although this represents a new and more complicated mode of doing research it is clearly a way by which most research will be carried out in the future. In order to implement this properly new resources for data handling and analysis will also need to be explored. All of these new capabilities and the vigorous research programs that we plan to undertake will make STC's Research Park a premier and unique center for CC development.

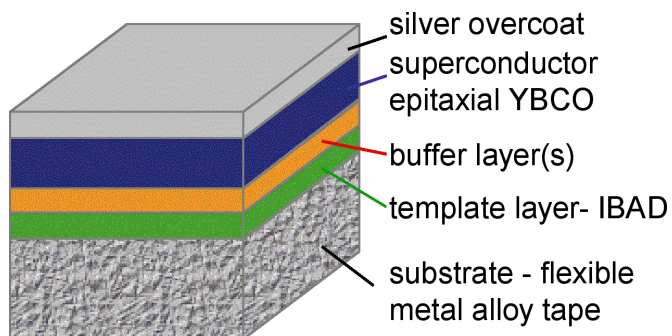


Figure 51. Stacking sequence of layers in the LANL process for coated conductor fabrication.

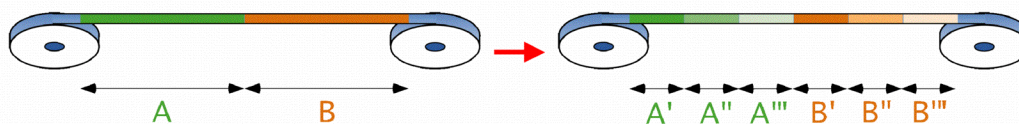


Figure 52. Schematic of combinatorial method for coated conductor experiments. On the left, for instance, IBAD MgO is deposited under two conditions, A and B. On the right, three conditions (‘, ‘’, and ‘’’) are used to deposit PLD YBCO, resulting in a total of six combinations to be tested.

Coated conductors require prepared metal tapes with smooth surfaces to achieve good in-plane texture in the IBAD MgO template layer. A new piece of industrial-type equipment has been ordered, Figure 53, to process reels of metal tape using wet electrochemistry (e.g., etching, electropolishing, electroplating). This system will have several stages that can be configured flexibly to achieve the required surface finish.

The metal tapes must of course also be characterized for surface roughness, before and after polishing. One tool for this is a laser scatterometer, which can be used in-line for instantaneous determination of surface roughness. This system is illustrated in Figure 54.

Production of the template layer is produced by ion beam assisted deposition (IBAD) of MgO. A schematic of the proposed IBAD chamber for the Research Park is shown in Figure 8. This chamber has reel-to-reel capacity to process 10 to 100 m lengths of tape. The right side of the chamber is the IBAD station including three electron beam guns and ion assist guns for deposition of the MgO template layer. The left side contains a buffer station for buffer layer deposition by e-beam evaporation and a PLD station for deposition of buffers of YBCO on the upper left to achieve complete process integration. The initial configuration will include the IBAD system and the e-beam evaporators.

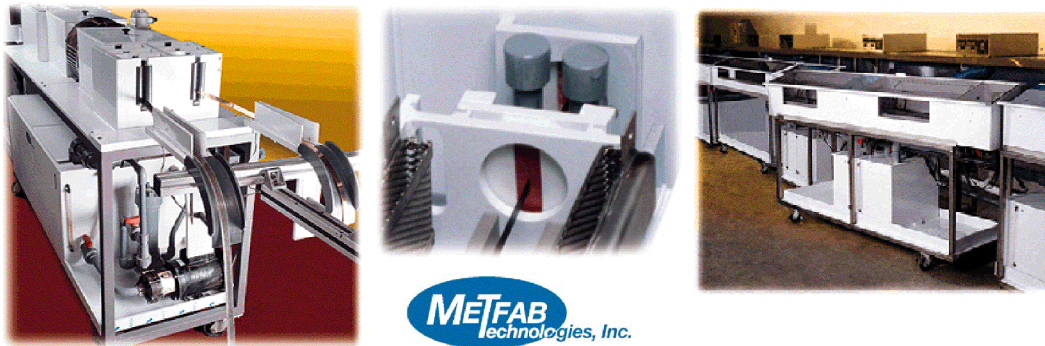


Figure 53. Illustration of tape polishing equipment ordered for the Research Park.

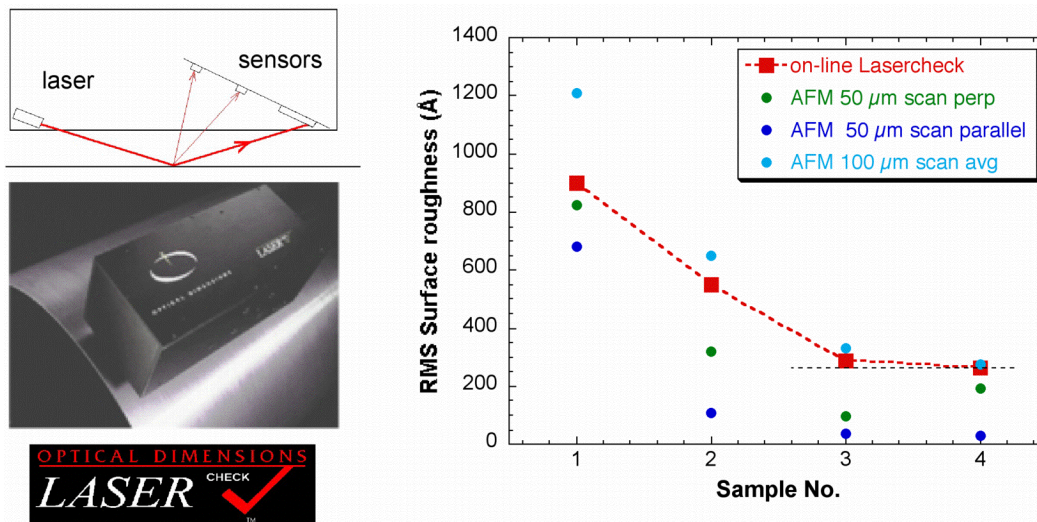


Figure 54. Schematic of laser scatterometer configuration and comparison of on line laser data with atomic force microscope (AFM) off-line scans.

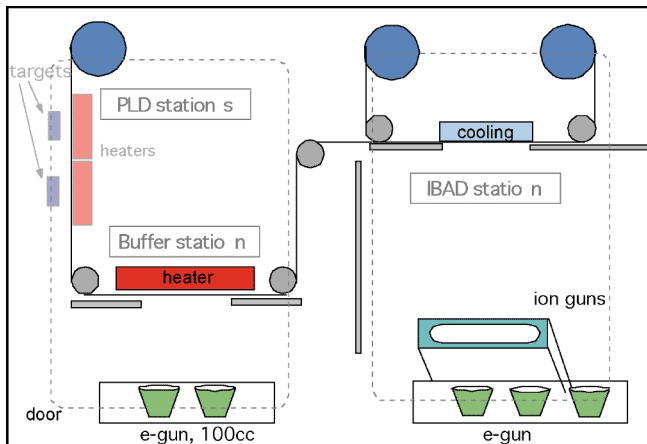


Figure 55. Schematic of proposed IBAD chamber.

In addition to the deposition equipment shown in Figure 55, the IBAD chamber will also include *in-situ* monitoring and diagnostic equipment. One of the most important of these is Reflection High Energy Electron Diffraction (RHEED). It can provide information of the structure of the film during growth, on texture development, on the optimum MgO film thickness, on out-of-plane tilt of the film, and on grain size. Figure 56 shows that the use of RHEED to monitor the growth of the MgO film in real time has proved extremely useful to maximize the in-plane texture.

For the chamber in the Research Park it is necessary to introduce a novel implementation of RHEED: that of scanning RHEED in both time and space, to monitor the deposition of MgO on the moving tape. By scanning the RHEED beam at the speed of the moving tape, it is possible to obtain RHEED images at a single location on the tape at different stages of deposition. This technique is shown schematically in Figure 57.

A second technique being considered for *in-situ* monitoring is that of ion scattering, illustrated in Figure 58. This is the most surface sensitive analytical tool available, and its real power is obtained when it is used *in-situ* on surfaces that have not been contaminated by the ambient atmosphere. The use of time of flight ion and recoil scattering (TOF-ISARS) is useful for determining the top most layer and layer structure, the presence of residues and contamination, whether there is complete coverage of a surface, and diffusion of elements through layers.

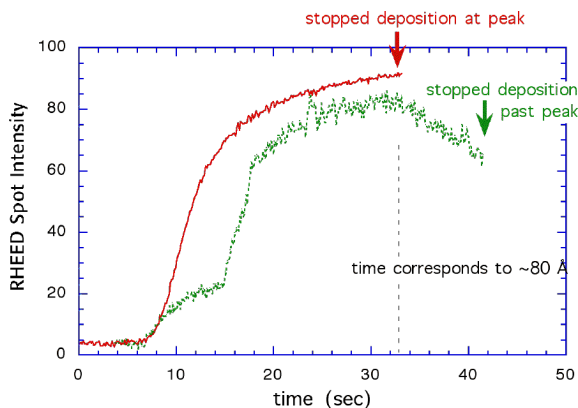


Figure 56. RHEED spot intensity for MgO film deposition stopped at the maximum and past the peak position. The best in-plane texture coincides with the peak spot intensity.

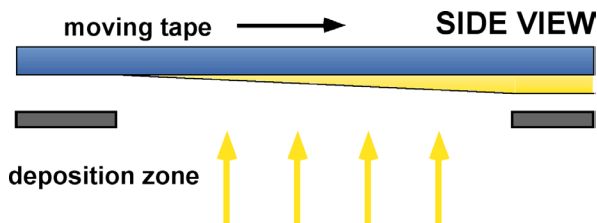


Figure 57a. RHEED beam is scanned from left to right at speed of the tape.

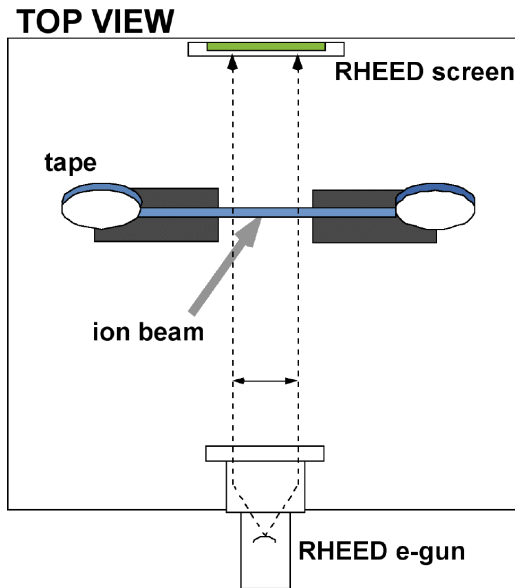


Figure 57b. Top view of the RHEED system showing the RHEED gun, the tape, and the RHEED screen. The RHEED beam intersects the tape at glancing incidence.

A third technique of atomic absorption (AA) monitoring may also be used for real time, in process monitoring of deposition rates. It can be used to independently monitor and control the deposition rate from one or more electron beam evaporators, e.g., to accurately control the stoichiometry of the deposited film.

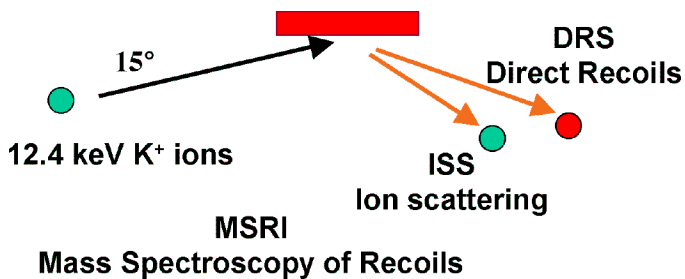
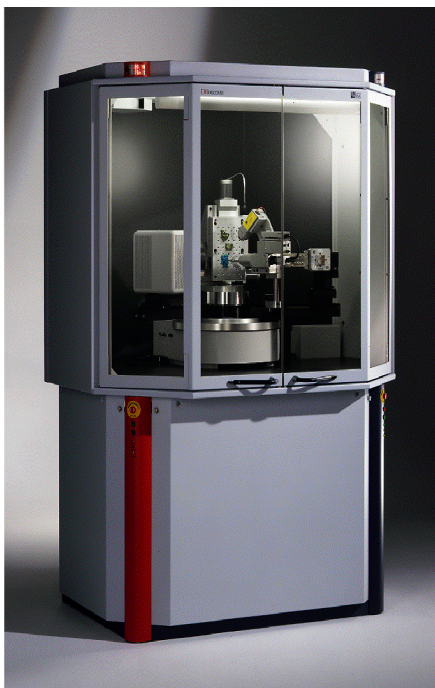
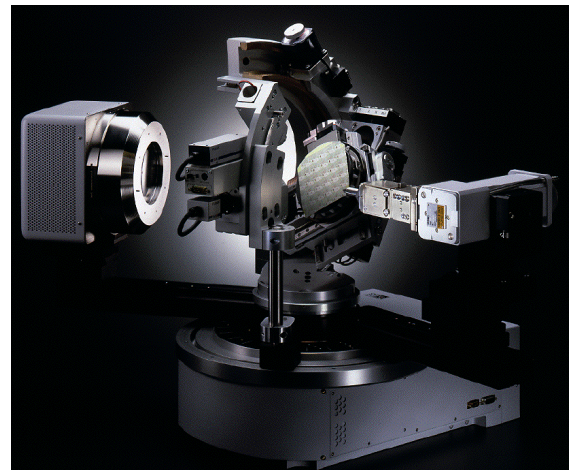


Figure 58. Schematic of ion scattering from a surface for *in-situ* monitoring.

A Bruker D8 Discover x-ray diffraction apparatus (Figure 60) will be used to characterize the coated conductor at various stages of processing. It is fitted with a 2D position sensitive detector and uses the General Area Diffraction Detector System (GADDS) to achieve rapid data acquisition and analysis. For instance, it can perform pole figures very rapidly making use of the large area detector. This can be used to analyze the texture of the IBAD MgO template layer, of the buffer layers, or of the YBCO film. Figure 61 shows the location of a 500- μm diameter beam on a YBCO tape used to perform a pole figure in 10 minutes. Another more standard diffraction mode, it can analyze the quality of the YBCO film, e.g., fraction of c-axis or a-axis oriented grains. It also has an x,y stage with a minimum spot size of 10 μm . It can be retrofitted with reel to reel capability to analyze long lengths of tape.



a



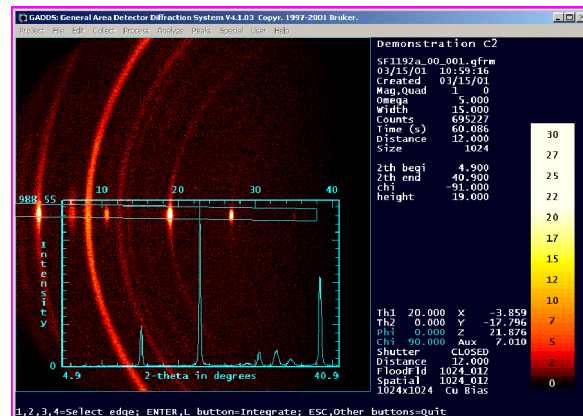
b

Figure 60. Bruker D8 Discover x-ray diffraction system.

a. Measurement unit.

b. Close up of goniometer with two dimensional position sensitive detector (General Area Detector Diffraction System (GADDS)).

c. Example of GADDS output.



c

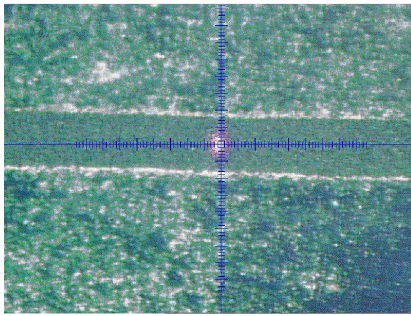


Figure 61a. Location of a 500- μm diameter beam on a YBCO coated conductor tape.

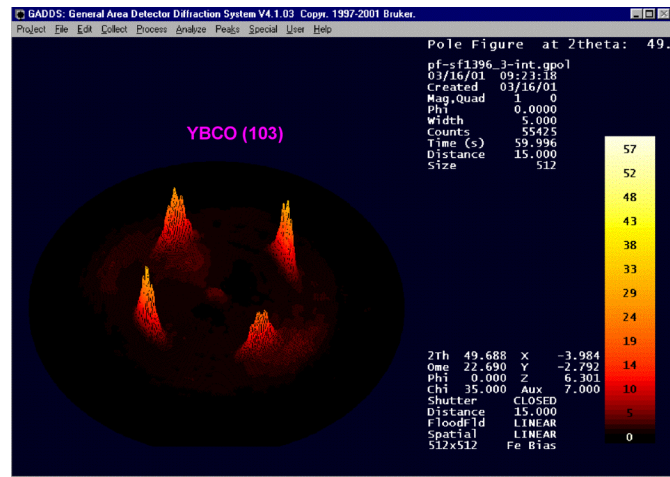


Figure 61b. Pole figure of region in 61a generated in 10 minutes using Bruker D8 Discover and GADDS.

At the final stage of coated conductor manufacture comes the superconductor characterization. This is performed in the Measurements Laboratory, which makes use of reel-to-reel tape transport system, and that will allow both contact (transport current) and non-contact (ac inductive, Hall probe array, etc.) determination of the tape critical current at liquid nitrogen temperature. The data collection will then be integrated with the sample preparation database for process feedback.

Equally importantly to the LANL coated conductor program, the Research Park staff will work in partnership with outside entities on furthering CC fabrication development. External partners will be given the opportunity to use the facility for their own process development. STC's Research Park facility will be a national resource for CC development. Other national labs will be offered use of the facilities to aid in their own research. Universities will be offered collaboration on aspects of basic research, with the possibility of having their students working at the Research Park. Companies will be able to have postdocs stationed at the Research Park Labs under various types of agreements to work with LANL research staff on CC development. The postdocs could act as a knowledge base for company staff to come and use the deposition and characterization facilities in the Research Park labs for their own purposes. The Research Park will also be a training facility for partners who are licensing CC technology.

In addition to the coated conductor development, which clearly will be the focus for the first years of RP operation, the materials labs would get involved in applying IBAD and HTS layers for electronics applications. There are a number of potential superconducting electronics applications where IBAD templates for HTS could be used, such as microwave filters. Initially the work on these applications will take place at LANL labs, but eventually it would migrate to the Research Park. This work would involve other substrate materials, such as ceramics and not necessarily reel-to-reel sample transport. Multi-sample (wafer) capability will be built into sample transport mechanisms.

Applications development research will also be carried out in three laboratories at the Research Park. As an example, one of these labs will be set up for characterization of the transport and magnetic field ac loss of YBCO tapes by electrical and calorimetric measurement techniques (Figure 62) with the capabilities: $I < \sim 100$ A, $T = 75-64$ K, $B = 0-$

100 mT \parallel and \perp to tape plane. Methods to reduce the losses in CC, e.g., by patterning into narrow strips, will be investigated. In addition, a three-phase ac loss cable calorimeter is available to measure losses in 1 m test sections of prototype power cables with currents up to ~ 2 kA_{rms}. This system allows the measurement of ac losses in cables of the “warm-dielectric” design, for which the amount of superconductor material is minimized but for which the phases interact magnetically.

The coated conductor (CC) YBCO tape represents a 2nd generation of high-temperature superconducting (HTS) wire. The 1st generation of HTS wire, i.e. BSCCO tape, is currently coming to commercial production. Both of these superconducting wires are expected to complement low- T_c superconducting (LTS) wires, which are currently commercially available. Applications of each of these materials are expected to be different and require significant research. Additionally, the CC wires need to be characterized carefully in terms of their structural and electrical properties that are required for specific applications. Some of this work is expected to take place at the Research Park facility as well as through outside collaborations. In the Research Park there will be labs where critical temperatures, critical currents, ac losses, and other properties will be measured on the coated conductors and where prototype (“demonstrator”) applications will be developed.

STC will work with outside collaborators, i.e., national labs, universities and companies, on superconductive applications development. The main type of outside collaboration will be in supplying high-quality coated conductor material to entities pursuing measurements and superconductive applications. Groups that are performing measurements and trial applications need sufficient quantities of reliable “standard” materials. Companies that are currently working on making CC’s are not expected to be able to supply such materials commercially before 2004, based on our estimates. Our goal is to provide a standard material that can be distributed within the community in the meantime. Furthermore, there is still no consensus on which processes should be employed for manufacture of CC. We anticipate that the LANL process will provide a benchmark for new processes that are being developed commercially.

In addition, STC will work jointly with universities, other national labs and companies on developing new applications. Our partners in this area will be able to use the Research Park facilities just like the partners on CC fabrication.

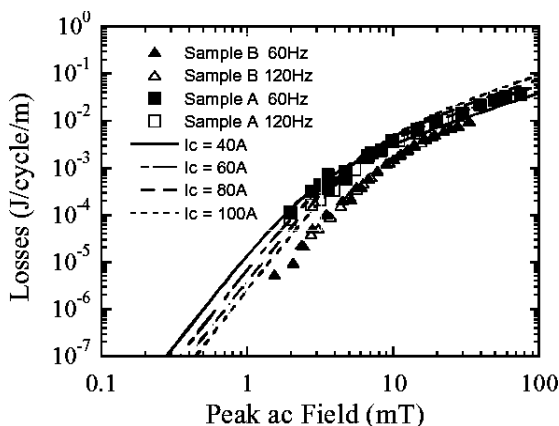


Figure 62a. Ac loss data on YBCO coated conductor.

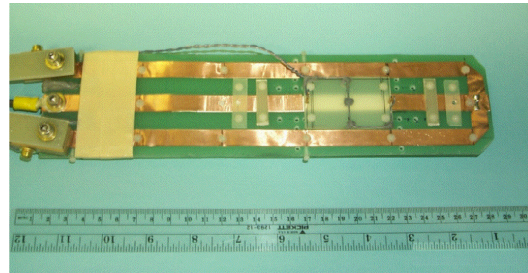


Figure 62b. Probe for measuring ac losses in YBCO tape.

To summarize the accomplishments of the ACCI this year: space has been established for the new labs and offices; building construction is finished; lab equipment procurement has begun; vacuum hardware and other equipment has been ordered; four new technical staff have been hired; initial contacts with possible partners have been made; and Argonne, Brookhaven and Oak Ridge National Laboratories are committed to collaborating at the Research Park.

The Research Park facility allows the opportunity for new partnerships with industry, universities and national labs. The facility allows companies to minimize their financial risk by allowing them to test concepts with a small investment. It allows industry to co-locate with Los Alamos National Laboratory. The basis for industrial collaborations can be User Facility Agreements and/or CRADA's

Plans for Fiscal Year 2002 include the set up the Coated Conductor labs at the Research Park; demonstration of a working continuous processes for coated conductors; demonstration of the *in-situ* monitoring/diagnostics capabilities described above; ac-loss measurements on long coated conductors; the establishment of an open environment for research and a user facility where various parties can work together; and the establishment of meaningful partnerships with interested parties.

The ACCI effort at Los Alamos is an aggressive program for Coated Conductor research and development with the goals for establishing the following: *High-throughput* sample preparation and characterization in *continuous* processing; *in-situ* and *real-time* process diagnostics; an applications effort using coated conductors; an open environment for industrial partnerships; user facility and relevant training; and educational opportunities for postdocs and students.

2.1.6 Scale-up of Coated Conductor Technology at IGC-SuperPower

(IGC-SuperPower (now SuperPower): V. Selvamanickam, Y. Li, C. Park, S. Sathiarju, J. Reeves, Y. Qiao, K. Lenseth), LANL: P.N. Arendt, E.J. Peterson, S.R. Foltyn, J.Y. Coulter, B.E. Newnam)

IGC-SuperPower executed a Cooperative Research and Development Agreement (CRADA) with Los Alamos National Laboratory and Argonne National Laboratory in January 2000 to scale up coated conductor processing to full-scale manufacturing. For the final process, IGC-SuperPower requires high yield, high throughput, high current product, and simple controls. The LANL demonstration process, using ion beam assisted deposition (IBAD) to provide the template layer and pulsed laser deposition (PLD) to deposit buffers and the YBCO, is a simple, proven, reproducible, high-rate process with few variables. Thus, this CRADA was an excellent match between manufacturing requirements and Laboratory demonstrations.

There has been strong collaboration between IGC-SuperPower & LANL in the scale-up effort. Quarterly meetings were held to evaluate progress and weekly conference calls to assure good and timely feedback. IGC-Superpower scientists and engineers were trained at the LANL process facilities and LANL personnel visited IGC-SuperPower to evaluate and assist in characterization techniques. In addition, key process patents were licensed to IGC-SuperPower.

IGC-SuperPower has invested substantial resources to scale-up coated conductor technology. A pilot-scale manufacturing facility was established in a 1000 sq. ft. Class-10,000 clean room. This was expanded to 2000 sq. ft. in June '01. The clean room houses the pilot-scale buffer and YBCO deposition facilities and the characterization equipment. Auxiliary systems, e.g., reel-to-reel polishing rig are outside the clean room area.

IGC-Superpower is now routinely polishing long lengths of metal substrates using the Reel-to-Reel Polishing Rig, Figure 63. This system was designed and constructed to polish in one pass > 100 m lengths of metal substrate with a high degree of surface smoothness for coated conductor deposition. Several tens of meters of metal tape have been polished for buffer deposition. Surface roughness of long tapes polished in this system is comparable to that of those polished manually. As determined by AFM, the manually polished tape, Figure 64, had a rms surface roughness (R_a) of 1.5 nm over a $20,000\text{-}\mu\text{m}^2$ area.

A pilot-scale IBAD template buffer deposition facility (Figure 65) was established at IGC-SuperPower in December 2000. It is contained in a 56" cube box coater. The equipment is rated for continuous operation for greater than 600 hours. It contains a source feed sufficient for one week of operation. The deposition zone is > 20 cm. It has resulted in achievement of an IBAD template buffer layer on a 20-cm long metal substrate (Figure 66) with an in-plane texture (ϕ scan full width at half maximum (FWHM) of $23^\circ \pm 1^\circ$.



Figure 63. Reel to reel polishing rig designed, built, and operating at IGC-SuperPower for polishing >100 m lengths of tape.

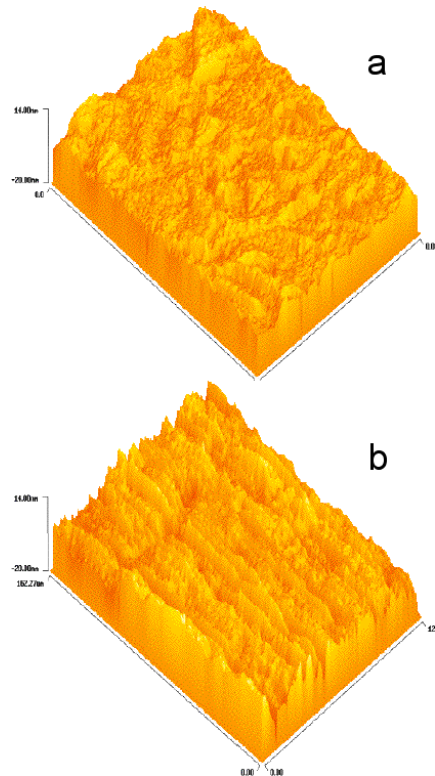


Figure 64. Surface roughness profiles of (a) a manually polished tape ($R_a=1.5$ nm) and (b) a tape polished in the system shown in Figure 1 ($R_a = 2.9$ nm).



Figure 65a. Pilot-scale IBAD template buffer deposition facility at IGC-SuperPower.

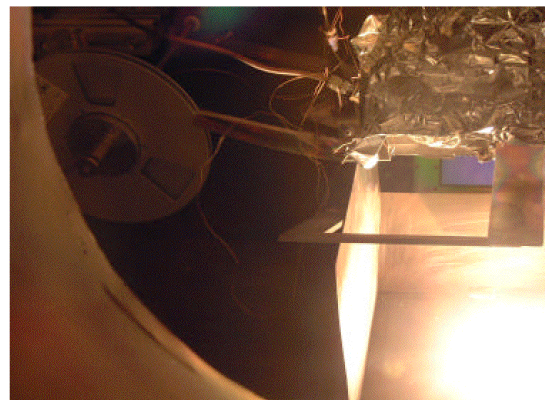


Figure 65b. Interior view of box coater chamber.

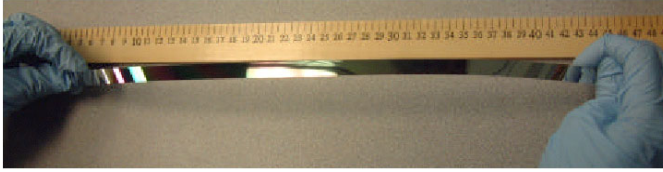


Figure 66. Metal alloy substrate coated with IBAD template layer.

A pilot-scale YBCO deposition facility was also established in December 2000. It consists of a 78"-long vacuum chamber, Figure 67, for YBCO deposition by pulsed laser deposition (PLD) and of a second station for sputtering of silver onto the YBCO film. The PLD system has computer control of the target rotation, rastering, and indexing. The system also has automatic monitoring and control of the target erosion beam energy inside chamber.

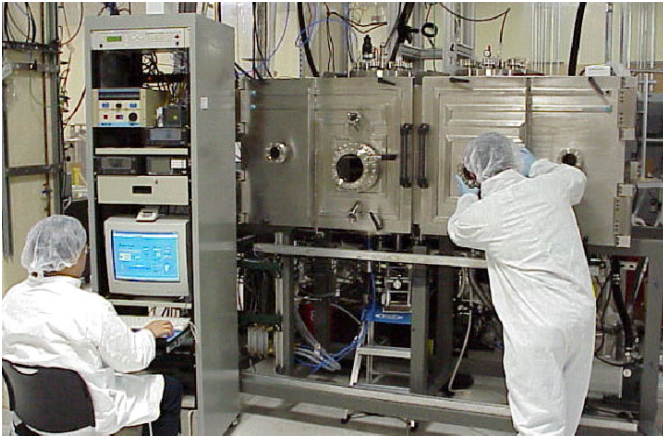


Figure 67. View of YBCO deposition chamber.

The YBCO deposition chamber has produced high quality YBCO coatings on metal tape (Figure 68). Typical critical current density J_c values achieved are 1 to 2 MA/cm² with a maximum of 4 MA/cm². IGC-SuperPower continues to aggressively scale up coated conductor technology to manufacturing operations in close collaboration with LANL.

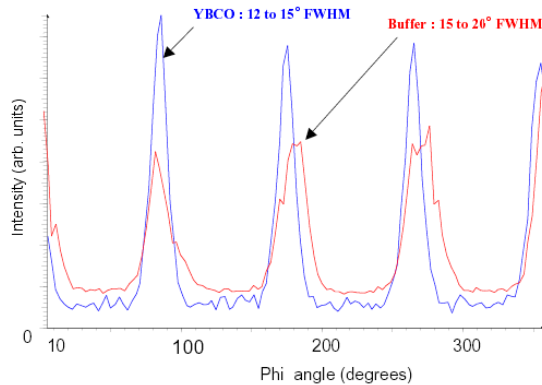


Figure 68a. Phi scans of YBCO film and underlying buffer layer. The YBCO has an in-plane texture of 12 to 15° FWHM.

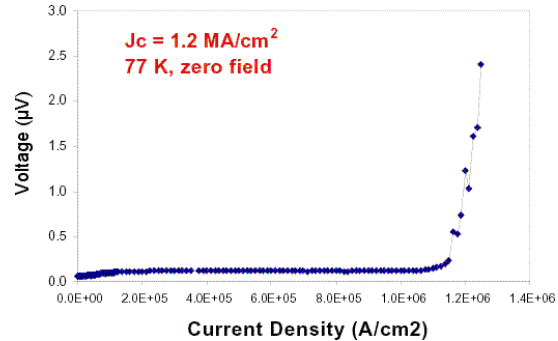


Figure 68b. Voltage/current density characteristic for a YBCO coated conductor at 77 K and self-field.

2.1.7 Development of the Superconducting Phase and the Origin of Potential Current Limiting Defects in Bi-2223 Tapes

(T.G. Holesinger, J.F. Bingert, American Superconductor Corp.: R.D. Parrella and G.N. Riley, Jr.)

Oxide-powder-in-tube (OPIT) $(\text{Bi,Pb})_2\text{Sr}_2\text{Ca}_2\text{Cu}_3\text{O}_y$ (Bi-2223) tapes are currently the only HTS conductors that are available in long lengths and meet the performance levels needed in practical applications. However, the best critical current densities (J_c s) in oxide-powder-in-tube (OPIT) $(\text{Bi,Pb})_2\text{Sr}_2\text{Ca}_2\text{Cu}_3\text{O}_y$ (Bi-2223) tapes are only a fraction of the values obtained in thin film architectures. Assuming the structure of the thin film to be optimized, it is important to understand the differences in structure between them. Two aspects of the structure are important: structure/property relationships in fully processed tapes and the processing/structure relationships that develop during manufacturing. The former are important in gauging the effects of various defect structures on the properties of the Bi-2223 tapes. The latter are important in determining (and rectifying) the origin of detrimental defects. Because there are a relatively large number of defect structures in Bi-2223 tapes, their effects on the transport properties are convoluted.

The scope of the problem can be reduced with an understanding of some key structure/property aspects of the Bi-2223 system. Work at Brookhaven National Laboratory suggests that strong c-axis textures should be sufficient to produce strongly-linked material provided that the majority of the grain boundaries are not basal-plane terminated. The latter type of boundary is one in which the grain-boundary plane is defined by one and only one of the connecting grains' (colonies') ab plane. Work at Univ. Wisconsin shows that the J_c values across 200 μm long filaments are variable and have J_c levels that are at most only 50% higher than those measured on the centimeter length scale; the conclusion is that defect structures below a length scale of 200 μm define the current limiting mechanism in Bi-2223 tapes.

Coupled with the length scale for the active current limiting mechanism is the belief that most of the transport current in Bi-2223 tapes is carried close to the silver interface. Hence, it is of interest to document this structure and determine the conditions during processing that shape its development. In this work, phase and microstructure development in Bi-2223 tapes were examined with an emphasis on defect structures that form near the silver interface during the normal course of processing.

Bi-2223 tapes at various stages of processing were examined by electron microscopy. The starting composition of the Bi-2223 powder used in the tapes was $\text{Bi}_{1.7}\text{Pb}_{0.3}\text{Sr}_{1.9}\text{Ca}_{2.0}\text{Cu}_{3.0}\text{O}_y$. Tapes were examined after specific dwell times in the initial heat treatment, after intermediate deformation, and after full processing. The critical current densities (J_c) of the fully processed tapes reached 70 kA/cm^2 at 77 K and self-field. The tapes were examined from three principle directions of view in an analytical electron microscope (AEM): short transverse section, longitudinal transverse section, and plan view. Electron back-scattered diffraction (EBSD) was performed in a SEM. EBSD pattern indexing and misorientation calculations assumed tetragonality of the Bi-2223 lattice.

The development of the microstructure in Bi-2223 tapes starts with the initial ramp up to temperature and the formation of a liquid phase during the initial stages of the heat treatment, as shown in Figures 69a and b. During the initial ramp, large alkaline-earth cuprate (AEC) phases develop; in particular, the $(\text{Sr,Ca})\text{CuO}_2$ (1:1 AEC) phase grows as

large needles, which can exceed 10 μm in length, while the $(\text{Sr,Ca})_{14}\text{Cu}_{24}\text{O}_{41}$ (14:24 AEC) remains as a blocky phase 1-2 μm in size. The AEC's can adversely affect the alignment and growth of the Bi-2223 phase. The formation of the liquid phase in the early stages of heat treatment involves both the AEC's and Bi-2212 phases. Its formation was slow, yet the liquid phase appeared to be stable, and its average composition was $\text{Bi}_{1.24}\text{Pb}_{0.92}\text{Sr}_{0.70}\text{Ca}_{0.44}\text{Cu}_{1.70}\text{O}_y$. Bi-2223 development did not start until sufficient liquid phase had developed, and all Bi-2223 grains found in the early stages of heat treatment were associated with a liquid phase. An effect of this growth process is to lock in the triangular pore structure that the liquid phase occupies as it forms and leaves behind as it is consumed to form Bi-2223.

The Bi-2223 phase continues to form until it comprises the majority of the phase content of the filaments. At the end of the first heat treatment, most of the grains contain Bi-2212 intergrowths. Secondary phases and residual porosity are found primarily in the middle of the filaments, as shown in Figure 70. Many of the misaligned Bi-2223 grains have their origin at second phases, defects, or roughness at the silver/BSCCO interface. In addition, the large, residual secondary phases play a significant role in the microstructure formation during intermediate deformation as discussed below.

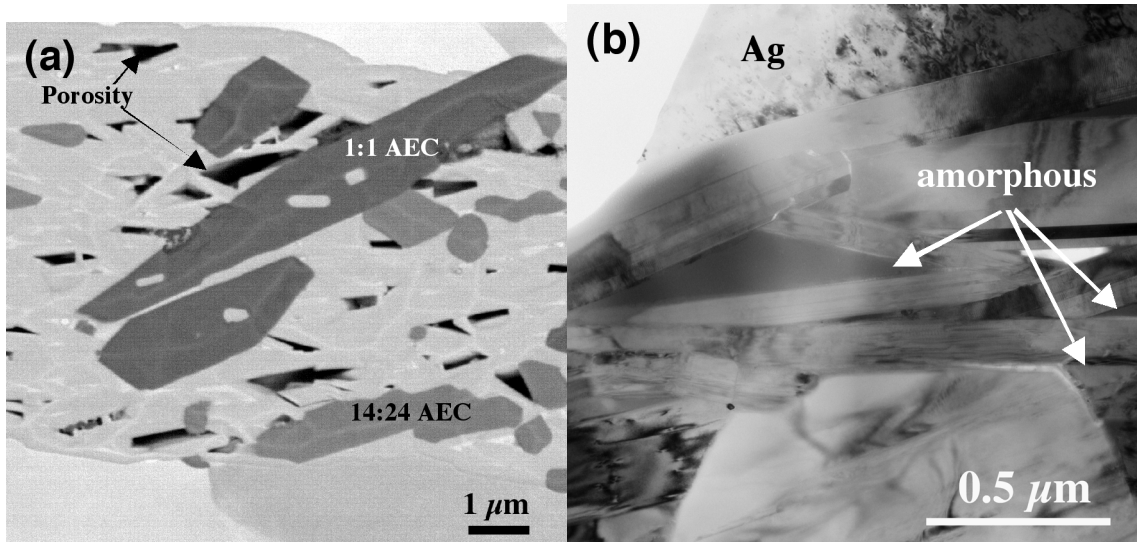


Figure 69. SEM micrograph (a) of a Bi-2223 filament after the initial ramp up to the processing temperature. The phases present were Bi,Pb-2212, 1:1 AEC, and the 14:24 AEC. The TEM micrograph (b) shows the transient liquid phase filling the voids between the Bi,Pb-2212 grains for a sample that was processed at temperature for 300 minutes in 7.5% O_2 prior to the quench.

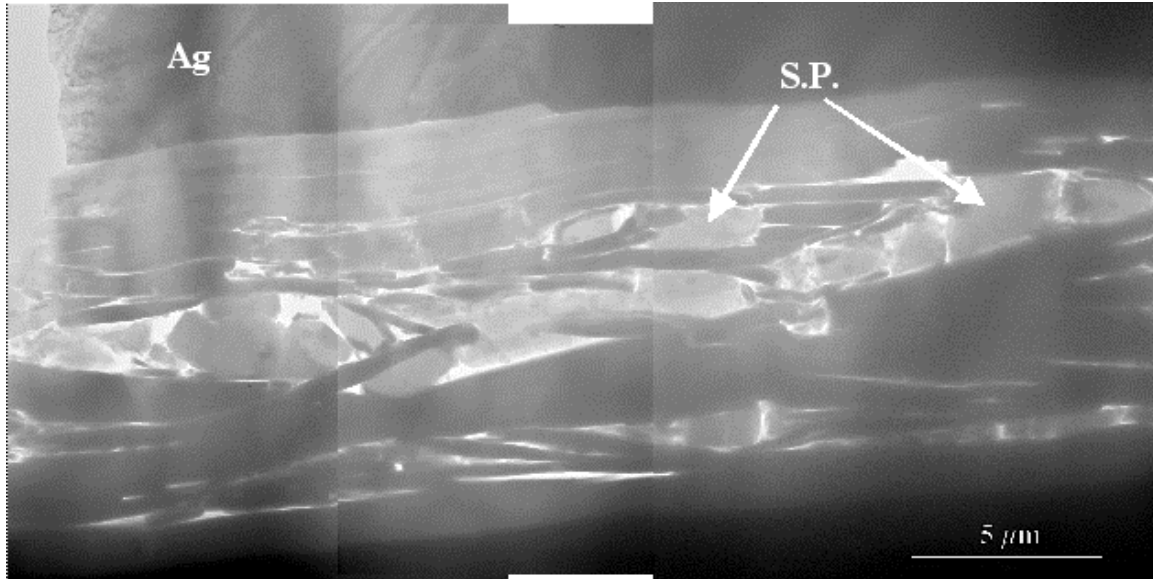


Figure 70. TEM longitudinal cross section of a Bi-2223 filament from a tape after the full first heat treatment. A well-formed Bi-2223 colony structure occurs next to the silver sheath while porosity, second phases, and misaligned Bi-2223 grains dominate the filament interior.

The effect of an intermediate deformation is to reduce porosity and bring the unreacted components into closer contact to complete the Bi-2223 conversion process and improve the properties of the tape. The typical microstructure after this step is shown in Figure 71. However, there are several detrimental effects. First, the secondary phases, namely 1:1 and 14:24 AEC's, are generally non-deformable, as opposed to the matrix, and lead to roughening of the silver interface, as shown in Figure 71. The silver hillocks formed along the interface lead to significant changes in the grain boundary structure. As the Bi-2223 matrix adjusts to the morphology of the interface, an increase in the number of high-angle grain boundaries occurs, as shown in Figures 72a and b. A second effect occurs within the Bi-2223 matrix when it fails under tension during deformation and cracks form as shown in Figure 73. Slip along the basal plane allows for discontinuities in the cracks across the grains.

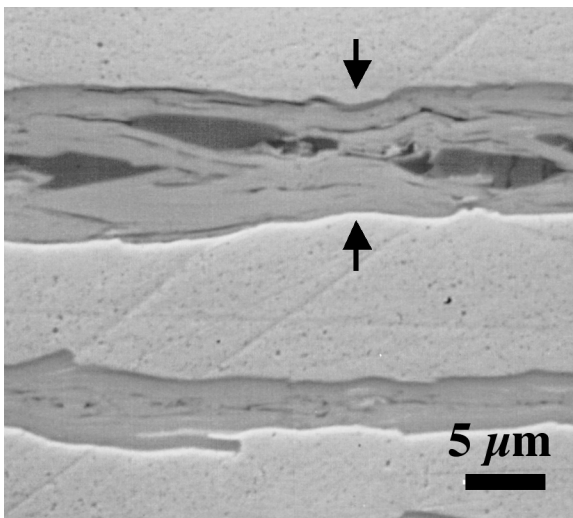


Figure 71. SEM micrograph of a Bi-2223 tape after an intermediate deformation.

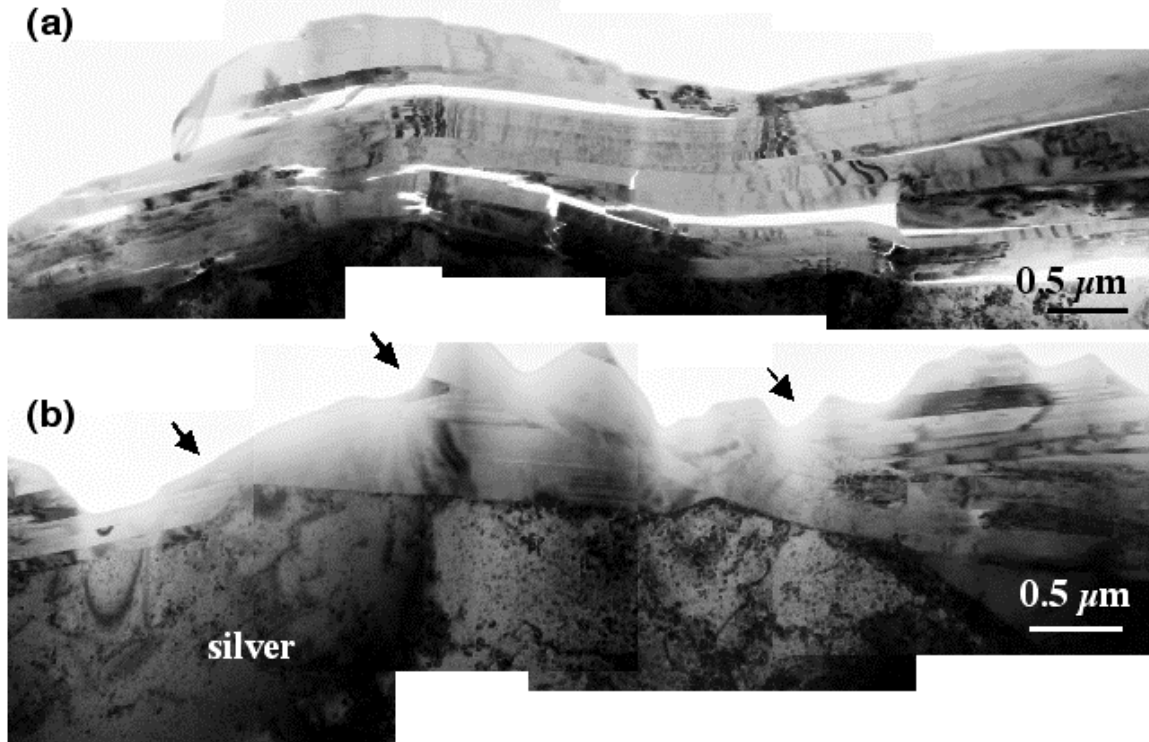


Figure 72. TEM micrographs of (a), the crack structure in the Bi-2223 matrix around a silver hillock and (b) the resulting structure around a silver hillock in a fully processed Bi-2223 tape. In (b), a number of basal-plane terminated grain boundaries have formed during the final sinter as a result of crack healing and the need accommodate the morphology of the silver hillock.

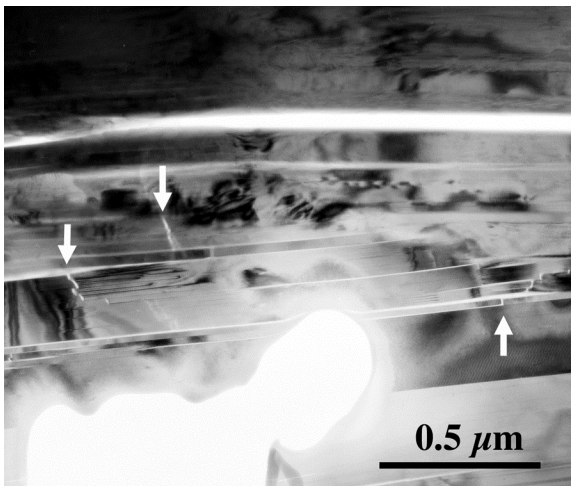


Figure 73. TEM micrograph of a Bi-2223 tape after the intermediate deformation. The failure of the matrix is illustrated by the marked crack structures.

Many of the microstructural features present after the first heat treatment reappear after the final heat treatment as shown in Figure 74. Large pores can be seen in the SEM micrograph. The AEC's are confined primarily to the filament centers. The TEM image, Figure 74b, shows the well-formed colony structure next to the silver, which supports our belief that most of the current flows in this region. Barriers to current flow arise in this region when the Bi-2223 matrix must traverse inhomogenities in the silver sheath as indicated in Figure 74a. As shown in Figure 72b, the matrix recrystallizes to form high angle grain boundaries, many of which are basal-plane terminated. Assuming a random

misorientation distribution, the breadth of c-axis texture ($\approx 10^\circ$ FWHM at best) implies that most colonies will be tilted along the c-axis with respect to their neighbors.

No mesoscopic ordering of orientations between colonies was found that would satisfy the Dimos criterion (low angle grain boundary required for good current transport), as indicated by the electron backscattered diffraction (EBSD) results of Figure 75. An analysis of 101 boundaries formerly adjacent to the silver interface from etched samples revealed an initial misorientation distribution weighted toward low-angle boundaries, as shown by the black bars in Figure 75a. However, inspection of SEM micrographs from which the data were collected, for example Figure 75b, reveals that many of the boundaries of less than 10° misorientation appear to be ledges defining intracolony grain boundaries. These intracolony boundaries are expected to be characterized by small angular misorientations. Excluding apparent intracolony boundaries results in a nearly random distribution of intercolony boundaries, as shown by the gray bars in Figure 75b. In general, most edge colony boundaries were found by TEM to be mixed; edge and basal-plane terminated grain boundaries both comprise the colony-to-colony connections along the filament as shown in Figure 76. Finally, secondary phases, in particular the 3221 phase, can affect the local chemistry in adjacent Bi-2223 colonies as we have discussed previously. For example, the average composition of several Bi-2223 grains attached to a 3221 phase was $\text{Bi}_{1.96}\text{Pb}_{0.07}\text{Sr}_{1.84}\text{Ca}_{2.11}\text{Cu}_{3.02}\text{O}_y$. Those not directly attached had an average composition of $\text{Bi}_{1.83}\text{Pb}_{0.28}\text{Sr}_{1.87}\text{Ca}_{2.01}\text{Cu}_{3.01}\text{O}_y$.

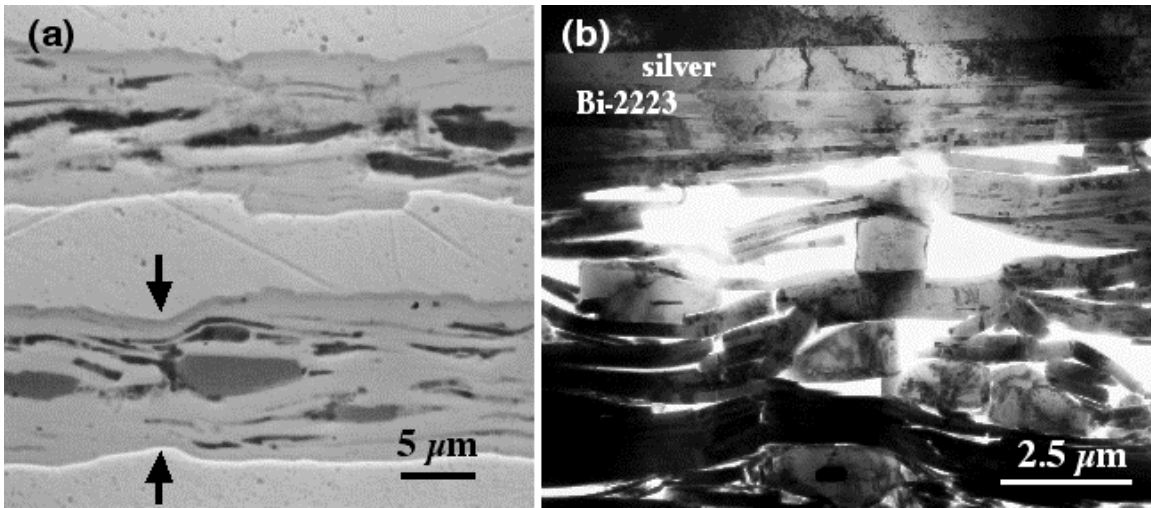


Figure 74. The roughened silver interface, porosity, and secondary phases present after the final heat treatment can be (a) seen in the backscattered electron image and (b) TEM image. Both images were taken with the sample viewed in cross section perpendicular to the long axis of the tape.

The amounts of porosity, secondary phases, and misaligned grains found in the filament centers provide a convincing argument that most of the current is carried in the colony structure next to the silver interface. The presence of secondary and liquid phases early in the heat treatment provides ample nucleation sites for misaligned Bi-2223 grains and the development of porosity. The silver sheath provides a stabilizing template to minimize these effects. Within the colony structure next to the silver, three major types of defects have been identified; chemistry variations due to secondary phases, matrix cracks arising from mechanical deformation, and basal plane terminated grain boundaries that comprise a significant fraction of the edge colony boundaries. The local Pb variation around the 3221 phase may affect the local critical current density of the matrix. The affected area of the colony structure is larger than the actual size of the secondary phase, and new

processing routes should be found to minimize the presence of the 3221 phase. Cracks within the matrix are an impediment to current flow based on magneto-optical imaging (MOI) and TEM. Adjustments need to be made in the processing to minimize residual cracks in fully processed tapes.

Of particular interest was the EBSD analysis, which did not reveal any misorientations between colonies on a mesoscopic scale that would fall within the Dimos criterion. Rather, the results support the Bi-2212 bi-crystal work that suggests BSCCO grain boundaries are strongly linked provided that the basal plane of one of the grains does not comprise part of the boundary. The primary gating mechanism for current flow in Bi-2223 tapes may be the fraction of basal plane terminated grain boundaries that comprise the edge colony boundaries. Tilting and recrystallization of the colony boundary structure accommodates inhomogenities in the silver sheath. Particularly worrisome are the large silver hillocks that form during intermediate deformation due to the presence of large AEC's. The distance between such defects falls well within 200 μm length scale suggested by MOI. The benefits of reduced porosity and shorter diffusion lengths that arise from the intermediate deformation may be partially offset by an increase in undesirable grain boundary structures. Improvements in performance are likely to come with new methodologies for reducing the secondary phase grain size prior to the intermediate deformation step or new deformation techniques that reduce the roughness along the silver / Bi-2223 interface.

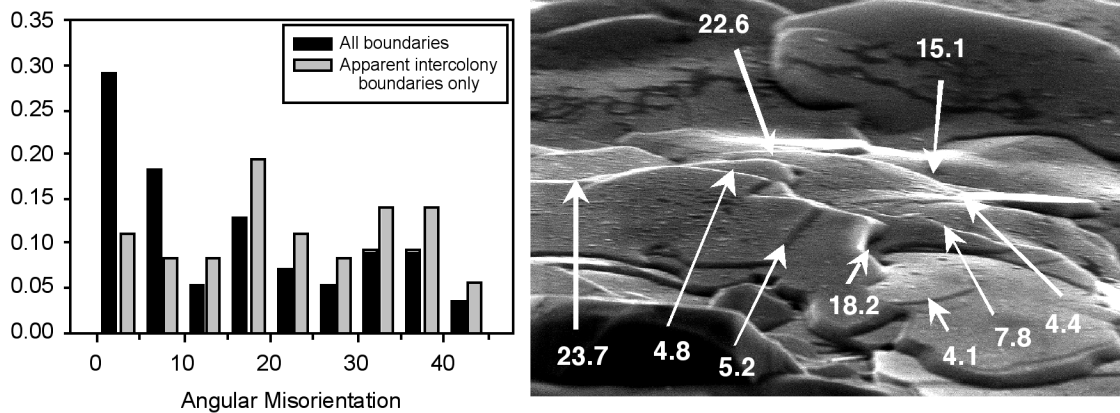


Figure 75. EBSD data from etched Bi-2223 samples showing, a) the angular misorientation distribution for all boundaries measured *versus* only those that appear to be intercolony boundaries, and b) a representative SEM (70° tilt) micrograph with misorientations identified, showing the intracolony appearance of several low-angle (<10°) boundaries.

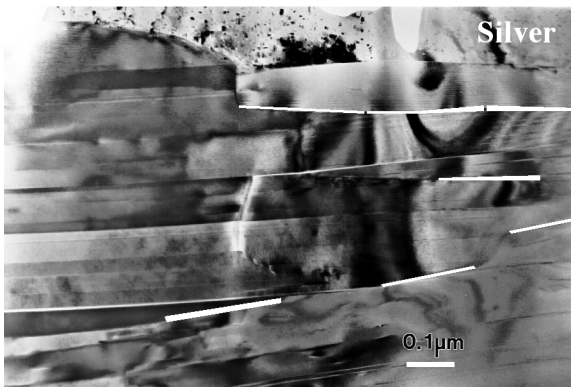


Figure 76. TEM micrograph of a typical colony boundary in a Bi-2223 tape. The white lines indicate the portions of the colony boundary where the grain boundaries are basal-plane terminated.

Microstructural analysis of the filament structure in Bi-2223 tapes suggests that most of the transport current is carried in the colony structure next to the silver sheath. Within this latter area, three main defect structures were found: chemistry variations due to secondary phases, matrix cracks arising from mechanical deformation, and basal plane terminated grain boundaries that comprise a significant fraction of the edge colony boundaries. No mesoscopic ordering between colonies was found that would satisfy the Dimos criterion. Most edge colony boundaries are actually comprised of both edge and basal-plane terminated boundary segments, and the fraction of the latter may be the gating mechanism for current flow. Inhomogeneities in the silver sheath are thought to increase the fraction of the basal-plane terminated grain boundaries, which are considered to be detrimental to the transport current.

2.1.8 Effect of Lattice Strain and Defects on the Superconductivity of MgB₂

(A. Serquis, Y. T. Zhu, E. J. Peterson, J. Y. Coulter, D. E. Peterson, and F. M. Mueller)

Since the discovery of superconductivity in MgB₂ at 39 K, considerable progress has been made in the understanding of the fundamental properties of this material. It is well known that lattice defects, strain, and vacancies may affect the physical properties of superconductors, such as superconducting transition temperature T_c and the critical current density J_c . However, there are so far no studies on the influence of lattice strain and defects on the superconductivity of MgB₂. The objective of this study is to understand the influence of structural defects (i.e., Mg vacancies) and the lattice strain on the superconducting properties of MgB₂.

MgB₂ samples were synthesized using an atomic ratio of Mg:B = 1:1 at 750 or 900°C under flowing Ar. The starting materials were amorphous boron powder (-325 mesh, 99.99% Alfa Aesar) and Mg turnings (99.98% Puratronic) or powder (-325 mesh, 99.8% Assay). Three different samples were prepared using varying starting materials and/or synthesis temperatures (see Table I). Boron powder (sample A) or a B+Mg powder mixture (samples B and C) was pressed into pellets (5 mm in diameter X 34 mm in thickness). The pellets, and the Mg turnings for sample A, were wrapped in Ta foil and placed in an alumina crucible inside a tube furnace under ultrahigh purity flowing Ar. The samples were heated for 1 h to the synthesis temperatures (see Table I), cooled at 0.5°C/min to 500°C, heated again for 1 h at the synthesis temperature, and then furnace cooled to room temperature. Sample C was preheated at 600°C for 5 h.

Table I. Synthesis parameters and lattice constants for samples A, B, and C.

Sample	Starting materials and processing states	Synthesis temperature (°C)	Lattice constants a (Å)	c (Å)
A	B powder pellets + Mg turnings	900	3.0860	3.5204
B	B + Mg powder mixture pellets	900	3.0842	3.5237
C	B + Mg powder mixture pellets	750	3.0849	3.5228

A superconducting quantum interference device magnetometer (Quantum Design) was used to measure the magnetic susceptibility of the samples over a temperature range of 10–45 K in an applied field of 10 Oe. As can be seen in Figure 77, all samples have sharp transitions, with T_c s given in Table II. It is interesting to note that in the inset of Figure 77 the superconducting transition of sample A ($\Delta T_c \sim 0.5$ K) is several times sharper than that of a commercial powder ($\Delta T_c \sim 11$ K).

The Mg vacancies and strain were determined by Rietveld analysis of powder x-ray data, collected using a Scintag XDS2000 θ – θ powder diffractometer. The data were refined using the computer program GSAS as a mixture of MgB₂ (space group $P6/mmm$), MgO ($Fm-3m$), and Si ($Fd3m$) standard. The fraction of MgO was ~ 5 wt% for all samples.

From the x-ray measurements we observed that samples with lower T_c have a greater peak broadening. It is well known that the x-ray peak broadening can be caused by both crystallite size and lattice strain. Any type of lattice defect, such as vacancies, interstitials, substitutions, and stacking faults, can cause strain broadening. For the strain and size broadening analysis two procedures with similar results were used.

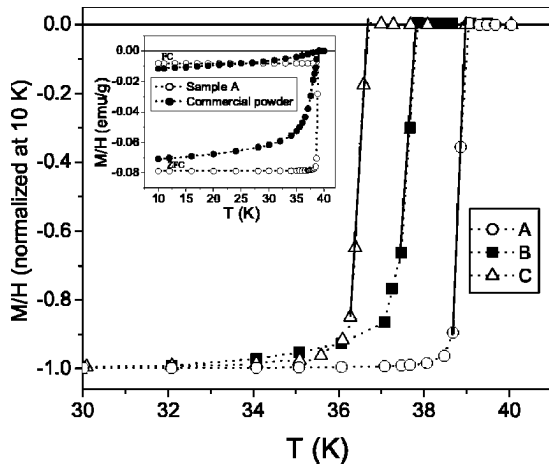


Figure 77. Magnetic susceptibility of MgB_2 samples as a function of temperature. A constant magnetic field of 10 Oe was applied. The solid lines were used to determine the T_c s. In the inset, sample A is compared with commercial MgB_2 powder.

(i) GSAS: the strain and particle size broadening can be calculated from refined L_x and L_y parameters, using as instrumental parameters the values obtained from the LaB_6 profile standard SRM 660. All samples showed negligible size broadening.

(ii) WH (Williamson–Hall) plot: the strain value can be estimated from the slope and the crystallite size from the intercept in a plot of the calculated full width at half maximum (FWHM) $X \cos \theta$ vs. $\sin \theta$. For Lorentzian profiles, which correspond to this analysis, this should yield a straight line if the strain is isotropic. Even though the contribution to size broadening was negligible in x-ray diffraction, the scanning electron microscopy (SEM) observations denote a smaller grain size of samples B and C, which were synthesized using Mg powder (see Table II).

Table II. Structural features of each sample. The Mg occupancies were estimated from the variation of χ^2 .

Sample	T_c (K)	Grain size (SEM) (μm)	Strain %		Mg occupancy
			GSAS	WH plot	
A	38.9 ± 0.2	0.5–5.0	0.294(30) 0.309(5)		0.994(5)
B	37.8 ± 0.3	0.1–0.9	0.674(60) 0.665(6)		0.973(5)
C	36.6 ± 0.3	0.1–0.7	1.091(80) 1.079(8)		0.945(5)

To refine the Mg occupancy in the MgB_2 phase, we first determined its approximate value by manually checking the goodness of fit, χ^2 , as a function of Mg occupancy. From the Williamson–Hall plots shown in Figure 78(a), it can be seen that since the intercept values are close to the Si value, the contribution of crystallite size to the broadening of the peaks is negligible (in agreement with the Rietveld results) and that the strain values ϵ calculated from the slope are in agreement with the strain values calculated from the GSAS analysis (see Table II).

The results presented in Figure 78(a) have been calculated using an isotropic strain model, but it is possible to achieve an even better fit by including an anisotropy coefficient to describe the strain broadening for the pseudo-Voigt function used in the GSAS. Figure 78(b) compares the Williamson–Hall plots for both models for sample C. The difference in the slopes for the 00 l and $hk0$ reflections indicates a clear strain

anisotropy, with a higher strain value in the c axis (0.95%) than within the a - b plane (0.79%).

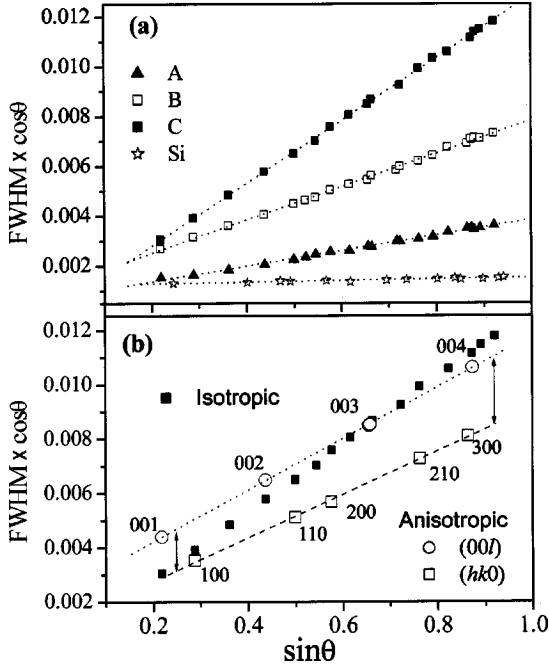


Figure 78. Williamson-Hall plots (FWHM values were obtained from the Rietveld analysis): (a) Isotropic models for Si and MgB_2 phases in samples A, B, and C. (b) Comparison of isotropic and anisotropic model for sample C. For clarity we have only included $(00l)$ and $(hk0)$ Bragg reflections corresponding to the c axis and a - b plane.

It is clear from Figure 79 that there is a strong correlation ($\sim 99\%$) between the T_c and the lattice strain. The change in T_c with strain is in agreement with the fact that in the MgB_2 system, T_c also decreases quasi-linearly with applied hydrostatic pressure, which causes a higher compression along the c axis than along the a axis. Although the average lattice parameters are the same in all three samples, small local variations caused by microstrains are likely the origin of the reduction in T_c .

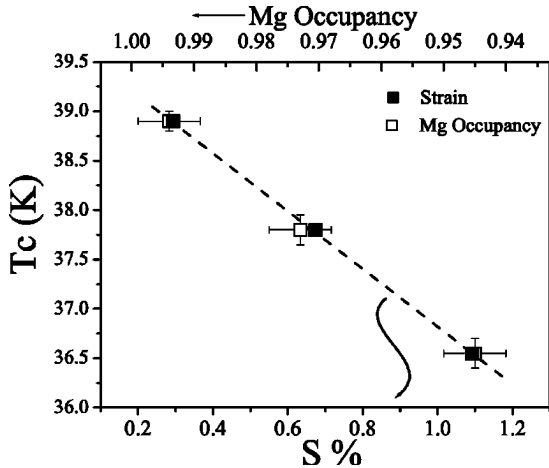


Figure 79. T_c as a function of the derived isotropic strain and the Mg occupancy. The results show the same dependency of T_c on both the strain and the Mg site occupancy.

Most strain values reported for other superconductor materials are smaller than 0.5%, and such a small strain may change the critical current or T_c by more than 50% in some materials. Therefore it is surprising that despite the large strain (1%) in our MgB_2 samples, the shift in T_c is only 2 K.

There are two possible explanations for the observed strain broadening in the samples: a real microstrain due to the presence of MgO inside the MgB₂ grains; and lattice defects based on Mg vacancies. Workers at Brookhaven National Laboratory reported that MgO particles, present as a second phase in MgB₂, can generate dislocations. Our high resolution transmission electron microscopy observations indicate that sample A contains coherent Mg(B,O) precipitates within the MgB₂ grains. However, another sample that does not have any precipitates shows exactly the same strain value as sample A. Therefore Mg deficiency is likely the cause of the observed strain. The data in Table II indicate that Mg vacancies exist in the samples.

In our MgB₂ samples, the highest vacancy concentration was about 5%, or for each Mg layer, approximately one vacancy in the third nearest neighbor or at an average distance ~ 13.6 Å. Assuming random occupancy of the vacancies on the Mg sites, the chance that a Mg vacancy has another vacancy either above or below along the *c* axis is 0.05 or about one chance in 400. We have not seen any evidence for such supercell ordering in our x-ray data of sample C, the one with the highest vacancy concentration. So we assume that a vacancy within a Mg layer has no concomitant vacancy in either the upper or lower neighboring Mg layers. The local strain of the vacancy produces distortions or fine structure on both sides of each Bragg peak.

In summary, the influence of lattice strain and Mg vacancies on the superconducting properties of MgB₂ samples has been investigated. High quality samples with sharp superconducting transitions were synthesized. The variations in lattice strain and Mg vacancy concentrations were obtained by varying the synthesis conditions. It was found that high (and anisotropic) strain ($\sim 1\%$) and the presence of Mg vacancies ($\sim 5\%$) resulted in lowering the T_c by only 2 K. The study of strain effects in MgB₂ films or wires could be an important issue for applications in this material.

2.2 Systems Technology

2.2.1. Fault Current Limiter Restoration Project

(H.J. Boenig, J.A. Waynert, C.H. Mielke, J.O. Willis, J.E. Serna, D.A. Roybal, (General Atomics: B.L. Burley)

A fault current limiter, FCL, is a device in an electrical system that reduces short circuit or fault currents to smaller current amplitudes. It can limit these currents in the first few cycles (to 80 ms) and can be less than a cycle, because the impedance of the inductor is immediately put into the circuit, following a fault until the mechanical breaker interrupts the current. By limiting the load current the FCL can provide disturbance isolation. Although this is a highly desired network component, it is not presently available. Figure 80 shows a schematic of the introduction of the FCL to a typical utility circuit. Its proper operation can prevent damage from fault currents to various components of the electrical grid and prevent interaction with other load circuits. Figure 81 shows the result of a modal calculation of a fault current with and without the FCL.

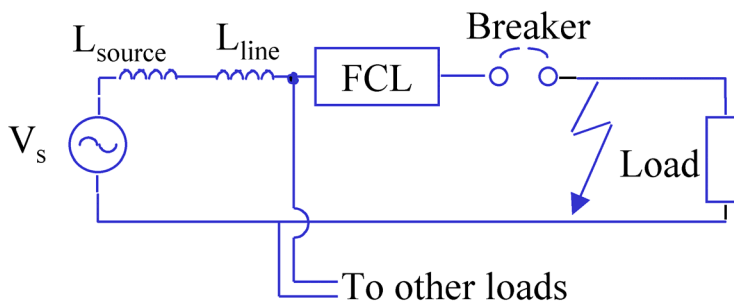


Figure 80. Schematic circuit diagram of the Fault Current Limiter in a typical utility application.

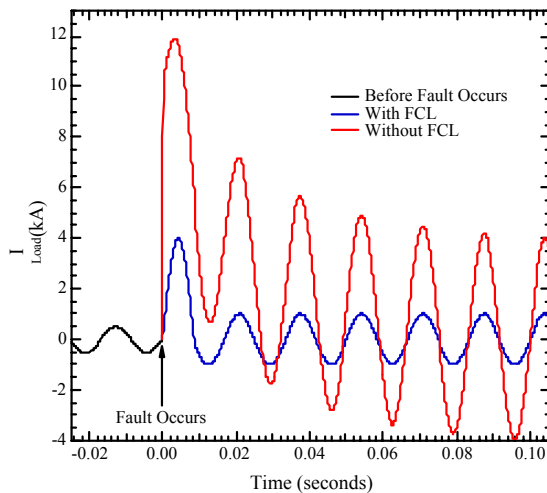


Figure 81. Model calculations of the load current in kA showing the steady state 0.5 kA peak current that rises to almost 12 kA peak immediately and has a significant dc component after the fault. The FCL limits the maximum current to only 4 kA peak on the first cycle and to 1 kA peak subsequently, with almost zero dc offset.

The system at Los Alamos uses a bridge-type FCC concept that is significantly different from competing concepts. The FCC is a combination of an HTS coil that provides the extra impedance in the circuit, which limits the initial fault current, and power electronics

circuits arranged in a bridge configuration, see Figure 82. The power electronics assume the voltage blocking, and therefore current limiting function after the initial half cycle of the fault condition, thus relieving the HTS coil of those functions. *Fault current limiting is automatically initiated* by adjusting the triggering angle of the thyristors (power electronics). The maximum fault current is continuously adjustable from zero to the peak value, and thus this system is called a fault current controller, not just a fault current limiter. The system therefore can also be operated as a sub-cycle solid state breaker. The bias power supply, initially thought to be required to establish a dc bias across the coil and to assure that all the thyristors were forward biased during normal operation, is not essential. The bias can be established automatically by the charging current of the coil. The FCC system is suitable for multiple reclosures with minimal delay after a fault, in marked contrast to the case for other FCL designs. It is more versatile than alternative HTS-FCL systems and is suitable for high power operation. The 15 kV prototype was designed for 26 MVA operation. The HTS coils, power electronics, and associated control and cooling systems were installed on a semitrailer, see Figure 83.

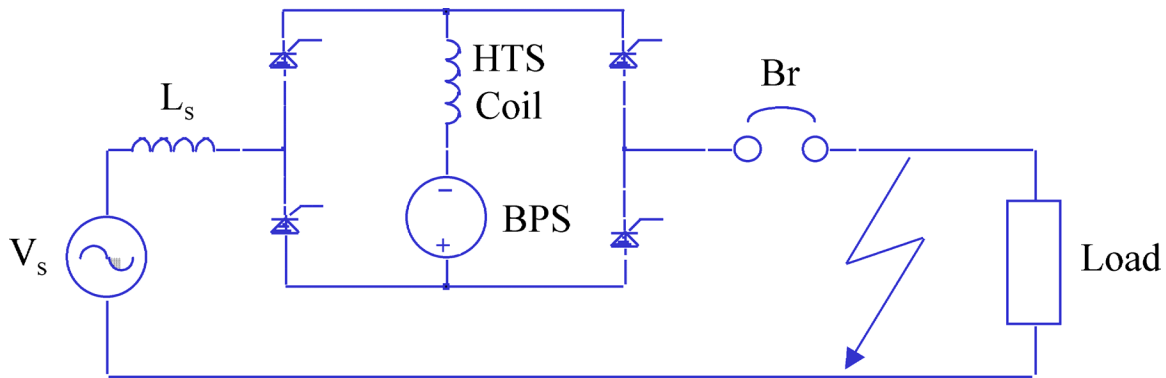


Figure 82. Schematic of a bridge-type FCC.



Figure 83. The FCC located next to the NHMFL substation at Los Alamos National Laboratory after the tests in a Southern California Edison substation.

In 1999, the FCC was taken to a substation of Southern California Edison for testing. During a three-phase 12.4 kV no load voltage test, there was a voltage breakdown in the vacuum system of phase A. Single-phase current limit tests with phase B yielded textbook results for the current and voltage shapes; however, the current amplitudes were too high. The results from this test are shown in Figure 84. A single-phase ac circuit breaker test with phase C yielded again textbook results of the current and voltage shapes, but the current amplitudes were once more too high.

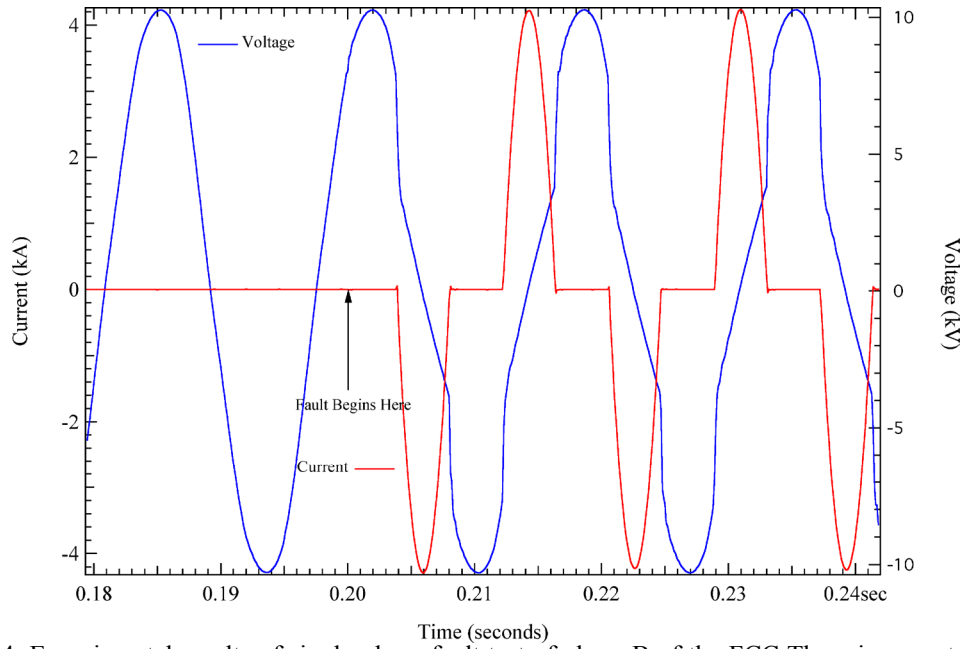


Figure 84. Experimental results of single-phase fault test of phase B of the FCC There is zero steady state current before the fault, which occurs at 0.2 s. The peak measured current, $i_{peak\ meas}$, during the fault was 4.28 kA.

The results of the test of phase B, shown in Figure 84, can be analyzed as follows using the circuit shown schematically in Figure 85 and the simplified circuit of Figure 86. The current is given as $i = \frac{V_{peak}}{\omega L} \left[\sin\left(\omega t - \frac{\pi}{2}\right) - \sin\left(\alpha - \frac{\pi}{2}\right) \right]$, where

$V_{peak} = \frac{12.5}{\sqrt{3}} \sqrt{2} \text{ kV} = 10.2 \text{ kV}$ is the peak voltage, and α is the phase angle between the current and the voltage (Figure 87), deduced as 137° from the experimental results shown in Figure 84.

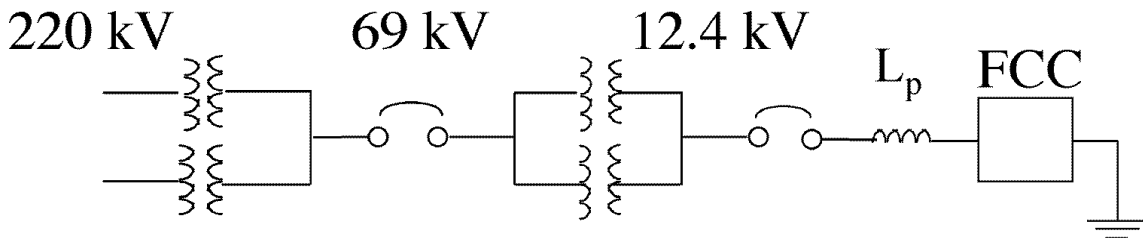


Figure 85. Schematic circuit for the test setup at Southern California Edison.

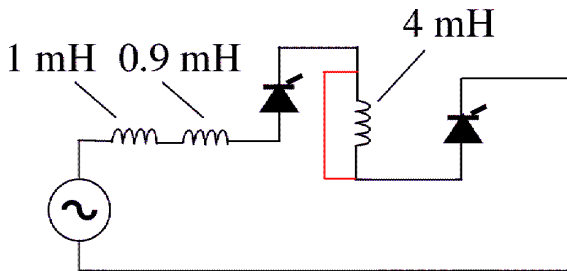


Figure 86. Simplified circuit diagram of the FCC during the test. The HTS coil is noted as 4 mH.

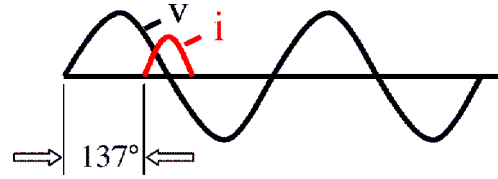


Figure 87. Phase angle between current and voltage during the FCC test.

With the HTS coil in the circuit, $\alpha = 137^\circ$ and $L = 5.9$ mH, the maximum current can be calculated at $i_{peak} = 1.22$ kA. However, if the coil is *not* in the circuit (indicated by the line shorting the coil in Figure 86) during the fault, then $L = 1.9$ mH, and the maximum calculated current would be much higher at $i_{peak} = 3.8$ kA. As this latter value is very close to the measured value of 4.28 kA, the conclusion is that the HTS coil was not in the circuit during the testing of the FCC, and that some kind of internal fault had occurred.

The next stage in the program was to determine the scope of the problem. LANL and DOE on a step by step approach to restore the FCC with cost effectiveness reviews. The industrial partners, notably IGC-SuperPower, expressed interest in the project. The restoration and testing were done at the LANL 13.4 kV NHMFL substation and with support of General Atomic personnel.

As the first step in the restoration project, all three HTS coil vessels were removed from the FCC trailer and moved to the NHMFL power supply building. All three vessels were opened and inspected. The vessel for phase A had no visual damage; the cryogenics in this vessel were known to have a helium leak at low temperatures. The vessels for phases B and C had burn marks around the high voltage (HV) bus and the low voltage superinsulation. A photograph of the damaged region is shown in Figure 88a. Figure 88b shows a schematic of that region. Arcing also occurred from the bus to the vacuum vessel with the location of the flashover the same for both phases. There was no apparent damage to the HTS coils and no voltage breakdown across the aluminum nitride component, originally thought to be a weak point of the HV design and a likely location for a HV breakdown.



Figure 88a. Damaged multilayer insulation near the high voltage bus at the top of the vacuum vessel. The damage was a result of an HV flashover from the HV bus to grounded parts of and in the vessel.

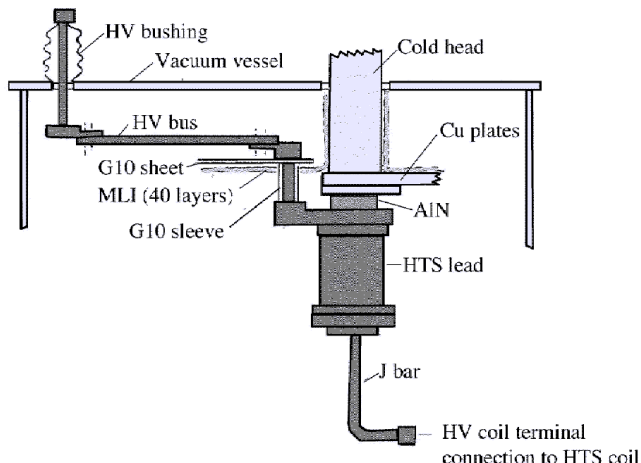


Figure 88b. Schematic of HV bus, the cold head, MLI, AIN insulator and other components near the top of the vacuum vessel in the region where the HV flashover occurred. The vessel top plate is about 5' (about 150 cm) in diameter.

To examine the issue of HV breakdown in the coil vessel, a panel of HV experts from around the US was assembled to examine the experimental findings and identify potential failure mechanisms. These suggestions ultimately led to a series of HV bus improvements. Some of the more obvious causes of voltage flashover are field enhancement by sharp corners and the presence of dirt particles. Some less obvious causes are voltage doubling by resonance, local gas cloud from ice evaporation, MLI evaporation from arcing, and reduction of breakdown voltage in a magnetic field.

Voltage doubling across the HTS coil may occur because of resonance between the source reactance and the coil stray impedance (Figure 89a). The remedy is to attach a low inductance capacitive snubber across the coil terminals to avoid the voltage doubling. Proper sizing of the snubber and minimization of the lead inductance is important to prevent resonances. It is planned also to look for any fast voltage transients, such as were seen (Figure 89b) in a similar circuit, in follow on experiments.

Stray capacitance across the source inductor (Figure 89a) results in fast charging currents in the circuit, including the high voltage bus. Current amplitudes might exceed 50 to 100 kA according to simulations, although the length of time this current flows is very short, in the nanosecond range. During the time these very large currents flow, ice that may be condensed on the HV bus will evaporate, which raises the pressure locally, and decreases the breakdown voltage. The remedy is to replace the conductor with Litz wire and to thermally insulate the surface of the bus conductor to reduce surface current effects. Litz wire is composed of many fine insulated transposed filaments, which all have equal inductance, and therefore current is uniform throughout the wire volume. This is in contrast to a single solid wire, which would have high frequency current flowing almost entirely at the surface thus generating an undesirable heat spike under these conditions.

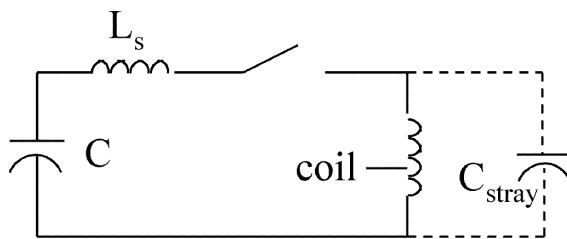


Figure 89a. Schematic of coil circuit leading to resonance and voltage doubling on the coil as a source of possible HV breakdown.

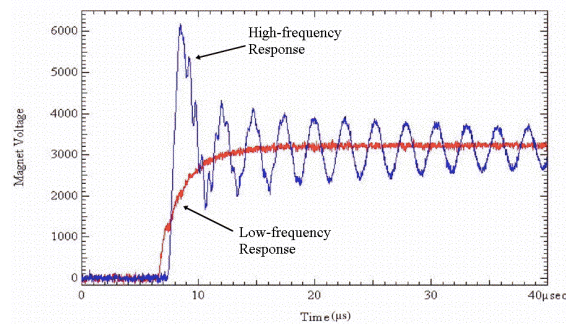


Figure 89b. Voltage transients measured in a circuit similar to that in the FCC to illustrate the phenomenon of voltage doubling.

Another possible source of HV breakdown is the local gas cloud that would result from vaporization of unconstrained MLI. The presence of a strong electric field near the bus can result in physical displacement (motion) of loose MLI. An arc to such unconstrained MLI near where the bus penetrates it will vaporize material. The local gas cloud that develops lowers the discharge strength (Figure 90a) required to initiate the arc. For instance, vaporization of 30 cm² of MLI will raise the vessel pressure to 10⁻⁴ torr with locally much higher pressure.

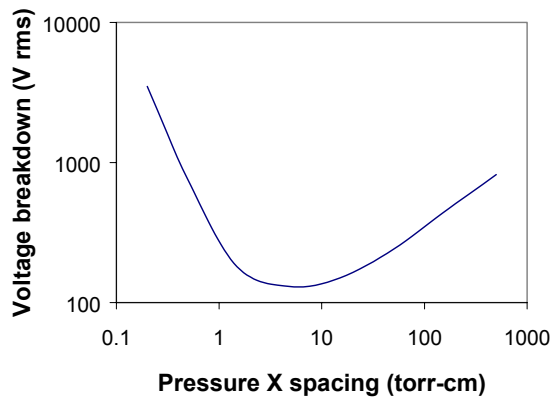


Figure 90a. The Paschen curve for voltage breakdown as a function of pressure times spacing. The FCC typical condition is 10^{-6} torr x 5 cm.

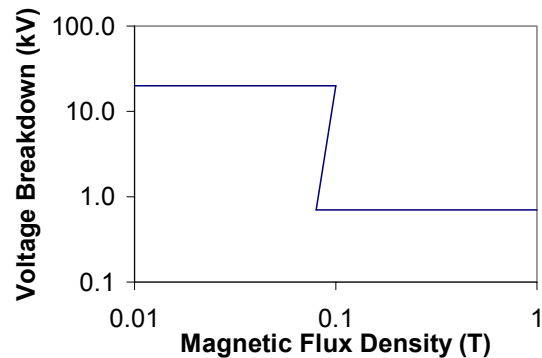


Figure 90b. Dependence of breakdown voltage on magnetic field strength at 10^{-6} torr.

The self-field of the current in the HV bus can also influence the breakdown voltage. This occurs because the magnetic field causes the ionized particles in the gas to have a helical motion. There is a dramatic drop ($\sim X20$) in the breakdown voltage when the diameter of the circular motion is less than the mean free path in the gas. For the FCC bus design and operating pressure, this occurs at a current of about 20 kA. This mechanism could also be a contributing factor for the HV breakdown observed.

As a result of conducting the failure analysis discussed above, a number of plausible failure mechanisms were identified. These mechanisms illustrate the need to modify the design of the HV bus. As a result, a design that addresses all of the issues identified has been developed. All of the existing technology was reviewed to support the new design. Several activities were initiated to optimize the bus performance. These included high pot testing of the bus in air, testing of Litz wire (thermal cycling of epoxy-potted bend regions), improvements in the bushing design, surface breakdown measurements of the AlN insulator at Texas Tech University, and electric field simulations.

The old bus and the new bus design are shown in Figure 91. Immediately apparent is the change from sharp edges and protruding bolt heads to a much more streamlined, round design that limits regions of locally high electric field. The bus will be made of Litz wire (a fine wire, multi-strand, individually insulated, copper cable) inside a stainless steel (SS) tube (used for structural support and to eliminate sharp corners) wrapped with multiple layers of dielectric to a thickness of about 1-2 mm. A conducting ground sheath is then applied as the final layer to the tube. The dielectric wrap with the ground sheath confines the electric field to the region between the stainless tube and the ground sheath. The new HV bus design addresses all the potential failure mechanisms, because the electric field is confined to the region between the ground sheath and the SS tube to prevent arcing, and the Litz wire greatly reduces the surface joule heating.

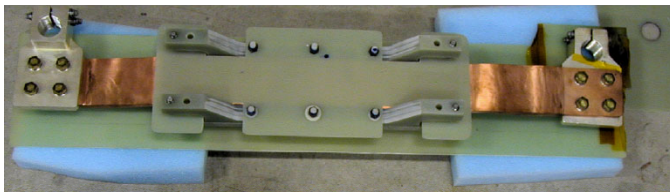


Figure 91a. Photograph of the of the original high voltage bus.

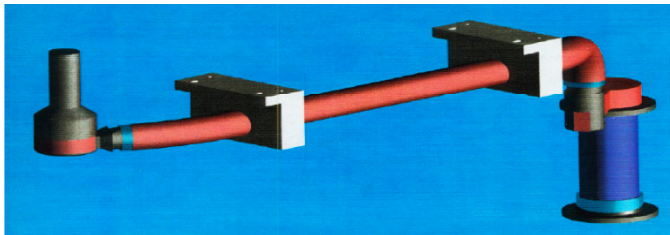


Figure 91b. Conceptual design for the new bus.

As stated earlier, the AlN thermal conductor/electrical insulator was thought to be a weak point in the design and susceptible to HV breakdown. To address this issue, LANL initiated a contract with Texas Tech University to measure the flashover voltage on an AlN disk at temperatures of 40, 60 and 80 K, for pressures of 10^{-6} , 10^{-5} , and 10^{-4} torr. Tests will also be made on disks with modified geometry to attempt to raise the breakdown voltage. The Texas Tech system is shown in Figure 92a. Finite element electrostatics analysis (Figure 92b) will also be used to look for possible high field regions in the vicinity of the AlN insulator.

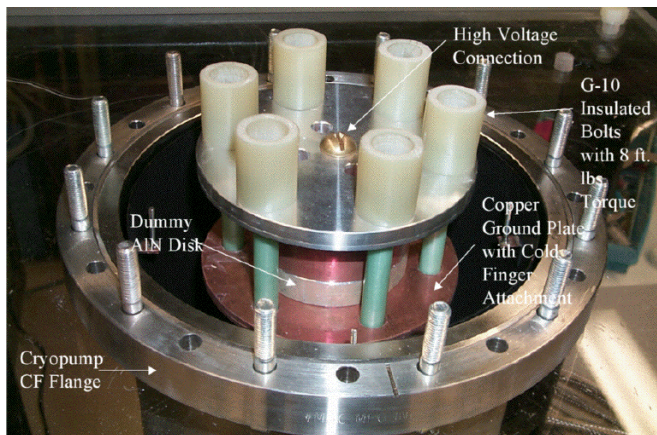


Figure 92a. Test assembly used for flashover tests of the AlN disk as a function of temperature and pressure spanning the expected operating region of the FCC coil vessel.

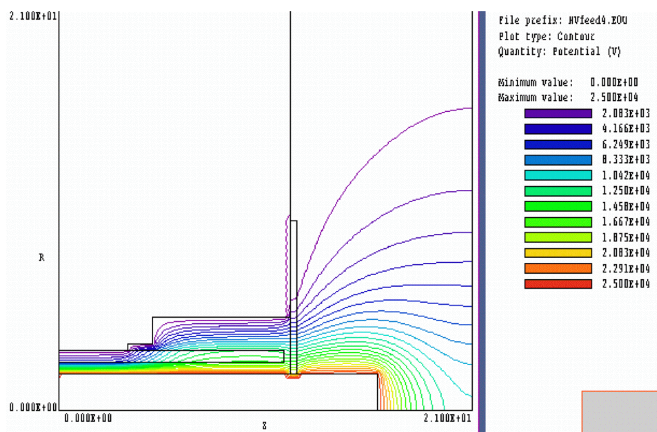


Figure 92b Finite element electrostatics analysis evaluating possible high field regions near the HV penetration of the coil vessel lid.

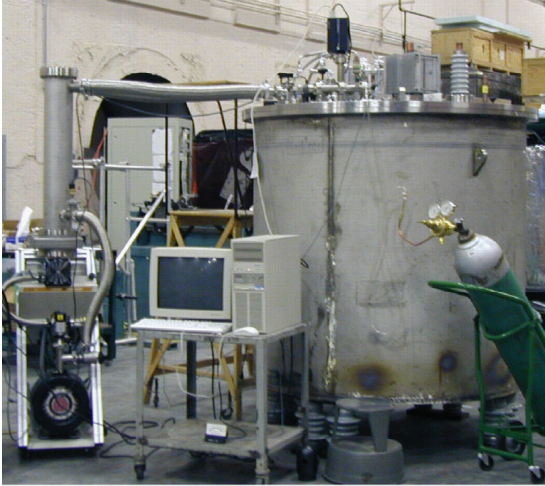


Figure 93. Testing of vacuum and residual gas analysis of FCC coil vessel.

In addition to the electrical issues discussed above, there are also some issues regarding the vacuum and cryogenics systems that need to be addressed in the restoration of the FCC. There was a cold He leak in one vessel, and in the others, after arcing, high residual pressure. The goal during operation is to have no external pumping, and instead to rely on cryopumping by cold surfaces in the vessel. The requirement was for the operating pressure to remain less than 5×10^{-5} torr. To characterize the system more fully, it is necessary to determine using a residual gas analyzer (Figure 93) the long-term (after many hours of pumping and operation) gas species and the leak rates. It is also necessary to determine the amount and type of adsorbants.

In addition, there had been problems with the cryocoolers during the original substation tests in California. There were 10 documented failures of the cryocoolers, likely related to overheating of the compressors, and general problems with He contamination. To address these, Cryomech, the cryocooler manufacturer, was consulted, and improvements were made to the compressor ventilation.

A series of tests are planned at Los Alamos as part of the restoration program. In the early stages, these will be concurrent. There will be a series of tests of the power electronics at the substation using a copper coil replacement for the HTS coil. As the new HV bus design is implemented there will be a series of tests of its components. The vacuum system residual gas analysis tests will be performed. Once the HV bus is installed in the vessel, there will be a series of capacitor bank tests of the HTS coil to rated voltage and current. The test series will end with single-phase and three-phase testing of the FCC on the LANL substation. The tentative schedule for this project is given in Table I.

Table I. Schedule for Restoration of the Fault Current Controller

Date	Task
Sept-Oct 2001	single-phase copper coil substation tests with all three phases
Aug-Oct 2001	high voltage bus tests
Nov 2001	capacitor bank test with first repaired HTS unit
Dec 2001	single-phase substation test with first repaired HTS FCC unit, load and short circuit test
Feb-March 2002	single-phase substation tests with remaining two HTS FCC units
April-May 2002	three-phase, FCC system load and short-circuit substation tests

As a final summary of the work done on the fault current limiter restoration project this year, the following tasks have been accomplished:

1. The HTS coils from the previous substation tests were found to be undamaged.
2. The electrical failure mechanisms were identified using the results from the committee of high voltage experts.
3. The FCC repair was shown to be feasible and a restoration program plan was developed.
4. A new high voltage bus has been designed.
5. Testing of voltage breakdown of key component (AIN) has been initiated at Texas Tech University.
6. The laboratory site for component and system testing was selected at the NHMFL.
7. Some components for the substation tests have been specified and ordered.
8. Performance issues of the cryogenic and vacuum systems have been identified and test plans developed.

3. Fiscal Year 2001 Publications

3.1. Journal Articles Published

- “Interlayer Tunneling of Quasiparticles and Cooper Pairs in Bi-2212 Single Crystal Whiskers,”
Y.I. Latyshev, V.N. Pavlenko, S.-J. Kim, T. Yamashita, L.N. Bulaevskii, M.J. Graf, A.V. Balatsky, N. Morozov, and M.P. Maley,
Physica C **341-348**, 1499 (2000).
- “C-Axis Tunneling in $\text{Bi}_2\text{Sr}_2\text{CaCu}_2\text{O}_8$ in Magnetic Fields up to 60 T,”
N. Morozov, L. Krusin-Elbaum, T. Shibauchi, L.N. Bulaevskii, M.P. Maley, Y.I. Latyshev, and T. Yamashita,
Physica C **341-348**, 1511 (2000).
- “Development of Meter-Long YBCO Coated Conductors Produced by Ion Beam Assisted Deposition and Pulsed Laser Deposition,”
S.R. Foltyn, P.N. Arendt, R.F. DePaula, P.C. Dowden, J.Y. Coulter, J.R. Groves, L.N. Haussamen, L.P. Winston, Q.X. Jia, and M.P. Maley,
Physica C **341-348**, 2305 (2000).
- “Magnetic Imaging of Superconducting Tapes to Determine Current Flow,”
G.W. Brown, M.E. Hawley, D.J. Brown, and F.M. Mueller,
Physica C **341-348**, 2497 (2000).
- “A Comparison of [001] Low-Angle Tilt Grain Boundaries of (100) and (110) Grain Boundary Planes in $\text{YBa}_2\text{Cu}_3\text{O}_{7-d}$ Coated Conductors,”
H. Kung, J. P. Hirth, S. R. Foltyn, P. N. Arendt, Q.X. Jia, M. P. Maley,
Physica C **357-360**, 959 (2001).
- “Josephson Coupling, Phase Correlations, and Josephson Plasma Resonance in Vortex Liquid Phase,”
A.E. Koshelev, L.N. Bulaevskii, and M.P. Maley,
Phys. Rev. B **62**, 14403 (2000).
- “Quasiparticle and Cooper Pair Tunneling in the Vortex State of $\text{Bi}_2\text{Sr}_2\text{CaCu}_2\text{O}_{8+\delta}$,”
N. Morozov, L.N. Bulaevskii, M.P. Maley, Y.I. Latyshev, and T. Yamashita,
Phys. Rev. B **62**, R14681 (2000).
- “Dissociation of Grain Boundary Dislocations in $\text{YBa}_2\text{Cu}_3\text{O}_{7-8}$ Superconducting Thick Films,”
H. Kung, J.P. Hirth, S.R. Foltyn, P.N. Arendt, Q.X. Jia, and M.P. Maley,
Phil. Mag. Lett. **81**, 85 (2001).

- “Multiphase AC Loss Mechanisms in Prototype Multistrand Conductors,”
J.O. Willis, D.E. Daney, M.P. Maley, H.J. Boenig, R. Mele, G. Colletta, M. Nassi,
and J.R. Clem,
IEEE Trans. Appl. Superconduct. **11**, 2188 (2001).
- “Texture Development in IBAD MgO Films as a Function of Deposition Thickness and
Rate,”
J.R. Groves, P.N. Arendt, H. Kung, S.R. Foltyn, R.F. DePaula, L.A. Emmert, and J.G.
Stover,
IEEE Trans. Appl. Superconduct. **11**, 2822 (2001).
- “Investigation of the Initial Stages of Processing Bi-2223 Multifilamentary Tapes by
Analytical Electron Microscopy,”
T.G. Holesinger, A. Ayala, R.M. Baurceanu, and V.A. Maroni,
IEEE Trans. Appl. Superconduct. **11**, 2991 (2001).
- “Properties of a Prototype Bi-Based HTS Composite with a High Resistivity Sheath for
Resistive Fault Current Limiting Applications,”
R.C. Diehl, S. Fleshler, R. Mason, C. Christopherson, K. DeMoranville, R. Harnois,
A. Otto, G.N. Riley, Jr., E. Serres, J.O. Willis, H.J. Boenig, and J.B. Schillig,
IEEE Trans. Appl. Superconduct. **11**, 3265 (2001).
- “Non-Magnetic Substrates for Low Cost YBCO Coated Conductors,”
C.L.H. Thieme, S. Annavarapu, W. Zhang, V. Prunier, L. Fritzemeier, Q. Li, U.
Schoop, M.W. Rupich, M. Gopal, S.R. Foltyn, and T. Holesinger,
IEEE Trans. Appl. Superconduct. **11**, 3329 (2001).
- “A Comparison of Buffer Layer Architectures on Continuously Processed YBCO Coated
Conductors Based on the IBAD YSZ Process,”
T.G. Holesinger, S.R. Foltyn, P.N. Arendt, Q. Jia, P.C. Dowden, R.F. DePaula, and
J.R. Groves,
IEEE Trans. Appl. Superconduct. **11**, 3359 (2001).
- “*In Situ* High Rate Growth of High Temperature Superconductor Tapes,”
L.S.-J. Peng, W. Wang, W. Jo, T. Ohnishi, A.F. Marshall, R.H. Hammond, M.R.
Beasley, E.J. Peterson, and R.E. Ericson,
IEEE Trans. Appl. Superconduct. **11**, 3375 (2001).
- “High-Current Y-Ba-Cu-O Coated Conductor Using Metal Organic Chemical-Vapor
Deposition and Ion-Beam-Assisted Deposition,”
V. Selvamanickam, G. Carota, M. Funk, N. Vo, P. Haldar, U. Balachandran, M.
Chudzik, P. Arendt, J.R. Groves, R. DePaula, and B. Newnam,
IEEE Trans. Appl. Superconduct. **11**, 3379 (2001).
- “Transverse Stress and Fatigue Effects in Y-Ba-Cu-O Coated IBAD Tapes,”
J.W. Ekin, S.L. Bray, N. Cheggour, C.C. Clickner, S.R. Foltyn, P.N. Arendt, A.A.
Polyanskii, D.C. Larbalestier, and C.N. McCowan,
IEEE Trans. Appl. Superconduct. **11**, 3389 (2001).

- “Effect of Ca-Doping on Grain Boundaries and Superconducting Properties of $\text{YBa}_2\text{Cu}_3\text{O}_{7-\delta}$,”
A.V. Berenov, R. Marriott, S.R. Foltyn, and J.L. MacManus-Driscoll,
IEEE Trans. Appl. Superconduct. **11**, 3780 (2001).
- “Real-Time Spectroscopic Ellipsometry as a Characterization Tool for Oxide Molecular Beam Epitaxy,”
B.J. Gibbons, M.E. Hawley, S.T. McKinstry, and D.G. Schlom,
J. Vacuum Sci. and Tech. A **19**, 56 (2001).
- “C-Axis Josephson Plasma Resonance Observed in $\text{Tl}_2\text{Ba}_2\text{CaCu}_2\text{O}_8$ Superconducting Thin Films by Use of Terahertz Time-Domain Spectroscopy,”
V.K. Thorsmolle, R.D. Averitt, M.P. Maley, L.N. Bulaevskii, C. Helm, and A.J. Taylor,
Optics Lett. **26**, 1292 (2001).
- “Thermodynamic Stability and Kinetics of Y-Ba-Cu-O Film Growth at High Rates in Atomic and Molecular Oxygen,”
W. Jo, L.S.-J. Peng, W. Wang, T. Ohnishi, A.F. Marshall, R.H. Hammond, M.R. Beasley, and E.J. Peterson,
J. Crystal Growth **225**, 183 (2001).
- “RHEED In-Plane Rocking Curve Analysis of Biaxially-Textured Polycrystalline MgO Films on Amorphous Substrates Grown by Ion Beam-Assisted Deposition,”
R.T. Brewer, J.W. Hartman, J.R. Groves, P.N. Arendt, P.C. Yashar, H.A. Atwater,
Appl. Surface Sci. **175**, 691 (2001).
- “Effects of Very Thin Strain Layers on Dielectric Properties of Epitaxial $\text{Ba}_{0.6}\text{Sr}_{0.4}\text{TiO}_3$ Films,”
B.H. Park, E.J. Peterson, X. Zeng, W. Si, X.X. Xi, Q.X. Jia,
Appl. Phys. Lett. **78**, 535 (2001).
- “Microstructure of Epitaxial $\text{La}_{0.7}\text{Ca}_3$ Thin Films Grown on LaAlO_3 and SrTiO_3 ,”
C.J. Lu, Z.L. Wang, C. Kwon, Q.X. Jia,
J. Appl. Phys. **88**, 4032 (2001).
- “YBCO Coated Conductor Current Lead Testing,”
P.E. Blumenfeld, J.Y. Coulter, S.R. Foltyn, D.E. Peterson, F.C. Prenger, E.W. Roth, J.A. Stewart,
Advances in Cryogenic Engineering, Volume 45, pages 1565-1572 (2001).
- “In-situ biaxial texture analysis of MgO films during growth on amorphous substrates by ion-beam-assisted deposition,”
R.T. Brewer, P.N. Arendt, J.R. Groves, H.A. Atwater,
Proceedings of the SPIE - The International Society for Optical Engineering, 2001, vol.4468, p.124-30.

“High Critical Current Density $\text{YBa}_2\text{Cu}_3\text{O}_7$ Thick Films Using IBAD MgO Bi-axially Oriented Template Layers on Nickel-Based Superalloy Substrates,”
J.R. Groves, P.N. Arendt, S.R. Foltyn, Q.X. Jia, T.G. Holesinger, H. Kung, E. J. Peterson, R.F. DePaula, P.C. Dowden, L. Stan, L.A. Emmert,
J. Mater. Res. **15**, 1110 (2001).

3.2. Journal Articles Submitted for Publication

“Observation of the Josephson Plasma Resonance in $\text{Tl}_2\text{Ba}_2\text{CaCu}_2\text{O}_8$ Using THz Spectroscopy,”

V.K. Thorsmølle, L.N. Bulaevskii, and A.J. Taylor,
Submitted to *Ultrafast Phenomena*, (to be publ. by Springer-Verlag).

“Rietveld Refinement of Crystal Chemistry of $\text{RBa}_4\text{Cu}_3\text{O}_{8.5+\delta}$ (R=Rare Earth),”

Y.T. Zhu, Li Shu, E.J. Peterson, D.E. Peterson, and F.M. Mueller,
Submitted to *J. Physics and Chemistry of Solids*.

“Dielectric Nonlinearity and Stochastic Effects in Strontium Titanate,”

A.T. Findikoglu, G.D. Lythe, Q.X. Jia, R.A. Camassa.
Submitted to *Applied Physics Letters*.

“Determination of the Activation Energy of Activated Oxygen Diffusion in YBCO Thin Films By Real-Time Spectroscopic Ellipsometry,

B. J. Gibbons, C.B. Eom and R.A. Eao, S. Troler-McKinstry and D.G. Schlom,
Submitted to Journal of Applied Physics.

“Conductive Metal Oxide Thin Films,”

Q.X. Jia,
Book chapter for “Thin Film Handbook” to be published by Academic Press.

“Enhancing the Critical Current of *ex situ* YBCO Coated Conductors,

R. Feenstra, B.W. Kang, A. Goyal, M. Paranthaman, D.F. Lee, P.M. Martin, D.K. Christen, D.M. Kroeger, Paul N. Arendt, J.R. Groves, R.F. DePaula,
full paper submitted to the ORNL Annual Report.

“IBAD Template Films for HTS Coated Conductors,”

Paul N. Arendt,
Book Chapter for “Next Generation High Temperature Superconducting Wires,”
Plenum Press.

“Oxidation of c-Axis Oriented Epitaxial) $\text{YBa}_2\text{Cu}_3\text{O}_{7-x}$ Thin Films in Ozone-Containing Atmospheres,”

B.J. Gibbons, C.B. Eom, R.A. Rao, S. Troler-McKinstry, D.G. Schlom,
Submitted to the *J. Mater. Research*.

“Dielectric Properties of $\text{Ba}_{0.6}\text{Sr}_{0.4}\text{TiO}_3$ Thin Films with Various States,” B.H. Park, E.J.

Peterson, J. Lee, X. Zeng, W. Si, X.X. Xi, Q.X. Jia,
ISIF (International Symposium on Integrated Ferroelectrics, Colorado Springs, CO, March 11-14, 2001; Published in *Integrated Ferroelectrics* **39**, 271 (2001).

Ion-Beam Assisted Deposition of MgO with *in situ* RHEED Monitoring to Control Biaxial Texture,”

J.R. Groves, P.N. Arendt, S.R. Foltyn, Q.X. Jia, R.F. DePaula, P.C. Dowden, H. Kung, T.G. Holesinger, L. Stan, L.A. Emmert, E.J. Peterson,
Paper submitted to appear in MRS Symposium Proceedings, Transport and Microstructural Phenomena in Oxide Electronics, Spring MRS, 2001, 4/15-20/01. San Francisco, CA.

“Integration of Biaxially Aligned Conducting Oxides with Silicon Using Ion Beam Assisted Deposited MgO Templates,”

L.A. Emmert, B.H. Park, J.R. Groves, R.F. DePaula, Q.X. Jia, P.N. Arendt,
Full paper submitted for proceedings of the 2001 MRS Spring Meeting, San Francisco, CA, 4/14-22/01.

“In-Situ Biaxial Texture Analysis of MgO Films during Growth on Amorphous Substrates by Ion Beam-Assisted Deposition,”

R.T. Brewer, P.N. Arendt, J.R. Groves, H.A. Atwater,
Full paper submitted to the MRS Symposium Proceedings Vol. 672 from Spring MRS talk #06.2, May 16-20, 2001, San Francisco.

“High-Resolution Transmission Electron Microscopic Study of Defects and Interfaces in Epitaxial TiO₂ Films on Sapphire and LaAlO₃,”

J.Y. Huang, B.H. Park, D. Jan, X.Q. Pan, Y.T. Zhu, Q.X. Jia,
Submitted to *Phil. Mag. A*.

“Dielectric Properties of Ba_{0.6}Sr_{0.4}TiO₃ Thin Films With Various Strain States,”

B.H. Park, E.J. Peterson, J. Lee, X. Zeng, W. Si, X.X. Xi, Q.X. Jia
Full paper submitted to journal, Integrated Ferroelectrics.

“Structure, Processing and Property Relationships in Tunable RF and Microwave Devices,”

B.J. Gibbons, B.H. Park, Y. Gim, Y. Fan, A.T. Findikoglu, D. Reagor, Q.X. Jia,
Full Paper submitted to journal Integrated Ferroelectrics.

“Imaging Transport Current Distribution in High Temperature Superconductors using Room Temperature Scanning Laser Microscope,”

B.E. Klein, S. Seo, C. Kwon, B.H. Park, Q.X. Jia,
full paper submitted *Applied Physics Letters*.

“Josephson Plasma Resonance in Tl₂Ba₂CaCu₂O₈ in a Magnetic Field Measured Using THz Spectroscopy,”

V.K. Thorsmolle, R.D. Averitt, M.P. Maley, L.N. Bulaevskii, C. Helm, A. Taylor,
Paper for Strongly Correlated Electron Systems Conference, Ann Arbor, MI, August 6-10, 2001; to appear in *Physica B*.

- “Enhanced Critical Currents in Bi-2223/Ag Sheathed Tapes by High Energy Proton Irradiation,”
J.O. Willis, J.Y. Coulter, M.P. Maley, J.L. Ullmann, S. Fleshler, G.N. Riley Jr.,
Paper submitted to the International Cryogenics Materials Conference proceedings
(Advances in Cryogenic Engineering (Materials)), eds. U. Balachandran et al.,
American Institute of Physics.
- “Microstructural Development in YBa₂Cu₃O₇ Coated Conductors Based on Ion-Beam-Assisted Deposition (IBAD) of YSZ and MgO Buffer Layers,”
T.G. Holesinger, S.R. Foltyn, P.N. Arendt, Q.X. Jia, J.R. Groves,
Ibid.
- “The Development of the Superconducting Phase and the Origin of Potential Current Limiting Defects in Bi-2223 Tapes,”
T.G. Holesinger, J.F. Bingert, R.D. Parrella, G.N. Riley Jr.,
Ibid.
- “High Temperature Superconducting Magnetic Refrigeration,”
P.E. Blumenfeld, F.C. Prenger, A. Sternberg, C. Zimm,
Paper submitted to the Cryogenic Engineering Conference proceedings (Advances in Cryogenic Engineering), eds. S. Breon et al., American Institute of Physics.
- “Improving Flux Pinning in MgB₂ Superconductor Through Coherent Precipitation,”
X. Liao, A.C. Serquis, Y.T. Zhu, J. Huang, J.O. Willis, D.E. Peterson, F.M. Mueller,
Paper submitted to *Applied Physics Letters*.
- “Effect of Lattice Strain and Defects on the Superconductivity of MgB₂,”
A.C. Serquis, Y.T. Zhu, E.J. Peterson, J.Y. Coulter, D.E. Peterson, F.M. Mueller,
Paper submitted to *Applied Physics Letters*.
- “High Temperature Superconducting Thick Films with Enhanced Supercurrent Carrying Capability,”
Q.X. Jia, S.R. Foltyn, P.N. Arendt, J.F. Smith,
Paper submitted to *Applied Physics Letters*.
- “Magnetic Imaging of Superconducting Tapes to Determine Current Flow,”
G. Brown, S.R. Foltyn, F.M. Mueller,
Full paper submitted to the proceedings of the Fall 2000 Meeting of the Materials Research Society, November 27—December 21, 2000.

3.3 Other Publications and Conference Abstracts

“Advances in HTS Coated Conductor Processes and Performance in High Magnetic Fields,”

B. E. Newman,

Abstract for the Low Temperature Superconductor Workshop (LTSW 2000), Santa Rosa, California, November 8-10, 2000.

“Growth of Thick YBCO Films With High Critical Current Density by Pulsed Laser Deposition,”

S.R. Foltyn, Q.X. Jia, P.N. Arendt, T.G. Holesinger, H. Kung, J.F. Smith,

Abstract for the MRS Fall 2000 Meeting, November 27-December 1, 2000, Boston, MA.

“Magnetic Imaging of Superconducting Tapes to Determine Current Flow,”

G.W. Brown, M.E. Hawley, F.M. Mueller, D.J. Brown,

Ibid.

“Improved Inversion Techniques for Obtaining Transport Current Pathways from Magnetic Field Data,”

F.M. Mueller, D.J. Brown, G. W. Brown, M.E. Hawley,

Ibid.

“Neutron Diffraction Analysis of (Y, Re) Ba₂Cu₃O_{7-x} (Re=Yb, Er, Ho, Dy),”

E.J. Peterson, W.H. Hults, M. Simpson, L. Kinder, J. Y. Coulter, S.R. Foltyn,

Abstract submitted to the 2nd HIPPOS Neutron Diffractometer User Workshop for Materials and Earth Sciences, Santa Fe, NM, February 28-1 March, 2001.

“Status of YBCO Coated Conductor Development in the U.S.,”

Jeffrey O. Willis,

Abstract for the Workshop on Large-Scale Applications of High-T_c Superconductors, Tokyo, JAPAN, March 5, 2001.

“Texturing of Thin Films Using Ion Beams,”

P.N. Arendt, L. Emmert, T.G. Holesinger, Q.X. Jia, H. Kung, R.F. DePaula, P.C.

Dowden,

Abstract submitted to the March Meeting of the American Physical Society, March 12-16, 2001, Seattle, WA.

“Determining Transport Current Density Pathways in YBCO Thin Films by Low

Temperature Scanning Magnetoresistance Microscopy,” G.W. Brown, M.E. Hawley,

P.O. Dickerson, D.J. Brown, S.R. Foltyn, F.M. Mueller,

Ibid.

- “Josephson Plasma Resonance Observed in $\text{Ti}_2\text{Ba}_2\text{CaCu}_2\text{O}_8$ Superconducting Thin Films Using Terahertz Time-Domain Spectroscopy,”
V. K. Thorsmolle, R. D. Averitt, M.P. Maley, A.J. Taylor, L.N. Bulaevskii, C. Helm,
Ibid.
- “Structure, Processing, and Property Relationships in Tunable RF and Microwave Devices,”
Brady J. Gibbons, B.H. Park, Y. Gim, A.T. Findikoglu, D.W. Reagor,
Abstract for the 13th International Symposium, Colorado Springs, CO, March 9-14, 2001.
- “Integration of Biaxially Aligned SrRuO_3 and Sr_2RuO_4 with Silicon Using an IBAD-MgO Intermediate Layer,”
L.A. Emmert, B.H. Park, J. R. Groves, R.F. DePaula, Q.X. Jia, P.N. Arendt,
Abstract for the MRS Spring meeting, April 16-20, 2001, San Francisco, CA.
- “Ion-Beam Assisted Deposition of MgO with In-situ RHEED Monitoring to Control Biaxial Texture,”
J R. Groves, P. N. Arendt, S. R. Foltyn, Q.X. Jia, R. Depaula, P. C. Dowden, H. Kung, T. G. Holesinger, L. Stan, L. A. Emmert, E. J. Peterson,
Ibid.
- “Optimization of Dielectric and Structural Properties of $\text{Ba}_{1-x}\text{Sr}_x\text{TiO}_3$ Films for Tunable Microwave Devices,”
Q.X. Jia, B.H. Park, B.J. Gibbons, Y. Gim, A.T. Findikoglu, Y. Fan, P. Lu, G. Wang, X.D. Xiang,
Ibid.
- “Large Paramagnetic Meissner Effect in MgB_2 ,”
Adriana Serquis, Yuntian Zhu, Yates Coulter, Fred Mueller,
Ibid.
- “Bi-2223: Prospects for Further Developments in Critical Current Performance,”
X. Cai, J. Chandler, M. Feldmann, E. Hellstrom, J. Jiang, D. Larbalestier, S. Patnaik, A. Polyanskii, M. Rikel, Y. Yuan, Y. Dingan, Y. Huang, Q. Li, K. de Moranville, R. Parella, G. Riley, M. Rupich, V. Maroni, T.G. Holesinger, and John Bingert,
Ibid.
- “Nonequilibrium Conductivity Dynamics in $\text{YBa}_2\text{Cu}_3\text{O}_{7-x}$,”
R. D. Averitt, A. Taylor, V. K. Thorsmolle, Q.X. Jia, S. A. Trugman,
Abstract for Quantum Electronics and Laser Science '01 Baltimore, MD, May 6-11, 2001.
- “Effect of Texture on the Electrical Properties of $\text{La}_{0.5}\text{Sr}_{0.5}\text{CoO}_3$ Thin Films,”
L.A. Emmert, B.H. Park, J.R. Groves, R.F. DePaula, L. Stan, Q.X. Jia, P.N. Arendt,
Abstract for the American Vacuum Society Meeting, Albuquerque, NM, May 23-24, 2001.

- “Materials for the Optimization of Barium Strontium Titanate Thin Film Ferroelectric-based Tunable Microwave Devices,”
Q.X. Jia, B.H. Park, B.J. Gibbons, P. Lu, F.W. Van Keuls, F.A. Miranda,
Abstract for the Ferroelectric Workshop in Puerto Rico, June 1-2, 2001.
- “High Temperature Superconducting Coated Tape and Their Performance in High Magnetic Fields,”
B. Newnam,
Abstract for the Free Electron Laser Development for Naval Applications Meeting, Newport News, VA, June 5-6, 2001.
- “The Application of High Temperature Superconductors to Underground Communications,”
D. Reagor,
Abstract for the OIT Sensors and Controls Workshop, June 6-8, 2001, New Orleans, LA.
- “The Application of High Temperature Superconductors to Underground Communications,”
D. Reagor,
Abstract for the DOE workshop on Sensors and Controls, June 7, 2001, Washington, DC.
- “Microstructural Characterization of YBCO Thick Film Coated Conductors on IBAD-YSZ and MgO Template Layers,”
H. Kung, T.G. Holesinger, S.R. Foltyn, P.N. Arendt, Q.X. Jia, J.R. Groves, M.P. Maley,
Extended abstract for the 5th joint ISTE/C/MRS Workshop on HTS Conductors, June 25-27, 2001, Honolulu, HI.
- “High-Ic YBCO Coated Conductors Produced by an ex situ BaF₂ Process,”
R. Feenstra, A. Goyal, M. Paranthaman, D.F. Lee, P.M. Martin, D.K. Christen, D.M. Kroeger, P.N. Arendt, J.R. Groves, R.F. DePaula,
Ibid.
- “Microstructural Characterization of YBCO Thick Film Coated Conductors on IBAD-YSZ and MgO Template Layers,”
H. Kung, S.R. Foltyn, P.N. Arendt, J.R. Groves, T. G. Holesinger, Q.X. Jia, M.P. Maley,
Ibid.
- “Development of the IBAD MgO Process for HTS Coated Conductors,”
J.R. Groves, P.N. Arendt, S.R. Foltyn, Q.X. Jia, T.G. Holesinger, H. Kung, R.F. DePaula, P.C. Dowden, E.J. Peterson, L. Stan, L.A. Emmert,
Ibid.

- “Acceptor Doping of YBCO Grain Boundaries,”
A.V. Berenov, C. Farvacque, D. MacPhail, S.R. Foltyn, J.L. MacManus-Driscoll,
Ibid.
- “Microstructural Development in YBa₂Cu₃O₇ Coated Conductors Based on Ion-Beam-Assisted Deposition (IBAD) of YSZ and MgO Buffer Layers,”
T.G. Holesinger, S.R. Foltyn, P.N. Arendt, Q.X. Jia, J.R. Groves,
Ibid.
- “The Development of the Superconducting Phase and the Origin of Potential Current Limiting Defects in Bi-2223 Tapes,”
T.G. Holesinger, J.F. Bingert, R.D. Parrella, G.N. Riley Jr.,
Abstract submitted to the CEC/ICMC 2001, Madison, WI, July 16-20, 2001.
- “Enhanced Critical Currents in Bi-2223/Ag Sheathed Tapes by High Energy Proton Irradiation,”
J.O. Willis, J.Y. Coulter, M.P. Maley, J.L. Ullmann, S. Fleshler and G.N. Riley, Jr.,
Ibid.
- “Recent Progress in Bi-2223 Tape Technology: Improving Performance and Reducing Cost,”
Y.B. Huang, G.N. Riley Jr., A. Otto, M. Teplitsky, R.D. Parrella, X.Y. Cai, D. Larbalestier, T. Holesinger, R.M. Baurceanu, V.A. Maroni,
Ibid.
- “Measurement of Critical Currents on YBCO Coated Conductors: Effects of Sample Contact Conductors: Resistance and Liquid Nitrogen Bath Temperature Control,”
J.Y. Coulter, S.R. Foltyn, P.N. Arendt, P.C. Dowden, R.F. DePaula, J.R. Groves, J.O. Willis, M.P. Maley,
Ibid.
- “Measurement of Critical Current Homogeneity on Long-Length YBCO Conductors in a Magnetic Field,
J.Y. Coulter, S.R. Foltyn, P.N. Arendt, P.C. Dowden, R.F. DePaula, J.R. Groves, J.O. Willis, M.P. Maley,
Ibid.
- “High Temperature Superconducting Magnetic Refrigeration,”
P.E. Blumenfeld, F.C. Prenger, A. Sternberg, C. Zimm,
Ibid.
- “Underground Digital Radio Using High Temperature Superconductor Technology,
J. Vasquez-Dominguez,
Abstract for the Student Symposium 2001, Santa Fe, NM. August 5-6, 2001.
- “Application of Neutron Scattering to Estimate Current Density Distributions in High Temperature Superconducting Tapes,”
O. Ogunnika, F.M. Mueller,
Ibid.

- “Terahertz Time-Domain Spectroscopy of High-Tc Superconductors,”
V.K. Thorsmolle, MST-STC, abstract submitted for a Dissertation.
- “Effects of Microstructure on the Dielectric Properties of $\text{Ba}_{0.6}\text{Sr}_{0.4}\text{TiO}_{0.3}$ Films,”
B.H. Park, K.H. Ahn, A. Saxena, L.A. Emmert, J.R. Groves, P.N. Arendt, Q.X. Jia,
Abstract submitted to the Fall 2001 MRS Meeting, Boston, MA. November 26-30,
2001.
- ”Progress in Coated Conductor Development at Los Alamos National Laboratory,”
S.R. Foltyn, P.N. Arendt, P.C. Dowden, R.F. DePaula, J.R. Groves, L. Stan, T.G.
Holesinger, Q.X. Jia, B.J. Gibbons, V. Matijasevic, J.Y. Coulter, E.J. Peterson,
Ibid.
- “(110)-Oriented Grain Boundaries in $\text{YBa}_2\text{Cu}_3\text{O}_{7-x}$ Based Coated Conductors,”
B.J. Gibbons, H. Kung, Q.X. Jia, R.J. Hammon, A.K. Zurek, S.R. Foltyn,
Ibid.
- “X-Ray Diffraction Mapping of YBCO Superconducting Tape on a Mesostructural
Scale,”
E.J. Peterson, U. Preckwinkle, B.N. Herrington, D.J. Brown, G.W. Brown, M.
Hawley, J.Y. Coulter, S.R. Foltyn, P.N. Arendt, D.E. Peterson
Ibid.
- “Phase Diagram Studies in the $\text{SrO-CuO-Ti}_2\text{O}_3$ System; Applications to YBCO Coated
Conductors,”
A. Ayala, T.G. Holesinger, E.J. Peterson, M. Archuleta,
Ibid.
- “Strong Correlation Between Transport Current Densities and Spatially-Resolved X-Ray
Analysis in YBCO Superconducting Tapes,”
F.M. Mueller, D.J. Brown, G.W. Brown, M. Hawley, J.Y. Coulter, P.N. Arendt, E.J.
Peterson, U. Preckwinkle, B.N. Herrington, D.E. Peterson,
Ibid.
- “The Microstructural Development of the Colony Structure Along the Silver Sheath in
Bi-2223 Tapes,”
T.G. Holesinger, J.F. Bingert, R.D. Parrella, Y. Huang, G.N. Riley,
Ibid.
- “Characterizing Transport Current Defects in 1-cm Wide YBCO Coated Conductors,”
G. Brown, M. Hawley, E.J. Peterson, J.Y. Coulter, P.C. Dowden, P.N. Arendt, S.R.
Foltyn, F.M. Mueller,
Ibid.
- “Engineered Microstructures and Transport Properties in YBCO Coated Conductors,”
T.G. Holesinger, B.J. Gibbons, J.Y. Coulter, S.R. Foltyn,
Ibid.

“Development of In-Plane Texture in Ceramic Thin Films by Ion Beam Assisted Deposition,”

L. Emmert, P. Arendt, J.R. Groves, R. DePaula, L. Stan,

Abstract submitted to the 4th Pacific Rim International Conference on Advanced Materials and Processing (PRICM-4) December 11-15, 2001, Honolulu, HI.

4. Patent and License Activity (April 1988 to Present)

4a. Invention Disclosures and Patent Applications

Designation	Date	Subject	Submitted by
DOE S-82,620 S.N. 08/425,752	Opened 1/06/95 Filed 04/19/95	High-Temperature Superconducting Thick Films	P. Arendt, X.D. Wu, and S. Foltyn
DOE S-82,623 S.N. 08/608,069	Opened 1/06/95 Filed 02/28/96	Melt Processing of Superconductors Using Alumina	T.G. Holesinger
DOE S-89,624 S.N. 08/942,038	Filed 10/1/97	Substrates for Superconductors	L.G. Fritzmeier, E. Thompson, E. Siegel, C. Thieme, R.D. Cameron, J.L. Smith, W.L. Hults
DOE S-89,678 S.N. 09/152,813	Filed 9/14/98	Superconducting Structure	C. Kwon, Q.X. Jia, and S.R. Foltyn
DOE S-89,679 S.N. 60/100,215 S.N.09/787,224	Filed 9/14/98 Filed 3/14/01	Superconducting Structure Including Mixed Rare-Earth Barium Copper Oxide Compositions	C. Kwon, Q.X. Jia, S.R. Foltyn, J.L. Smith, W.L. Hults, E.J. Peterson
DOE S-91,736 S.N. 60/138,326 S.N. 09/615,640	Filed 06/09/99 Filed 7/13/00	High Temperature Superconducting Composite Conductor and Method for Manufacturing the Same	T.G. Holesinger and J.F. Bingert
DOE S-91,761 S.N. 60/213,111 S.N. 09/867,842	Filed 6/21/00 Filed 5/29/01	Architecture for High Critical Current Superconducting Thick Films	Q.X. Jia S.R. Foltyn T.G. Holesinger
DOE S-94,668 S.N. 60/170,968 S.N. 09/616,570	Filed 12/15/99 Filed 7/14/00	Surface Control of Alloy Substrates and Methods of Manufacture Thereof	L.G Fritzmeier, Q. Li, M.W. Rupich, E. Thompson, E. Siegel, C. Thieme, S. Annavurapu, P.N. Arendt, S.R. Foltyn
DOE 94,720	7/13/00	Apparatus for Heating a Moving Tape	S. R. Foltyn, P.C. Dowden
DOE 94,726 S.N. 09/731,534	Filed 12/06/00	High Temperature Superconducting Thick Films	P.N. Arendt, S.R. Foltyn, J.R. Groves, T.G. Holesinger, Q.X. Jia
DOE 94,731 S.N. 09/731,646	Filed 12/06/00	Superconducting Composite Structures	T.G. Holesinger S.R. Foltyn
DOE 94,732 S.N. 09/721,834	Filed 11/22/00	Adjustable Direct Current and Pulsed Fault Current Limiter	H.J. Boenig J.B. Schillig
DOE 94,734 S.N. 60/333,917	Filed 11/21/01	Composition of Matter for Superconducting Composite Conductors and Manufacturing of Same	T.G. Holesinger, S.R. Foltyn, P.N. Arendt, J.R. Groves, Q.X Jia, A. Ayala
DOE S-97,723 S.N. 10/113,476	Filed 5/30/01	High Critical Current Superconducting Tapes	T G. Holesinger, Q.X. Jia S.R. Foltyn

4b. Patents Granted

Designation	Date	Subject	Issued to	Status
DOE S-63,245 S.N. 07/041,950 US Pat.4,784,686	Filed 04/24/87 Issued 11/15/88	Synthesis of Ultrafine Powders by Microwave Heating	T.T. Meek H. Sheinberg R.D. Blake	Expired 05/15/00
DOE S-68,033 S.N. 07/454,607 US Pat. 5,008,622	Filed 12/21/89 Issued 04/16/91	Superconductive Imaging Surface Magnetometer	W.C. Overton, Jr D. van Hulsteyn E.R. Flynn	Expired 10/16/98
DOE S-68,041 S.N. 07/330,329 US Pat 5,006,672	Filed 03/29/89 Issued 04/09/91	Apparatus for Storing High Magnetic Fields Having Reduced Mechanical Forces and Reduced Magnetic Pollution	M.L. Prueitt F.M. Mueller J.L. Smith	Maint. Fee 3 due 10/09/02
DOE S-68,042 S.N. 07/276,188 US Pat 4,873,444	Filed 11/23/88 Issued 10/10/89	Detection of Surface Impurity Phases in HTS Using Thermally Stimulated Luminescence	D.W. Cooke M.S. Jahan	Expired 10/10/97
DOE S-68,086 S.N. 07/311,998 US Pat 4,992,696	Filed 02/17/89 Issued 02/12/91	Apparatus Having Reduced Mechanical Forces for Supporting High Magnetic Fields	M.L. Prueitt F.M. Mueller J.L. Smith	Maint. Fee 3 due 08/12/02
DOE S-68,098 S.N. 07/324,264 US Pat 5,015,952	Filed 03/14/89 Issued 05/14/91	Apparatus for Charac- terizing Conductivity of Materials by Measuring the Effect of Induced Shielding Currents Therein	J.D. Doss	Expired 05/14/99
DOE S-71,082 S.N. 07/671,231 US Pat 5,102,863	Filed 03/19/91 Issued 04/07/92	Process for Producing Clad Superconducting Materials	R.B. Cass K.C. Ott D.E. Peterson	Expired 10/07/99
DOE S-71,084 S.N. 07/670,111 US Pat 5,134,360	Filed 03/15/91 Issued 07/28/92	Apparatus and Method for Critical Current Measurements	J.A. Martin R.C. Dye	Expired 01/28/00
DOE S-72,816 S.N. 07/690,725 US Pat 5,268,646	Filed 04/24/91 Issued 12/07/93	Apparatus & Method for Characterizing Con- ductivity of Materials	J.D. Doss	Maint. Fee 2 due 06/07/01
DOE S-72,851 S.N. 07/860,337 US Pat. 5,238,913	Filed 03/30/92 Issued 08/24/93	Superconducting Micro- circuitry by the Micro- lithographic Patterning of Superconducting Compounds and Related Materials	N.V. Coppa	Maint. Fee 2 due 02/24/01

DOE S-72,861 S.N. 813,726 US Pat 5,262,394	Filed 12/27/91 Issued 11/16/93	Superconductive Compositions Including Cerium Oxide Layer	X.D. Wu R. Muenchausen	Maint. Fee 2 due 05/16/01
DOE S-72,880 S.N. 07/774,748 US Pat 5,278,138	Filed 10/11/91 Issued 01/11/94	Aerosol Chemical Vapor Deposition of Metal Oxide Films	K.C. Ott T.T. Kodas	Maint. Fee 2 due 05/16/01
DOE S-72,898 S.N. 814,355 US Pat 5,252,551	Filed 12/27/91 Issued 10/12/93	Superconductive Articles	X.D. Wu, R.E. Muenchausen	Maint. Fee 2 due 01/11/01
DOE S-72,899 S.N. 813,727 US Pat 5,270,294	Filed 12/27/91 Issued 12/14/93	Free-Standing Superconductive Articles	X.D. Wu, R.E. Muenchausen	Maint. Fee 2 due 06/14/01
DOE S-75,023 S.N. 08/419,485 US. Pat 5,554,224	Filed 03/31/94 Issued 09/10/96	Substrate Heater for Thin Film Deposition	S.R. Foltyn	Maint. Fee 2 due 03/10/04
DOE S-75,081 S.N. 08/067,911 US Pat 5,300,486	Filed 05/27/93 Issued 04/06/94	Synthesis of BiPbSrCaCuO Superconductor	W.L. Hults, K.A Kubat-Martin, K.V. Salazar, D.S. Phillips, D.E. Peterson	Maint. Fee 2 due 10/05/01
DOE S-78,394 S.N. 08/419,485 US Pat. 5,569,641	Filed 04/10/95 Issued 10/29/96	Preparation of Superconducting Bi- 2223 Wire	M.G. Smith J.O. Willis D.E. Peterson	Maint. Fee 2 due 04/29/04
DOE S-80,400 S.N. 08/168,331 US Pat 5,434,128	Filed 12/17/93 Issued 07/18/95	Superconducting Wire	D.A. Korzekwa J.F. Bingert D.E. Peterson H. Sheinberg	Maint. Fee 2 due 01/18/03
DOE S-82,620, S.N. 08/425,752 US Pat. 5,872,080	Filed 04/19/95 Issued 02/16/99	High Temperature Superconducting Thick Films	P.N. Arendt X.D. Wu S.R. Foltyn	Maint. Fee 1 due 08/16/02
DOE S-82,623 S.N. 08/608,069 US Pat. 5,958,842	Filed 02/28/96 Issued 09/28/99	Melt Processing of Superconductors Using Alumina	T.G. Holesinger	Maint. Fee 1 due 03/28/03
DOE S-82,633 US Pat. 5,726,848	Filed 05/8/96 Issued 3/10/98	Fault Current Limiter and Alternating Current Circuit Breaker	H.J. Boenig	Maint. Fee 1 due 09/10/01
DOE S-84,942 S.N. 08/597,061 US Pat. 5,908,812	Filed 02/05/96 Issued 06/01/99	Structure for HTS Composite Conductors & Manufacture of Same	J.D. Cotton G.N. Riley	Maint. Fee 1 due 12/01/02
DOE S-84,965 S.N. 08/865,827 US. Pat.5,820,678	Filed 09/23/96 Issued 10/13/98	Solid Source MOCVD Delivery System	B.N. Hubert X.D. Wu	Maint. Fee 1 due 04/13/02

DOE S-89,600 S.N. 60/074,717 S.N. 09/249,476	Filed 2/13/98 Filed 02/12/99 Issued 3/6/01	Compressive Annealing of BSCCO-2223 Superconductive Tapes	Y.T. Zhu, P.S. Baldonado, J.F. Bingert, T.G. Holesinger, D.E. Peterson	Maint. Fee due 3/06/04
--	---	---	--	---------------------------

4c. Licenses Granted

License Number	Date	Subject	Issued to
89-41-0000-1	12/28/88 (Terminated 11/94)	Apparatus for Characterizing Conductivity of Materials by Measuring the Effect of Induced Shielding Currents Therein	Lakeshore Cryotronics
99-C00510.1	11/11/98	Superconductive Article including Cerium Oxide Layer	DuPont Superconductivity
01-C01080.0	05/29/01	High Temperature Superconductor Material	IGC-SuperPower, LLC
01-C01081.0	05/29/01	High Temperature Superconductor Material	IGC-SuperPower, LLC
01-C01082.0	05/29/01	Fault Current Limiter and Alternating Current Circuit Breaker Device	IGC-SuperPower, LLC

5. Agreements in Progress (11 Active, all types)

5a. Superconductivity Pilot Center Agreements - Active

Organization	Topic	PI	Funding,\$ K DOE	Funding,\$K Partner	Dates
American Superconductor Corporation	Bi-2223 Conductors HTS Composite Conductors	Peterson Peterson Willis Willis Holesinger	170.5 587.1 1500 2300 1800	179 350 950 1100 1800	Ph 1: 6/89- Ph 2: 11/91- Ph 3: 2/94- Ph 4: 3/96- Ph.5: 7/98- 3/01

5b. CRADA Agreements - Active

Organization	Topic	PI	Funding,\$K DOE	Funding,\$K Partner	Dates
Oxford Superconducting Technology	Bi-2212 HTS Tapes	Smith Holesinger Holesinger	290 55 100	290 100 130	11/93 -11/96 10/97-10/98 5/99-9/01
3M Corporation	Coated Conductors	Peterson	960 720 400	1375 720 150	3/97-3/99 3/99-5/00 5/00-1/02
IGC- SuperPower	Coated Conductors	Newnam Balachandran	700, LANL 500, ANL	1300	1/00-3/03

5c. Funds In / Funds Out Agreements - Active

Organization	Topic	PI	Type	Value \$K	Dates
None					

5d. Other Collaborations - Active

Organization	Topic	PI	Dates
ASC/ ANL/ ORNL/ U. Wisconsin/ (previously, NIST-Gaithersburg)	Bi-2223 Wire Development (Wire Development Group)	J. Willis Holesinger	11/91-11/00 11/00-
3M/ORNL/ Southwire / Stanford University	Coated Conductor Group	E. Peterson	3/97-
ASC/ ORNL/ LBNL/U. Wisconsin/ Stanford U./MIT/ Wright-Patterson AFB/ EPRI (previously, TCSUH)	Coated Conductor Development Group	J. Willis Holesinger	2/96- 11/00-
Oak Ridge National Laboratory	HTS Information Exchange	D. Peterson	In Progress
Argonne National Laboratory	HTS Information Exchange	D. Peterson	In Progress
Sandia National Laboratories	HTS Information Exchange	D. Peterson	In Progress
Brookhaven National Laboratory	HTS Information Exchange	D. Peterson	In Progress

6. Completed Agreements

6a. Superconductivity Pilot Center Agreements - Completed

Organization	Topic	PI	Funding,\$K DOE	Funding,\$K Partner	Dates
CPS Superconductor	Metal-Ceramic Interfaces	Mitchell	102.6	80.8	9/89 - 9/90
DuPont / Hewlett-Packard	HTS Electronic Components	Peterson	3777	7200	10/89 - 10/92
Space Industries, Inc.	Microgravity Processing	Peterson	205	247	4/90 - 4/91
Cryopower Associates	Improvement of Bulk HTS Materials	Maley Maley	45.2 199.4	60 485.9	Ph 1: 2/90 Ph 2: 1/92 1/94
HiTc Superconco	Optimizing Performance of HTS Cavities and Targets	Wu Wu	136.6 101.9	125 100	Ph 1: 9/89 Phase 2: 12/91
Ceracon, Inc	Bulk HTS Consolidation	Foltyn	237.5	300	Phase 1: 6/91

Nuclear Metals/ SNL/AT&T	HTS Co- extrusion	Wallace Bingert	239.2 239.2	760.5 285 NM 190 ATT	Ph 1: 8/90- 8/93 Ph. 2: 10/93-10/96
The Boeing Company	Superconducting Electromagnetic Devices	Peterson	240	240	4/97 - 4/98
Power Superconduct- ing Devices, Inc	Development of HTS Fault Current Limiter	Peterson	250	250	7/96-7/98

6b. CRADA Agreements - Completed

Organization	Topic	PI	Funding,\$K DOE	Funding,\$K Partner	Dates
Lockheed Martin	Coil Development	Peterson	330	210	7/93 - 7/96
Plastronic, Inc.	Liquid Cryogen Free HTS Magnet System	Daugherty	100 +33k funds in	67	6/95 - 5/96
The BOC Group, Inc.	Superconducting Coated Materials	Peterson	70	70	2/23/96- 11/22/96
EURUS Technologies, Inc.	Development of HTS Current Leads & Solders	Peterson	80	140	2/6/96- 2/5/97
Eriez Magnetics	HTS Magnetic Separation	Daugherty	70	52	4/2/96- 4/1/97
Lockheed Martin	HTS Current Limiter	Peterson	400	400	11/95-10/97
Lockheed Martin	Bridge-Type Fault Current Limiter	Boenig	700	1400	11/95-9/98
General Atomsics (assumed LM activity)	Bridge-Type Fault Current Limiter	Peterson	Remainder of 700 from above	Remainder of 1400 from above	9/98-5/99, 5/99-11/99
Astronautics Corp. of America	Active HTS Magnetic Refrigerator	Peterson	200	200	4/98-7/00
ABB Power T&D Co., Inc.	HTS Transformer	Maley	95	70	7/99-7/00

6c. Funds In / Funds Out Agreements - Completed

Organization	Topic	PI	Type	Value \$K	Dates
Superconductor Technologies, Inc.	Rutherford Backscattering	Maggiore	Funds In	1.0	5/88 - 5/89
Public Service Co. of New Mexico	HTS Theory	Parkin	Funds In	357.1	6/88 - 6/90

EPRI	Assessments for Utilities	Newkirk	Funds In	99.8	6/88 - 6/89
AMP, Inc.	RF Characterization of TI-Based HTS Films	Wallace	Funds In	102.9	1/89 - 5/89
EPRI	Heat Pipe Switch	Merrigan	Funds In	150	1/89 - 1/90
Univ. Missouri, Rolla	HTSC Fibers	Maestas	Funds Out	111	1/89 - 1/90
Bechtel	SMES Systems/ Hot-to-Cold Transitions	Maestas	Funds Out	10	2/89 - 2/90
Rocketdyne Corp., Rockwell, Intl.	Synthesis of TI HTS	Peterson	Funds Out	95.3	5/89 - 5/90
EPRI	New Families of HTS	Smith	Funds In	120	2/90 - 2/92
Underground Systems	Transmission Systems	Stewart	Funds In	48	5/91 - 5/92
W.J. Schafer Assoc.	SMES Assessment	Peterson	Funds Out	89.9	5/92 - 5/93
Univ. Calif.-San Diego	Hydrocode Models	Peterson	Funds Out	63 57	12/92 -12/93 6/94 - 5/95
Intermagnetics General Corporation	TI-Based HTS Coils	Peterson	Funds Out	400	10/92 - 10/96
MIT	Bitter Magnets	Peterson	Funds In	50	5/93 - 4/96
Midwest Superconductivity, Inc.	IBAD-Coated Flexible Substrates	Peterson	SBI Tech Consulting Agreement	5	3/95 - 3/96
EPRI	Ac Loss Measurements in HTS Cables	Maley	Funds In	150	9/5/95- 9/4/96
EPRI	Thick Films on Flexible Substrates	Wu	Funds In	25 200	7/95-9/95 10/95-10/96
Pirelli Cable & Systems	Ac Losses on HTS Cables	Peterson Willis	Funds In	55 63	11/97 – 6/98 1/99 – 9/99

6d. Other Collaborations - Completed

Organization	Topic	PI	Dates
Tektronix, Inc.	Cryogenic Materials Characterization	J. Smith	11/89-5-94